

https://dspace.org/

Focusing of expansion waves

Whalley, Matthew Sean

2016
http://hdl.handle.net/10539/20626

Downloaded from a DSpace repository. https://dspace.org/

Focusing of Expansion Waves

M. S. Whalley

A dissertation submitted to the Faculty of Engineering and the Built Environment, University of the Witwatersrand, Johannesburg, in fulfilment of the requirements for the degree of Master of Science in Engineering.

Johannesburg, February 2016

Declaration

I declare that this dissertation is my own, unaided work, except where otherwise acknowledged. It is being submitted for the degree of Master of Science in Engineering in the University of the Witwatersrand, Johannesburg. It has not been submitted before for any degree or examination at any other university.

Signed this 14th day of February 2016



M. S. Whalley

Abstract

The flow field which results from an expansion wave entering a cavity, and the focusing effect which occurs was studied using both numerical and experimental methods. Previous research into cavity flows has looked at shock waves entering a cavity as well as shock wave focusing phenomenon; however no previous work on expansion wave cavity flows was found. The type of flow was analysed for different cavity geometries, different expansion wave pressure ratios and different expansion wave widths. The numerical work was done using the commercial CFD codes, Ansys Fluent and STAR CCM+. An inviscid solver was found to be sufficiently accurate to model the flow. The experimental work was performed using a unique shock tube with windows at the diaphragm and in the driver section. A number of sub-studies were done during the development of the shock tube. These included a short study on the use of different materials as a diaphragm in a shock tube in order to get the best possible expansion wave for the experiments. Hundred micron thick aluminium sheets were found to give the best burst as it responded well to scoring and once scored gave a consistent symmetrical burst. Another study was performed into the straightening of an initially curved expansion wave. This was done to try and improve the experimental results as a diaphragm will always have some curvature at burst resulting in an initially curved expansion wave. It was found that by curving the walls of a shock tube the leading edge of an expansion wave could be made to straighten faster, however this introduced additional undesirable two-dimensional waves behind the leading edge of the expansion which resulted in a simple straight walled shock tube being used in the experiments. The numerical and experimental work showed that a focus region forms when an expansion wave enters a cavity, and this region has very low fluid property values, especially temperature and pressure. The basic focus region can be described as a region of flow enclosed by compression or shock waves in which two dimensional expansion waves repeatedly reflect to create very low pressures and temperatures. The effect of an initially curved expansion wave was considered and it was found that the flow is significantly affected by the shape of the expansion. For a plane expansion wave a focus region develops in the driver section of the tube and collapses towards the end of the driver. For a curved expansion wave the focus region develops at the centre of the curvature. The pressure ratio over the expansion wave

was also studied by changing the initial diaphragm pressure ratio in the shock tube. It was found that as the wave strength was increased, the focusing happened later and was stronger until the pressure ratio was sufficiently high for supersonic flow to occur. At this point the focusing changed, most significantly for the cylindrical cavity where the flow pattern seen for subsonic flow disappeared completely, and was replaced by a different focusing pattern. The width and thus the gradient of the expansion wave was also found to be important as once the expansion wave starts to widen, the focusing becomes significantly weaker and may not even be noticeable.

Contents

Declaration **i**

Abstract **ii**

Contents **iv**

List of Figures **viii**

List of Tables **xiv**

1 Introduction **1**

1.1 Background 1

1.2 Motivation 2

2 Literature Survey **3**

2.1 1-Dimensional Gas Dynamics 3

2.1.1 General theory 3

2.1.2 Compression and shock waves 4

2.1.3 Expansion waves 6

2.2 Shock Tube Theory 7

2.2.1 Assumptions . . . 7

2.2.2 Governing equation . . . 7

2.2.3 Shock tube wave diaphragm . . . 8

2.2.4 Solution to the shock tube equation . . . 8

2.3 Previous Research . . . 10

2.3.1 Two-dimensional expansion wave diffraction around a 90^o convex corner - I. Mahomed (2013) . . . 10

2.3.2 Shock wave-induced flow features in concave profiles - D. MacLucas (2012) . . . 12

3 Objectives **14**

4 Apparatus **15**

4.1 Experimental . . . 15

4.1.1 Expansion wave generator . . . 15

4.1.1.1 Description . . . 15

4.1.1.2 Design . . . 16

4.1.1.3 Post Manufacture Development . . . 18

4.1.2 Expansion wave straightening . . . 18

4.1.3 Diaphragm selection . . . 23

4.1.3.1 Plastic . . . 24

4.1.3.2 Aluminium foil . . . 24

4.1.3.3 Brass foil . . . 27

4.1.3.4 Copper foil . . . 27

4.1.3.5 Stainless steel foil . . . 27

4.1.4 Optical system 29
4.1.5 Data capture 30
4.2 Numerical 31

5 Methodology **32**

5.1 Experimental 32
5.1.1 Start of day procedure 32
5.1.2 Diaphragm preparation 32
5.1.3 Diaphragm replacement 33
5.1.4 Test piece positioning and replacement 33
5.1.5 Test procedure 34
5.1.6 End of day procedure 35
5.2 Numerical 35
5.2.1 Geometry 35
5.2.2 Meshing 37
5.2.2.1 Mesh independence 38
5.2.3 Solver set-up 39
5.2.3.1 Solver independence 40

6 Data Processing **41**

6.1 Image processing 41
6.2 Numerical Results Processing Method 43

7 Results and Discussion **46**

7.1 Description of Flow Field 46
7.1.1 Cavity geometry 46
7.2 Curved Diaphragm simulations 64
7.3 Results for Different Diaphragm Pressure Ratios 67
7.4 Results for Different Test-piece Distances from the Diaphragm 76
7.5 Experimental/Numerical Validation 78
7.5.1 Shock-wave formed at exit of shock tube 84
7.5.2 Pressure trace comparisons 87

8 Conclusions **89**

9 Recommendations **90**

A Digital Appendix **92**

B Numerical Simulations **93**

C Experimental Tests **94**

List of Figures

2.1 Propagation of small disturbance waves in 1-D flow [5] 4

2.2 Gas property changes over a shock wave [5] 5

2.3 Flattening of an expansion wave with time 6

2.4 Shock tube wave diagram with pressure and temperature at time t_1 [5] 9

2.5 Shock Mach number against diaphragm pressure 10

2.6 Shock pressure ratio against diaphragm pressure 10

2.7 Expansion pressure ratio against diaphragm pressure 11

2.8 Expansion temperature ratio against diaphragm pressure 11

2.9 Expansion density ratio against diaphragm pressure 12

2.10 Flow velocity and trailing expansion characteristic velocity against diaphragm pressure 12

2.11 Diffraction of an expansion wave around a 90^o convex corner [4] 13

2.12 Shock focusing, [3] 13

4.1 Shock tube 15

4.2 Test piece geometries, converging (left), triangular (middle), cylindrical (right), the actual test pieces are shown below the sketches of the geometry 16

4.3 CAD design of Shock tube 17

4.4 Electrical burst mechanism 18

4.5 Modelling the leading edge of an expansion wave in a straight tube 20

4.6 Comparison with numerical results 21

4.7 Wall geometry for theoretical straight wave 22

4.8 Curved wall numerical results 23

4.9 Plastic diaphragm burst 25

4.10 Plastic diaphragm after test 25

4.11 Aluminuim diaphragms after burst, left: 1 diaphragm used, middle: 2 diaphragms used, right: 3 diaphragms used 26

4.12 Aluminium diaphragm burst 26

4.13 Brass diaphragm after test 27

4.14 Brass diaphragm burst 28

4.15 Copper diaphragm after test 28

4.16 Stainless steel diaphragmafter test 29

4.17 Schlieren setup 29

4.18 Schlieren filters 30

4.19 Comparison of vertical (left) and horizontal (right) filters 30

4.20 Pressure transducer location 31

5.1 Diaphragm template 33

5.2 Examples of geometry for numerical simulations, Cylindrical test piece with plane diaphragm (top), Triangular test piece with curved diaphragm (bottom). 36

5.3 Annotated geometry for numerical simulations 36

5.4 Geometry with added outside region 37

5.5 2mm base mesh for numerical simulations 38

5.6 Zoomed in view of interface for 1mm base mesh 38

5.7 Summary of mesh independence results: 2mm mesh no automatic refinement (top), 0.5mm mesh no automatic refinement (middle), 0.5mm mesh automatic mesh refinement (bottom) 39

5.8 Comparison of Fluent (left) and STAR CCM+ (right) results showing solver independence 40

6.1 Base experimental image 41

6.2 Image with 'blank' image subtracted from it 42

6.3 Final processed image 42

6.4 Example of contours of Density (top), Pressure (second), Temperature (third) and the locations for pressure and temperature data (bottom) 43

6.5 Example of numerical shadowgraph (top), schlieren, horizontal gradients (middle), schlieren, vertical gradients (bottom) 44

6.6 Example of 3 dimensional surface plot 45

6.7 Top view of surface plot 45

7.1 Time series for no test piece, P41 = 7, Contours of density 47

7.2 Time series for cylindrical test piece, P41 = 7, Contours of density 49

7.3 Movement of a plane expansion wave into a cylindrical cavity, Contours of Temperature 50

7.4 Movement of compression waves into cylindrical cavity, Contours of Temperature 51

7.5 Time series for triangular test piece, P41 = 7, Contours of density 52

7.6 Detailed focusing phenomena for triangular test piece, Contours of Temperature 54

7.7 Time series for Converging test piece, P41 = 7, Contours of density 55

7.8 Detailed focusing phenomena for converging test piece, Contours of Temperature 56

7.9 Time series for Parabolic test piece AD 0.5, P41 = 7, Contours of density . . 57

7.10 Detailed focusing phenomena for Parabolic test piece AD = 0.5, Contours of Temperature 58

7.11 Time series for Parabolic test piece AD 1, P41 = 7, Contours of density . . . 59

7.12 Detailed focusing phenomena for Parabolic test piece AD = 1, early, Contours of Temperature 60

7.13 Detailed focusing phenomena for Parabolic test piece AD = 1, late, Contours of Temperature 61

7.14 Minimum pressure and temperature for different geometries 61

7.15 Wave position along centre line vs time plots for different geometries, coloured by temperature 62

7.16 Contour plot with temperature along symmetry line for cylindrical test piece and diaphragm pressure ratio of 7 63

7.17 Time series for cylindrical test piece with an initially curved diaphragm, P41 = 5, Contours of density 65

7.18 Time series for triangular test piece with an initially curved diaphragm, P41 = 7, Contours of density 66

7.19 Wave position along centre line vs time plots for different geometries with an initially curved diaphragm, coloured by temperature 67

7.20 Comparison of flow for different diaphragm pressure ratios below 10 (arrow indicates when lowest flow values occur, Contours of temperature, 0.000042s between frames 68

7.21 Plot of minimum temperature and pressure with diaphragm pressure, P41 ¡10, Cylindrical test piece 69

7.22 Comparison of flow for different diaphragm pressure ratios above 10, Contours of temperature, early flow features 70

7.23 Comparison of flow for different diaphragm pressure ratios above 10, Contours of temperature, late flow features 71

7.24 Plot of minimum temperature and pressure with diaphragm pressure, P41 ¿ 10, Cylindrical test piece 72

7.25 Comparison of flow for different diaphragm pressure ratios, triangular test piece, Contours of density, time between images = 0.000056s 73

7.26 Plot of minimum temperature and pressure with diaphragm pressure for triangular test piece 74

7.27 Comparison of flow for different diaphragm pressure ratios, converging test piece, contours of density, time between images = 0.000056s 75

7.28 Plot of minimum temperature and pressure with diaphragm pressure for converging test piece 76

7.29 Time series for cylindrical test piece placed 60mm from the diaphragm, P41 = 7, Contours of temperature 77

7.30 Time series for cylindrical test piece placed 500mm from the diaphragm, P41 = 7, Contours of temperature 77

7.31 Wave position along centre line vs time plots for cylindrical test piece at different distances from the diaphragm, coloured by temperature 78

7.32 Time series of experimental images for the cylindrical test piece and an initial diaphragm pressure ratio of 3. From top left to bottom right. 0.00002s between images first image is approximately 0.00024s after diaphragm burst 79

7.33 Flow features seen in experimental images and numerical contour plots for cylindrical test piece, P41 = 3 80

7.34 Time series of experimental images for the triangular test piece and an initial diaphragm pressure ratio of 3. From top left to bottom right. 0.00002s between images 81

7.35 Flow features seen in experimental images and numerical contour plots for triangular test piece, P41 = 3 82

7.36 Time series of experimental images for the converging test piece and an initial diaphragm pressure ratio of 3. From top left to bottom right. 0.00002s between images 83

7.37 Flow features seen in experimental images for the converging test piece 84

7.38 Shock wave at late time step in experimental results, left aluminium, middle brass, right plastic. First frame approximately 0.00565s, 0.0059s and 0.00595s after diaphragm burst respectively 85

7.39 Numerical result showing formation of reflected shock at tube exit 86

7.40 Pressure trace for numerical tests for the cylindrical test piece 87

7.41 Pressure trace for numerical tests for the triangular test piece 87

7.42 Pressure trace for numerical tests for the converging test piece 88

7.43 Comparison of pressure traces from the experimental tests for the cylindrical test piece 88

List of Tables

4.1 Piston vs Shock tube 17

4.2 Shock tube specifications 17

4.3 Optics specifications 29

4.4 Data capture equipment used 31

4.5 Computer specifications 31

5.1 Geometries for numerical simulations 37

5.2 Solver settings 40

B.1 All numerical simulations run 93

1 Introduction

1.1 Background

In fluid dynamics, information is passed through the fluid by pressure waves. These waves either cause the pressure of the fluid to increase (compression waves), or to decrease (expansion waves). The majority of research to date has focused on compression waves and more specifically shock waves, which occur when the pressure gradient of the compression wave becomes infinite. Expansion waves are as common as compressions as generally if the pressure of one area is increasing, due to a compression wave, the pressure in a different region needs to decrease, requiring an expansion wave. An example of this is the opening/failure of a pressure vessel which initially contains a fluid at a higher pressure than its surroundings. When the vessel is opened the higher pressure fluid will move out of the vessel and cause the fluid it is moving into to increase in pressure (compression). However, the fluid within the vessel will decrease in pressure as the fluid moves out of it (expansion).

Now imagine a plane expansion wave travelling through a fluid. This wave will cause the fluid to decrease in pressure and as a result, cause the fluid to flow in the direction opposite to the direction the wave is moving. If this wave was to hit a plane wall, the pressure at the wall would decrease further than the rest of the fluid due to continuity. The fluid which was in the region has been accelerated away from the wall and there is no additional fluid available to flow into the region. This results in a "reflected" expansion wave which moves away from the wall, causing an additional decrease in pressure in the fluid, which also causes the fluid to be accelerated back towards the wall. Thus continuity is conserved. If the wall was not plane, a cavity flow would result. Cavity flows for shock waves have been investigated and have been found to produce interesting flow features. Expansion cavity flows have not been researched and thus this is the type of flow which this research will investigate.

A common tool for investigating fluid flow phenomena, usually shock wave phenomena, is the shock tube. This is essentially a pressure vessel which is designed to fail in a desired and predictable manner. This is done through separating a high pressure region from a

low pressure region through means of a diaphragm made from material that is significantly weaker than the tube. This set up results in expansion waves in the high pressure region and compression/shock waves in the low pressure region after diaphragm burst. The fact that expansion waves are set up in a predictable manner by a shock tube makes it fitting tool for this research.

1.2 Motivation

Previous research on wave focusing has concentrated on shock wave cavity flows. Expansion wave cavity flows have not been investigated and are thus are the focus of this research. This type of flow is likely to occur when a pressure or vacuum vessel fails. An understanding of the flow could help in producing safer designs of such vessels. This also has application in the medical field as the flow is also expected to create a region of very low temperature and pressure (in contrast to shock wave focusing where a region of high pressure and temperature is formed).

2 Literature Survey

2.1 1-Dimensional Gas Dynamics

2.1.1 General theory

One dimensional flow consists of the behaviour of a fluid which can only move along one axis, such as an idealised duct flow. In compressible flow the fluid density can change, decreasing in the case of an expansion and increasing in the case of compression. In compressible flow information is passed through the fluid by waves. For example, if there was to be a small disturbance in a region of one-dimensional flow, this information will be passed into the fluid at sound speed, causing the fluid to adjust it's properties based on the nature of the disturbance. The changes in the fluid properties can be calculated using the basic principles of one-dimensional flow. These are derived from the conservation of mass, Equation 2.1, conservation of momentum, Equation 2.2, and the equation of state. For the purposes of this research the following simplifying assumptions can be made about the fluid. The fluid is an ideal gas, thus the ideal gas equation, Equation 2.3, can be used as the equation of state, and the flow is essentially isentropic, except where a shock is formed.[4]

$$A\frac{\delta\rho}{\delta t} + \frac{\delta}{\delta t}(\rho u A) = 0 \tag{2.1}$$

$$A\frac{\delta u}{\delta t} + u\frac{\delta u}{\delta x} = -\frac{1}{\rho}\frac{\delta p}{\delta x} \tag{2.2}$$

$$p = R\rho T \tag{2.3}$$

These equations can be used to determine the fluid properties within the flow field. The speed of sound in the fluid is also required and can be found according to Equation 2.4. Both

R and γ can be assumed to be constant if a single fluid is being considered. The speed of sound in the fluid is thus dependent only on temperature.

$$a^2 = \gamma RT \tag{2.4}$$

As the wave is travelling at sound speed relative to the fluid the absolute velocity of the wave will be the velocity of the fluid plus the local sound speed, as given in Equation 2.5. For a compression wave, the wave travels in the same direction as the fluid and for an expansion wave in the opposite direction.

$$U = u \pm a \tag{2.5}$$

Once the wave velocity is known a diagram can be constructed to describe the flow, an example of which is given in Figure 2.1 which shows the propagation of waves due to a small disturbance. Equation 2.1, Equation 2.2 and Equation 2.3 can then be used along with the initial or boundary conditions to determine the fluid properties throughout the flow region.

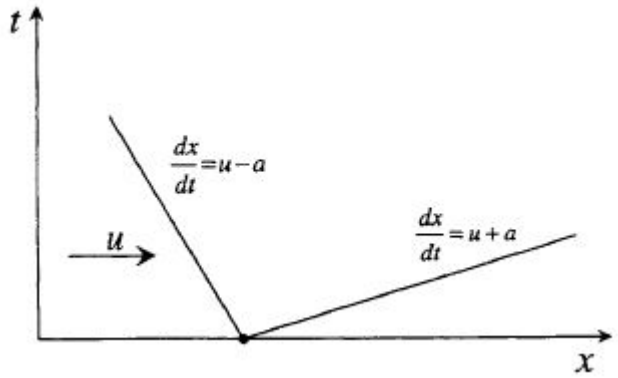


Figure 2.1: Propagation of small disturbance waves in 1-D flow [5]

2.1.2 Compression and shock waves

Compression waves cause a fluid to increase in pressure and move in the same direction as the wave. The result of this is that the leading edge of the wave travels at a lower velocity than the trailing edge of the wave, thus the gradient of the wave tends to increase. The trailing edge of the wave will catch the leading edge after a certain distance. At this point the gradient becomes infinite and the compression wave becomes a shock wave. The changes in fluid properties across a shock are shown in Figure 2.2. This image is for a moving fluid going through a stationary shock wave. The flow velocity is decreased (changing the

reference frame to a shock wave travelling through a stationary fluid, this corresponds to the fluid being accelerated in the same direction as the shock wave is travelling). All the other fluid properties are increased through the shock wave, e.g. the pressure behind the shock wave is higher than the fluid pressure before it. There is an increase in entropy associated with a fluid passing through a shock wave. The process is not reversible.

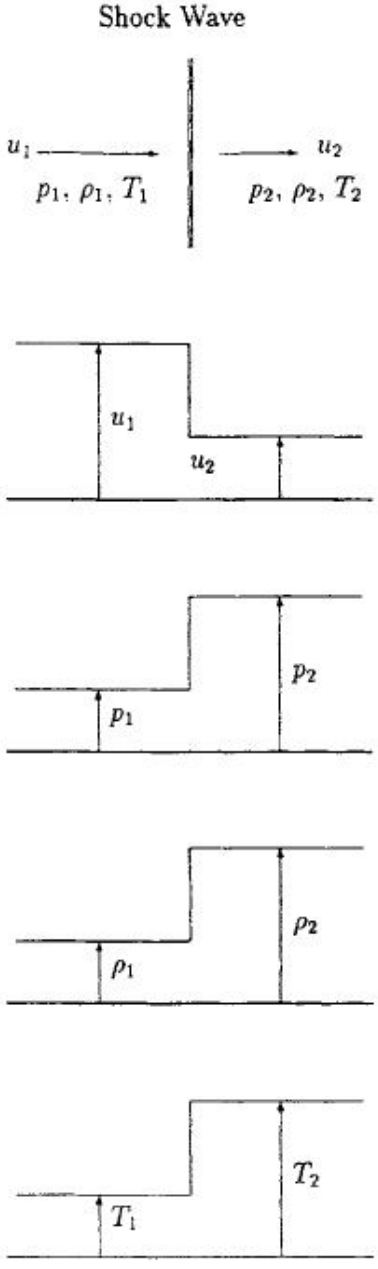


Figure 2.2: Gas property changes over a shock wave [5]

2.1.3 Expansion waves

Expansion waves cause a fluid to decrease in pressure and move in the opposite direction to the wave. This means that the leading edge of the expansion moves at a higher velocity than the trailing edge, as a result, unlike compression waves, expansion waves tend to flatten out and their gradients become weaker over time, shown in Figure 2.3.

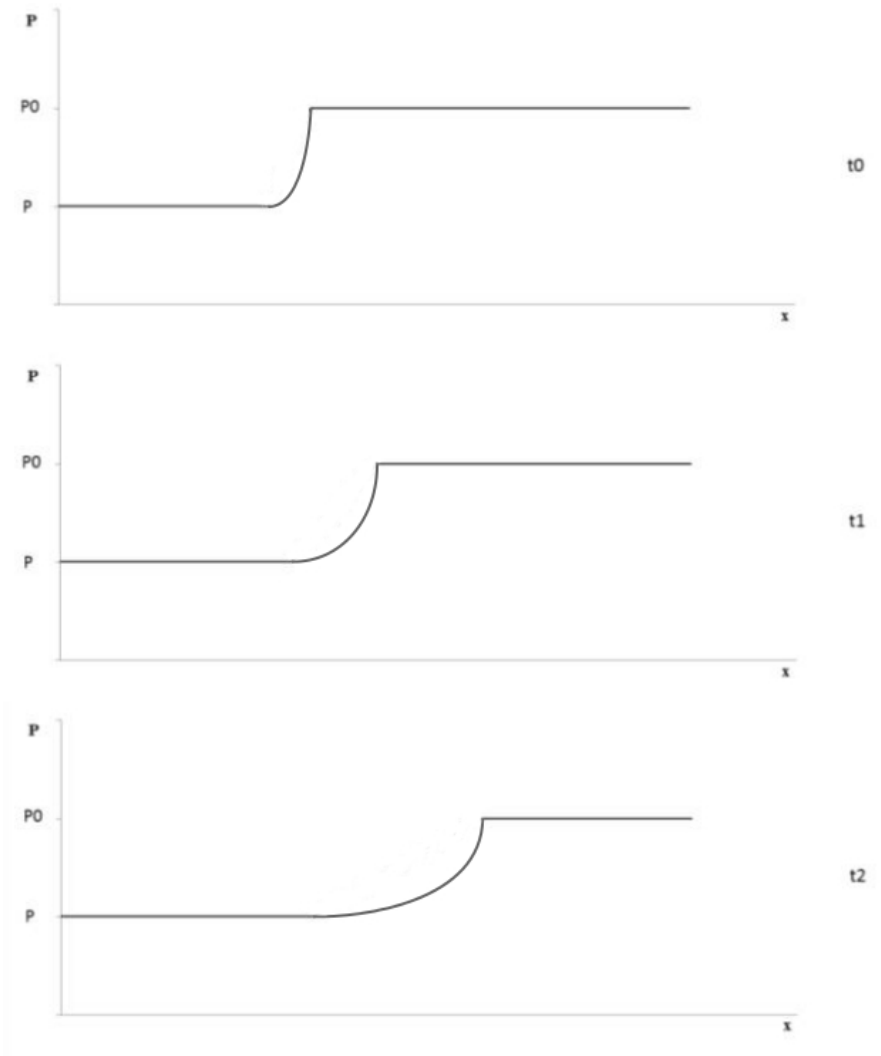


Figure 2.3: Flattening of an expansion wave with time

This phenomenon results in expansion waves generally having weaker gradients than compressions, making them more difficult to visualise using optical techniques. The flow through an expansion wave is isentropic. The changes in fluid properties through an expansion wave are opposite to a compression wave. That is, the fluid is accelerated in the opposite direction to the movement of the expansion wave and the fluid properties decrease. [2]

2.2 Shock Tube Theory

A shock tube is a device used to study short duration flows. In its simplest form it consists of a straight tube of constant cross-sectional area separated by a diaphragm into two sections of different pressure. When the diaphragm is rapidly removed a shock wave moves into the low pressure section and an expansion wave moves into the high pressure section. A contact surface lies between the shock wave and the expansion wave and moves at the fluid velocity. The fluid pressure and velocity is constant over the contact surface but temperature and density changes. The flow within a shock tube can be analysed using gas dynamics theory.

The basic flow field after diaphragm removal can be broken up into four regions. The first region is ahead of the shock wave in the low pressure section and the fluid properties are the initial properties of the low pressure region of the tube before diaphragm removal. The second region lies between the shock wave and the contact surface. This region will have a higher pressure, density, temperature and velocity than region 1 as the fluid has had a shock wave pass through it. The third region lies between the contact surface and the expansion wave, it has the same pressure and velocity as region 2, however it will be at a lower temperature. The fourth region lies ahead of the expansion wave in the high pressure section and the fluid properties are the same as initial fluid properties of the high pressure section.

2.2.1 Assumptions

When analysing the flow in a shock tube the following assumptions are made about the flow. The flow is assumed to be one-dimensional, with the walls of the tube being straight and the cross-section of the tube constant. This assumption holds for a basic shock tube, but is not the case once test pieces are placed into the tube. It does allow the initial conditions before the wave hits the test piece to be determined. The fluid is assumed to be inviscid, which is generally valid as the viscous effects are small. However, in real flows, near the walls where the boundary layer is present this assumption becomes invalid. [7] [2] [5]

2.2.2 Governing equation

Equation 2.6 is the governing equation for a shock tube, the subscripts denote the region to which the property belongs. The derivation of the equation can be found in many gas dynamics text books such as [7] or [1]. It relates the shock strength to the initial pressure differential over the diaphragm. This is an implicit equation and must be solved numerically. The strength of the expansion wave can also be calculated once the shock strength is known.

This equation assumes that the same gas is used in the two chambers and that γ is constant throughout the fluid. [2]

$$\frac{a_1}{a_4}\frac{\left(1-\frac{\gamma-1}{\gamma+1}\right)\left(\frac{P_2}{P_1}-1\right)}{\sqrt{\left(1+\frac{\gamma-1}{\gamma+1}\right)\left(\frac{P_2}{P_1}+\frac{\gamma-1}{\gamma+1}\right)}} = \frac{2}{\gamma-1}\left\{1-\left(\frac{P_1}{P_4}\frac{P_2}{P_1}\right)^{\frac{\gamma-1}{2\gamma}}\right\} \tag{2.6}$$

2.2.3 Shock tube wave diaphragm

Figure 2.4 gives the wave diagram for a simple shock tube. This diagram shows the 1-dimensional movement of the waves in a shock tube with time. The four flow regions can be seen and the two plots under the wave diagram help to show how the fluid properties vary through the different regions. The shock wave is given by a single line, as it represents a discontinuous change in fluid properties at a specific point, as explained in subsection 2.1.2. The expansion wave is represented by a diverging fan of lines as the expansion tends to flatten out as explained in subsection 2.1.3. Regions 3 and 4 are of the most interest for this research. [5]

2.2.4 Solution to the shock tube equation

Solving the shock tube equation allows the shock Mach number to be determined for a known initial pressure ratio over the diaphragm. This is plotted in Figure 2.5. The figure shows that the relationship between the diaphragm pressure and shock Mach number is logarithmic in nature. Thus for shock Mach numbers above 1.5 the diaphragm pressure required becomes very large. Once the shock Mach number is known, the fluid properties in the different regions for the one-dimensional case, can be calculated. [7]

If the shock Mach number is known, the pressure ratio over the shock wave can be determined. This is plotted in Figure 2.6. The pressure downstream of the expansion wave, P3 is equal to the pressure upstream of the shock wave, P2. The pressure ratio over the shock wave can thus be used to determine the pressure ratio over the expansion wave. The pressure ratio over the expansion wave for different initial diaphragm pressure ratios is given in Figure 2.7.

Figure 2.8 and Figure 2.9 give the relationship between diaphragm pressure ratio and the expansion wave temperature and density ratio respectively. The trend is the same as for pressure.

As expansion waves accelerate the flow in the opposite direction to which they travel and the velocity of a wave characteristic is given by Equation 2.5, the trailing characteristic will

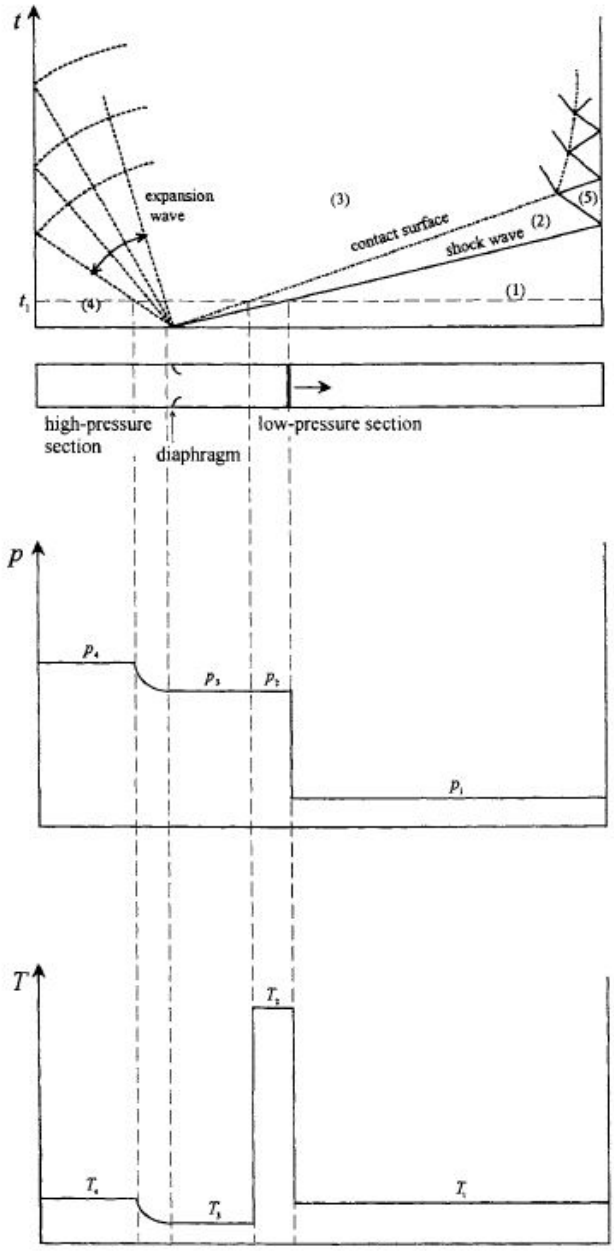


Figure 2.4: Shock tube wave diagram with pressure and temperature at time t_1 [5]

travel in the opposite direction to the leading characteristic of the expansion wave once the flow velocity in which the trailing characteristic is travelling becomes supersonic. Figure 2.10 plots the flow velocity in region 3 as well as the sound speed in region three. The dashed line shows the velocity of the trailing edge of the expansion. A negative velocity indicates that the characteristic is travelling upstream, i.e. in the same direction as the leading characteristic, while a positive velocity means it is travelling downstream. From this graph it can be seen that for an initial diaphragm pressure ratio above 10 the flow will become supersonic and thus the trailing characteristic will travel downstream rather than into the driver section.

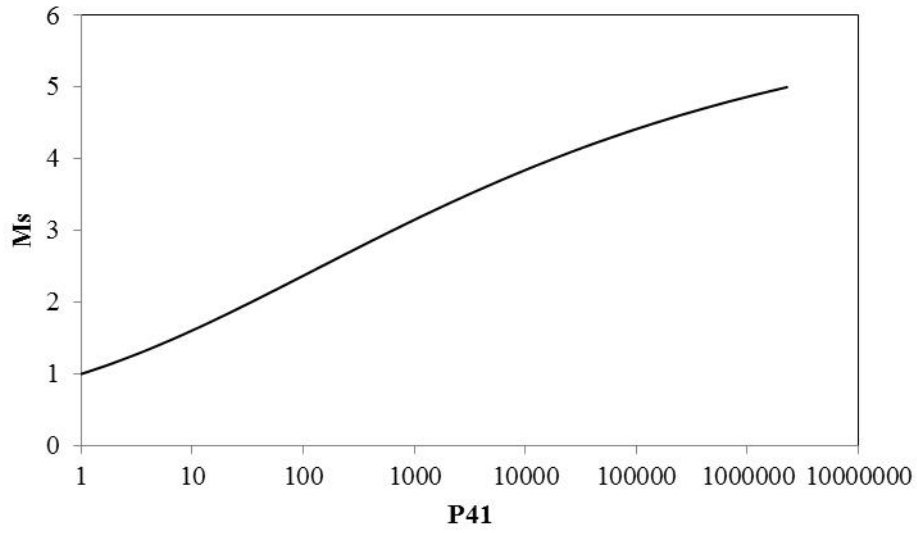


Figure 2.5: Shock Mach number against diaphragm pressure

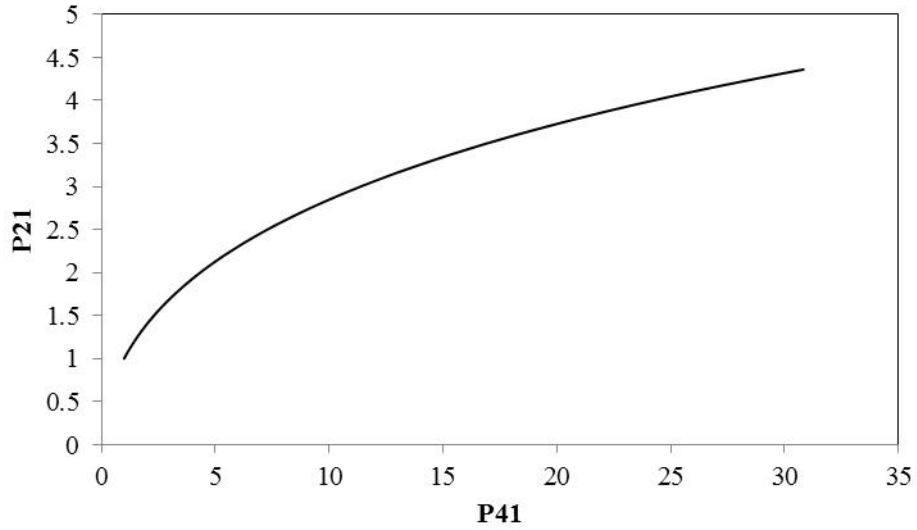


Figure 2.6: Shock pressure ratio against diaphragm pressure

2.3 Previous Research

2.3.1 Two-dimensional expansion wave diffraction around a 90^o convex corner - I. Mahomed (2013)

The flow resulting from an expansion wave diffracting around a 90^o corner in a shock tube was studied both numerically and experimentally. The effect of initial pressure ratio and distance between the diaphragm and the corner were both investigated. Several major flow features were identified, namely a shear layer near the corner apex, a separation bubble attached to

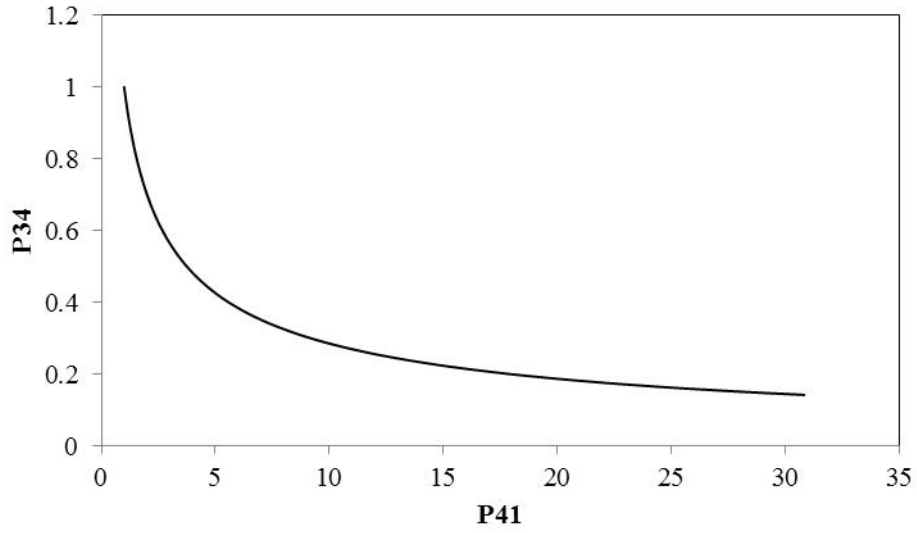


Figure 2.7: Expansion pressure ratio against diaphragm pressure

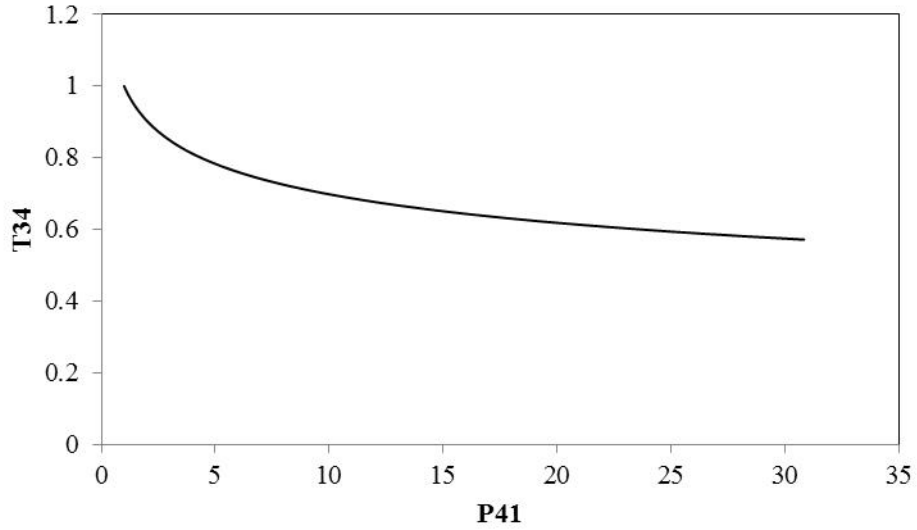


Figure 2.8: Expansion temperature ratio against diaphragm pressure

the wall and a reflected compression wave due to the diffraction of the expansion wave. If the expansion was sufficiently steep (the diaphragm being close to the corner), the reflected compression could steepen to become a weak shock wave. These flow features are hi-lighted in Figure 2.11.

This research found that it was very difficult to visualise the expansion wave due to the weak gradients, however the other features could be identified and used to validate the numerical work. [4]

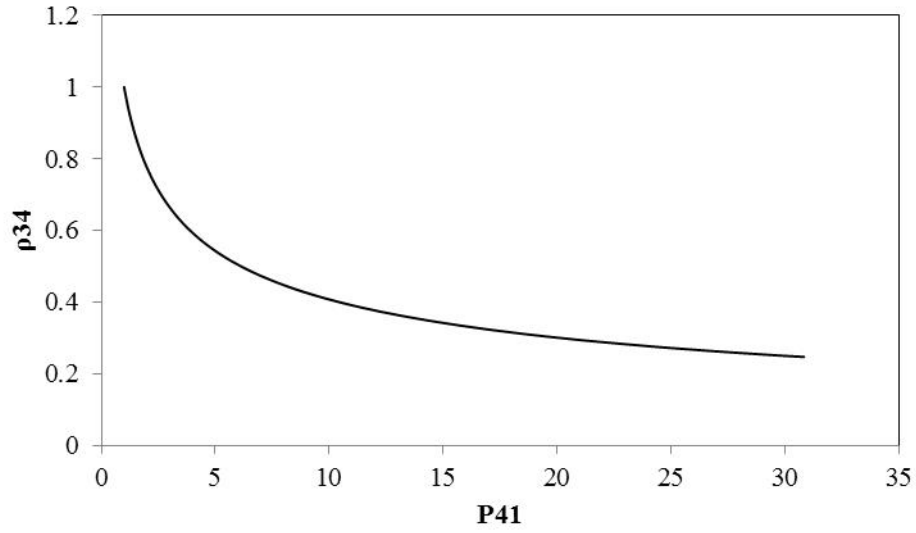


Figure 2.9: Expansion density ratio against diaphragm pressure

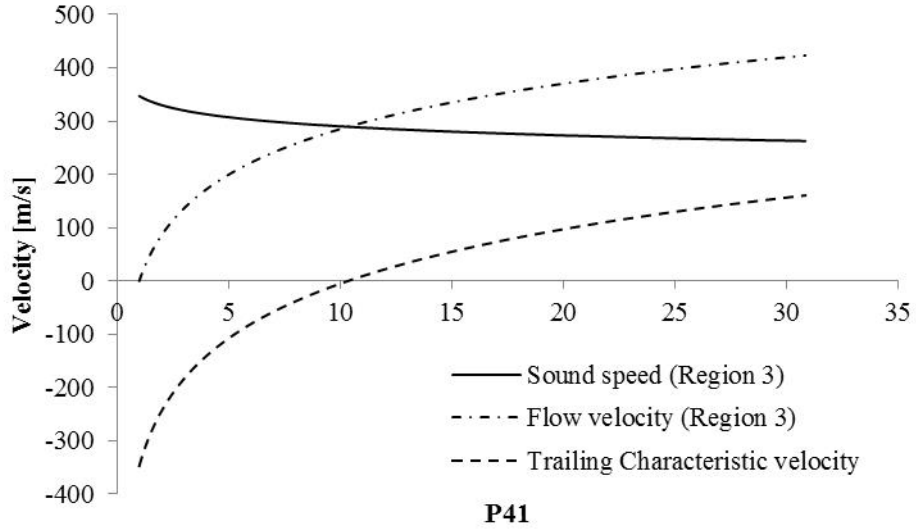


Figure 2.10: Flow velocity and trailing expansion characteristic velocity against diaphragm pressure

For the current study the experimental work done by I. Mahomed (2013) is an important base from which the experiments can be designed.

2.3.2 Shock wave-induced flow features in concave profiles - D. MacLucas (2012)

This work looks at the flow field which results from a plane shock wave entering a concave profile. It contains both experimental and numerical studies. Both the depth to aperture of

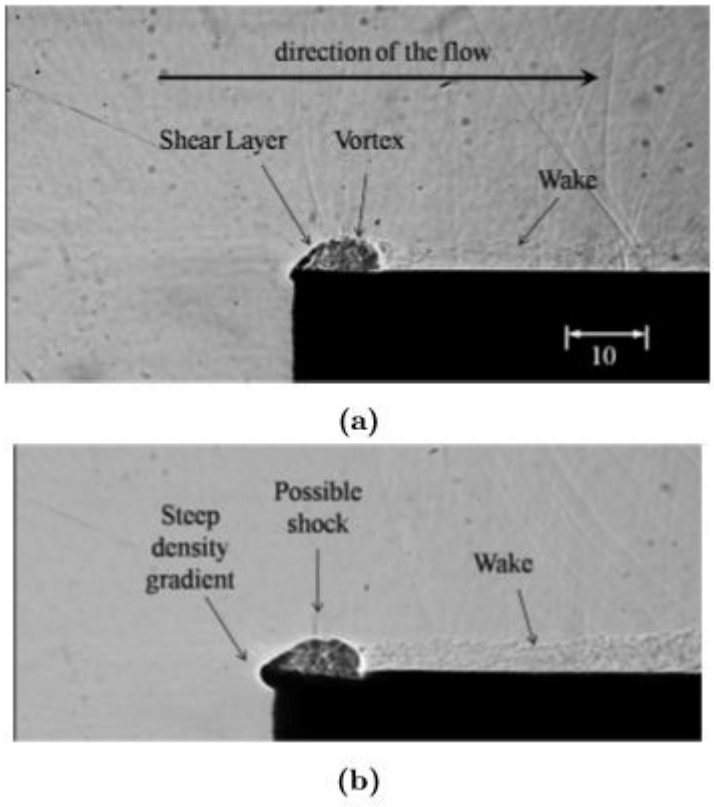


Figure 2.11: Diffraction of an expansion wave around a 90^o convex corner [4]

the cavity as well as the shock Mach number were varied. For the purposes of the current study the research of interest is the focusing flow pattern (illustrated in Figure 2.12). The main feature is the focus region, which contains fluid at high pressure and temperature. A focused expansion wave may be expected to create a similar region but with low pressure and temperature.

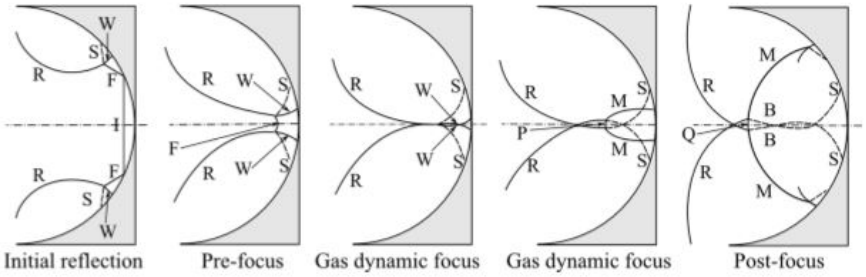


Figure 2.12: Shock focusing, [3]

In Figure 2.12, I is the incident shock wave (It has formed a TRR reflection pattern at the wall) and F and R are reflected shock waves. W is the wall shock and S is a shear layer. During the focusing the Mach stems P and Q form, as well as the additional shocks M and shear layers B. [3] [6]

3 Objectives

1. Determine the flow pattern when an expansion wave is focused for the planar case.
   (a) Determine the effects of expansion wave pressure ratio and wave width.
   (b) Determine the flow patterns for both shallow and deep cavities
2. Study the effect of diaphragm curvature on the focusing phenomenon.
3. Confirm computational results with experimental tests.

4 Apparatus

4.1 Experimental

4.1.1 Expansion wave generator

4.1.1.1 Description

The experimental apparatus used was a unique shock tube. The shock tube shown in Figure 4.1 has split windows which are used to clamp the diaphragm. (This allows the flow immediately around the diaphragm to be visualised.) The test piece is positioned within the high pressure section of the tube and its distance from the diaphragm can be adjusted using a threaded tube. A pressure transducer is located at the centre of the test piece mount and this is used as the trigger for the optics and other data capture equipment. The low pressure section can slide away to allow the diaphragm to be replaced. The low pressure section can have up to 3 pressure transducers fitted to it.

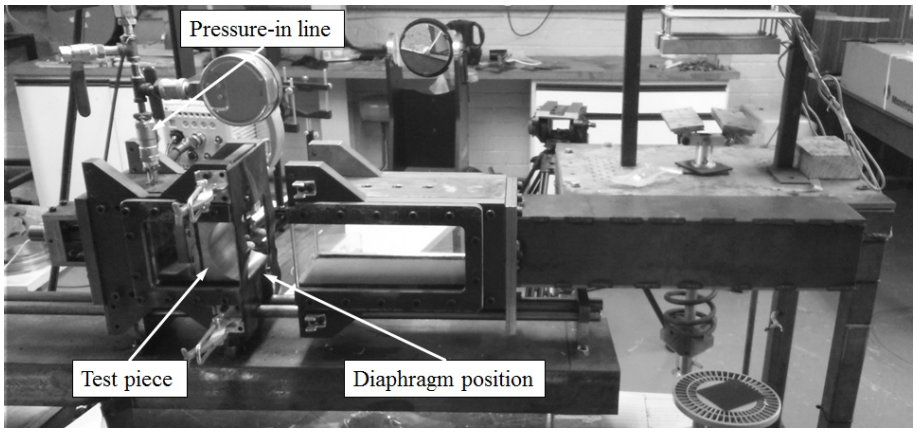


Figure 4.1: Shock tube

The different test piece geometries are shown in Figure 4.2. The pieces are mounted in the tube to form a cylindrical, triangular or converging cavity. The test pieces are made from aluminium.



Figure 4.2: Test piece geometries, converging (left), triangular (middle), cylindrical (right), the actual test pieces are shown below the sketches of the geometry

4.1.1.2 Design

Initially two methods of generating expansion waves were considered. A piston type tube and a shock tube. A piston would allow the shape of the initial expansion to be easily controlled. However it requires a piston to be accelerated at a high rate to generate sufficiently strong waves. The shock tube has the drawback that the shape of the initial expansion wave is not predictable, however it is significantly easier to get waves of sufficient strength. Table 4.1 shows the required pressure ratio in a shock tube versus the piston velocity needed to generate waves of different strengths. A $\frac{P_3}{P_4}$ of around 0.5 was desired. A shock tube design was chosen because the speed that the piston would have to achieve was considered too high for the scale at which the experiments needed to be done.

The major problem with using a shock tube is the diaphragm. As the diaphragm separates two regions of different pressures, it will tend to bend before failure, resulting in a curved wave being formed. This was known at the start of the design process. Once it was decided

Table 4.1: Piston vs Shock tube

M	$\frac{P_3}{P_4}$	$\frac{P_4}{P_1}$	**u [m/s]**
1.1	0.8	1.56	55.2
1.2	0.64	2.353	105.8
1.3	0.52	3.45	152.8
1.4	0.43	4.96	196.8
1.5	0.35	7	238.1

that a shock tube type device would be used, a brief study was done in order to determine if changing the wall geometry around the diaphragm would cause the expansion wave to flatten out faster than if it were a simple straight tube. This study is covered in subsection 4.1.2.

The tube was designed to fall into the sound engineering practice section of pressure vessel regulation. Clamps were chosen to close the tube as they would allow diaphragms to be changed faster than a bolted seal. The design calculations for the sizing of the thickness of the steel and perspex used for the tube can be found in Appendix A. The tube specifications are given in Table 4.2. The shock tube was manufactured from mild steel, and contained perspex windows.

Table 4.2: Shock tube specifications

Component	**Dimension**
Driver Length [mm]	150
Driven Length [mm]	800
Perspex Thickness [mm]	25
Steel Thickness [mm]	25
Cross-section [mm]	100 x 100

A CAD rendering of the shock tube before modifications is given in Figure 4.3.

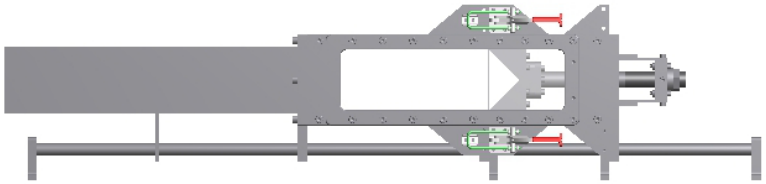


Figure 4.3: CAD design of Shock tube

4.1.1.3 Post Manufacture Development

After manufacture, small adjustments were made to the tube to improve its performance. An additional plate was added at the diaphragm position to assist in diaphragm clamping and the possibility of adding a burst mechanism was explored. As the flow being examined is adjacent to the diaphragm, any burst mechanism used had to have as little effect on the flow as possible. An electrical burst mechanism was chosen as nothing would extend into the test section. The burst mechanism consisted of a power supply, a switch, and a resistive wire which heated rapidly when current was put through it. A diagram of the burst mechanism is given in Figure 4.4. The mechanism was placed in the tube downstream of the diaphragm. The bursts obtained using this mechanism were not as consistent as expected and did not work with metal diaphragms. The decision to use metal diaphragms, discussed in subsection 4.1.3, made the burst mechanism obsolete and it was removed from the shock tube.

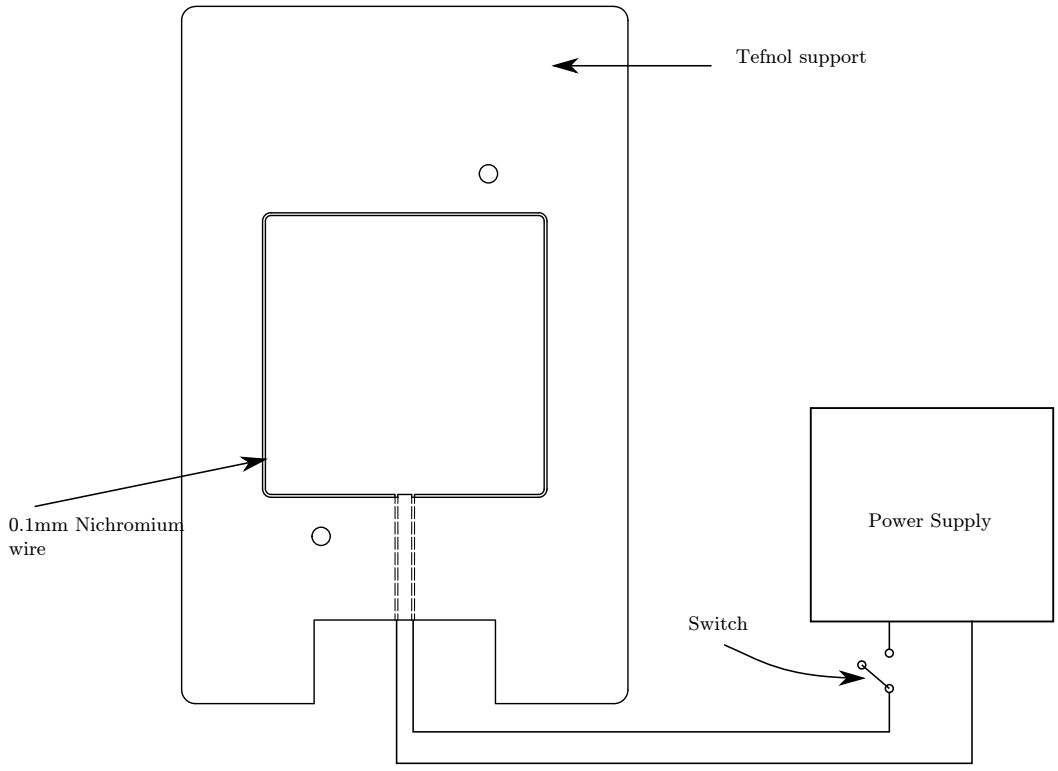


Figure 4.4: Electrical burst mechanism

4.1.2 Expansion wave straightening

The shape of an initially curved expansion wave in an internal flow was examined briefly, with the intention of trying to make it become plane as quickly as possible. It was assumed

that the leading edge of the expansion moves into a stationary fluid. The leading edge of the expansion moves into the fluid at the sound speed of the fluid it moves into. As the expansion causes a decrease in temperature and accelerates the fluid in the opposite direction to the one it travels in, the leading edge would not be affected by waves behind it as they will travel slower than the leading edge. Using this the movement of the expansion wave leading edge can be modelled. Figure 4.5 shows the method by which this was done. The top image shows the starting expansion wave of an arbitrary curvature. By constructing lines of equal length perpendicular to the initial wave, in the direction the wave would travel, an approximate shape of the wave as it moves can be constructed (shown in the second image). Additional perpendicular lines can be added at the midpoint of the new lines, between the wall and the initial wave shape, in order to improve the accuracy of the shape and the process repeated, resulting in the third image. This can then be repeated again and thus the shape of the wave at any distance from the start can be approximated. By decreasing the length of the perpendicular lines a more accurate shape can be created.

This method has a major limitation as it can only be used for wall geometries where the initial expansion doesn't hit the wall. This results in a reflected expansion and the physics at this point needs to be considered in more detail. For applicable wall geometries the predicted shape of the expansion matches closely with CFD data, as shown in Figure 4.6, (the prediction in black is overlaid on density contours) up until the initial expansion wave becomes singular at the symmetry plane of the tube. This also results in reflected waves being formed. This limited period was sufficient for the purposes of this study. However this should be expanded on in future studies to allow the shape to be modelled beyond these limiting cases.

This principle indicates that an expansion will not flatten out along a straight tube as the wave moves straight down the tube both at the walls and at the centre, thus these two points remain at the same position relative to each other. However using the idea that the wave travels at a constant velocity perpendicular to its current shape, possible wall geometries which would cause the wave to become plane can quickly be created. The theory is that by curving the wall and thus changing the direction the wave moves at the wall, the wave could be made to have the same horizontal position at the wall and at the centre after a short distance, this is shown in Figure 4.7. In the figure the double lines represent the curved part of the the wall, which has the same length as the arrow, representing the movement of the centre of the wave straight down the tube. The distance travelled by the the wave along the wall is equal to the distance travelled by the centre of the wave at the end of the curved section. This should result in a plane wave.

The required curve can be calculated using Equation 4.1 which simply sets the arc length of the the wall (d_w) equal to the horizontal distance of the wall (x_w) and the deflection of the

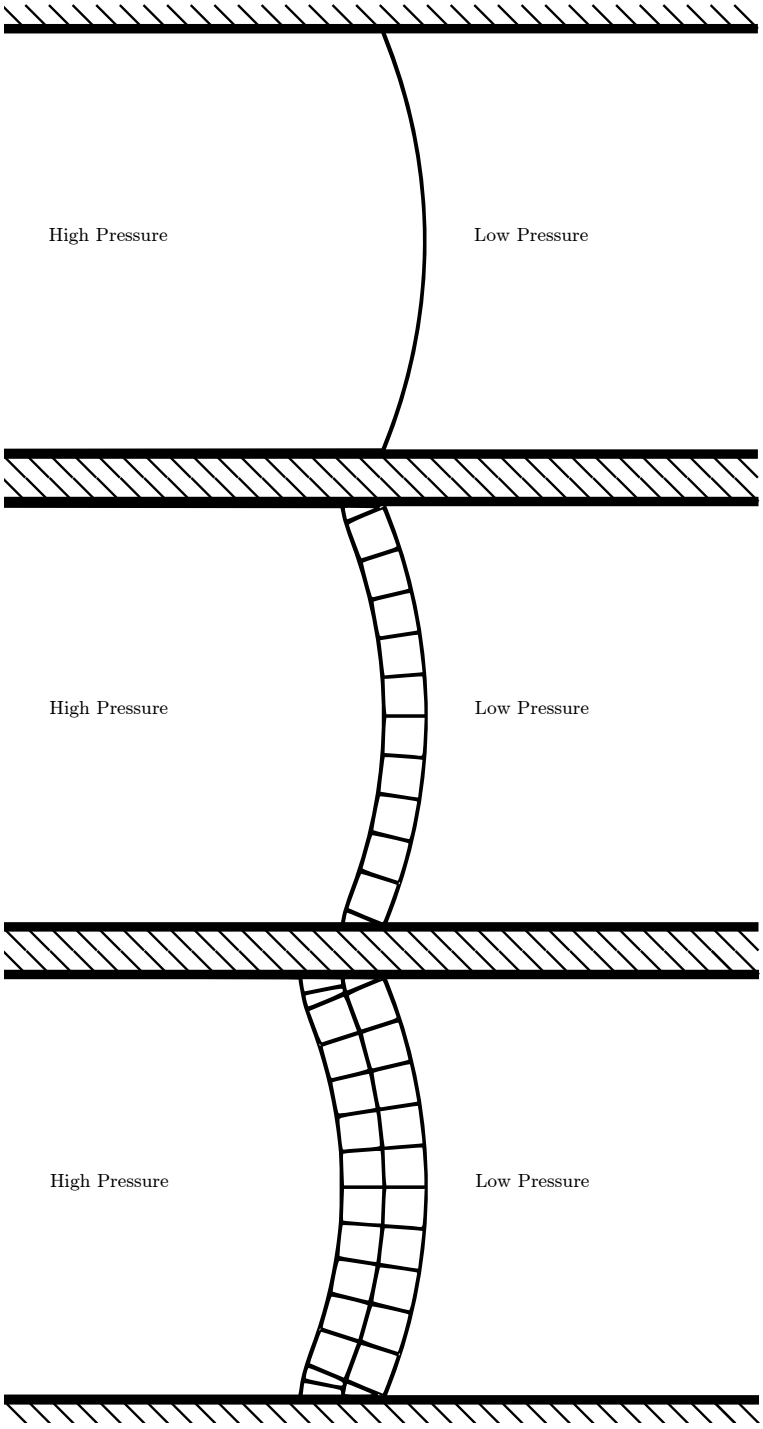


Figure 4.5: Modelling the leading edge of an expansion wave in a straight tube

initial wave (δ). This can be manipulated to give a radius and an angle of an arc centred above the end of the curve as shown in Figure 4.7.

$$d_w = x_w + \delta \tag{4.1}$$

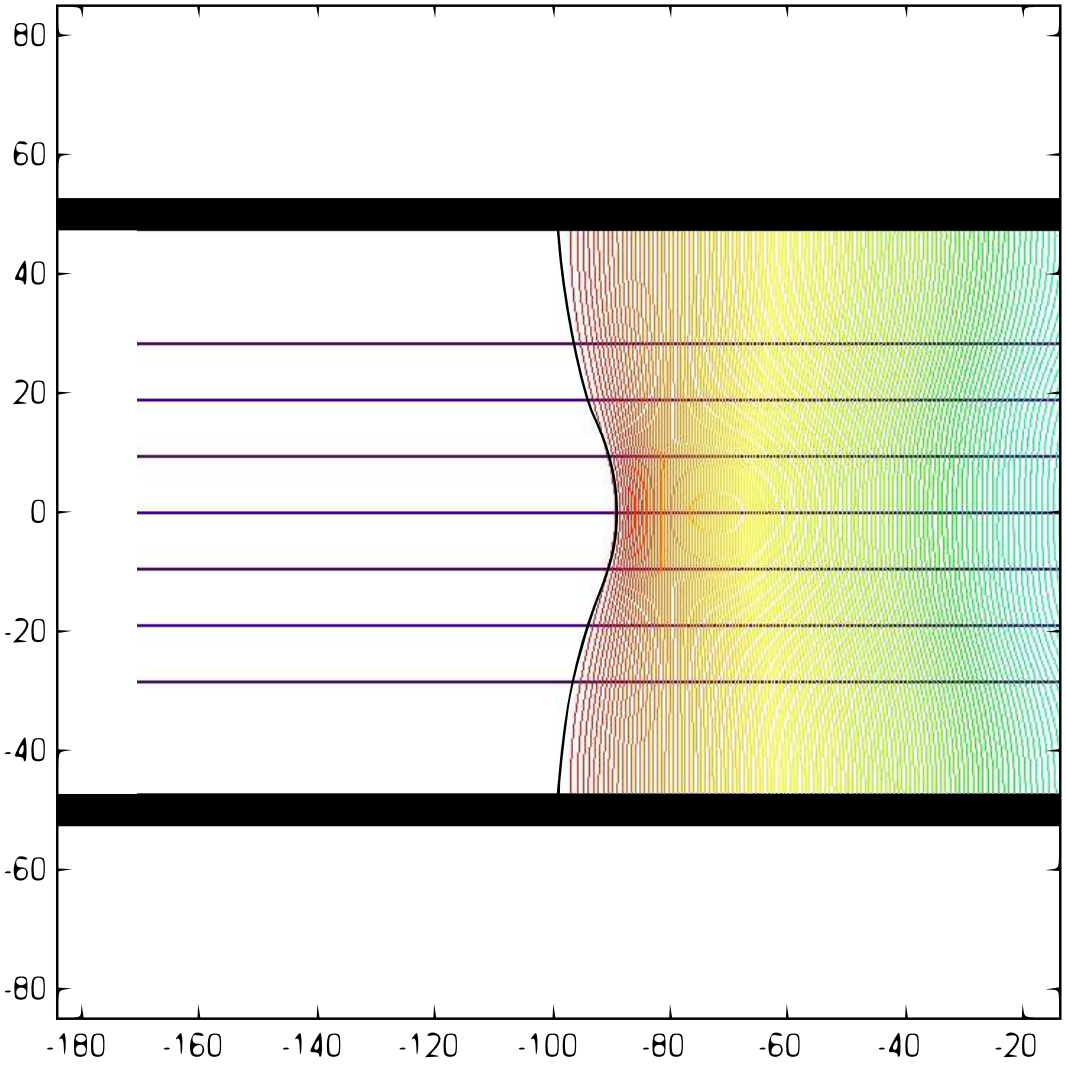


Figure 4.6: Comparison with numerical results

$$\theta r = r\sin\theta + \delta \tag{4.2}$$

The geometry generated by this equation is problematic in that the initial wave will hit the geometry, causing reflections, and thus the shape of the wave cannot be determined using simple methods. A second problem is that in order to reduce the horizontal distance, x_w the area of the tube needs to be changed significantly. Finally the curve will only be correct for a specific initial wave geometry, which in reality is unlikely to be constant.

With this in mind, a numerical study of several possibly feasible wall geometries was done. The results of this study are given in Figure 4.8. The first row contains plots of diaphragm curvature according to Equation 4.3. Dark blue indicates a plane wave. What can be seen from these plots is that increasing the curvature of the walls does cause the wave to flatten out, however it doesn't become completely plane and it takes a large distance to flatten out.

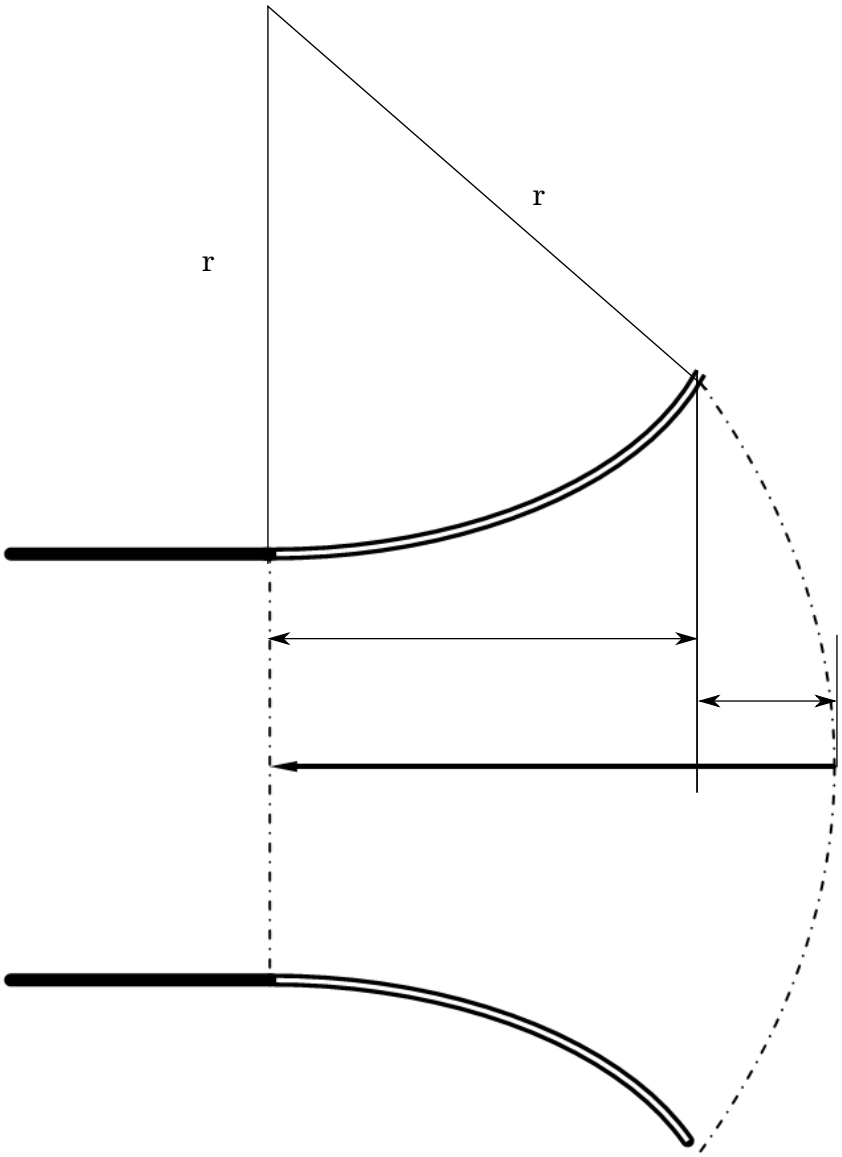


Figure 4.7: Wall geometry for theoretical straight wave

$$max(x_w ave) - x = d \tag{4.3}$$

The next three rows of Figure 4.8 give density contours at specific times. Here again the leading edge of the expansion can be seen to flatten out faster as the walls are curved more, however the more complicated flow features caused by the curved walls can also be seen, and can be seen to worsen as the wall curvature is increased.

This study showed that although the shape of the leading edge of the expansion could be manipulated by using curved walls for the tube, the effects on the flow behind the leading

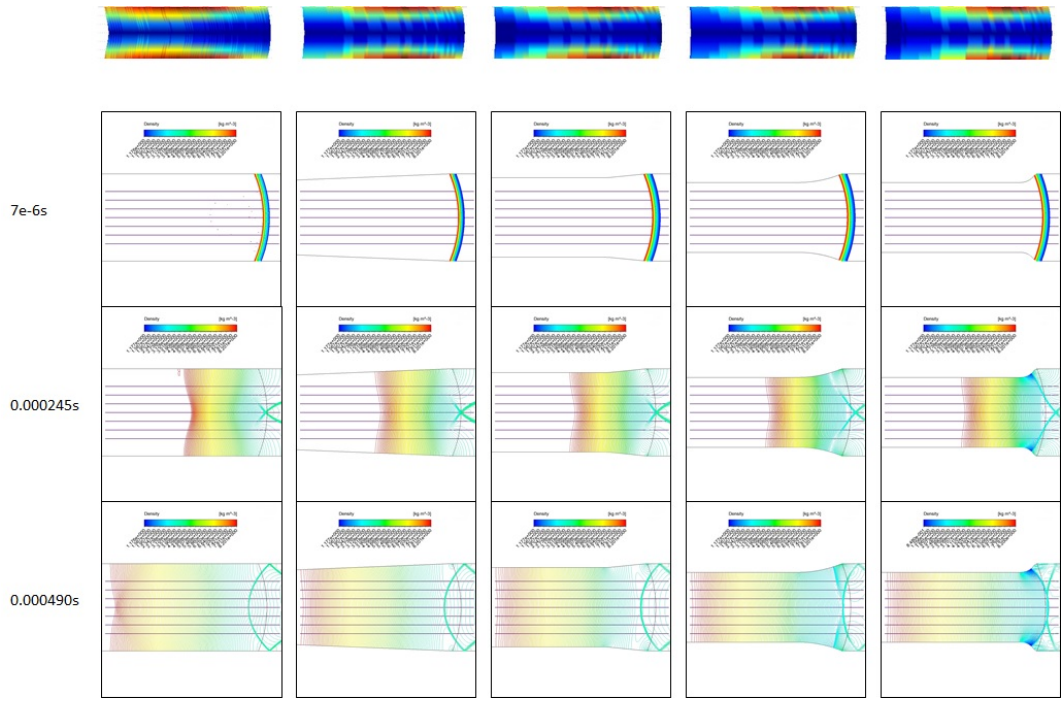


Figure 4.8: Curved wall numerical results

edge of the tube were significant and the distance it took for the wave to become plane was still high. This results in a wave with a weak gradient when it becomes plane. Controlling the shape of an expansion wave should be studied further. However this falls beyond the scope of designing a shock tube for studying expansion wave focusing. Based on these results it was decided that trying to straighten the expansion wave after diaphragm burst would not provide sufficient benefit to warrant the added complexity of a tube with curved walls.

4.1.3 Diaphragm selection

A brief study into the burst characteristics of diaphragms made from several different materials was carried out. This was done as the area of flow being studied is adjacent to the diaphragm and as a result the way in which the diaphragm bursts has a significant effect on the flow features. There were three main criteria used in the selection of the correct diaphragm material.

- The uniformity of the burst:
  - Whether the burst is consistent and repeatable.
  - Whether the diaphragm bursts in a symmetrical manner.
- The deflection of the diaphragm at burst.

  - The higher the deflection the more curved the initial expansion which has a significant effect on the flow.

- The burst pressure of the diaphragm.

Several materials were tested to check their viability for use as a diaphragm for the current research. The materials tested included:

- Plastic
- Brass foil
- Copper foil
- Aluminium foil
- Stainless steel foil

The reason for selecting each of these materials as well as their suitability for use for the diaphragm is discussed in the sections below. All tests were done for natural burst.

4.1.3.1 Plastic

Plastic diaphragms are used for the other shock tubes used by the Flow Research Unit. Plastic has the advantage of being readily available and inexpensive. A series of images showing the burst of a plastic diaphragm is given in Figure 4.9. Prior to burst the diaphragm can be seen to have deflected by an amount roughly equal to half the height of the test section. The start of the diaphragm failure also occurs at an arbitrary position along the diagonal of the tube cross-section. Scoring the diaphragm to try and achieve a more consistent burst had little to no effect on the burst. This is not usually a problem as most shock tubes are used to study the shock wave at a distance down stream of the diaphragm at which point the shock wave has flattened out and the effects of the diaphragm burst have dissipated. For this research the high deflection and inconsistent burst make plastic diaphragms unsuitable for use.

Figure 4.10 shows a plastic diaphragm after burst.

4.1.3.2 Aluminium foil

0.1mm aluminium foil was tried as an alternative diaphragm material. As it is a metallic material there is not a large amount of plastic deformation before failure and thus it doesn't

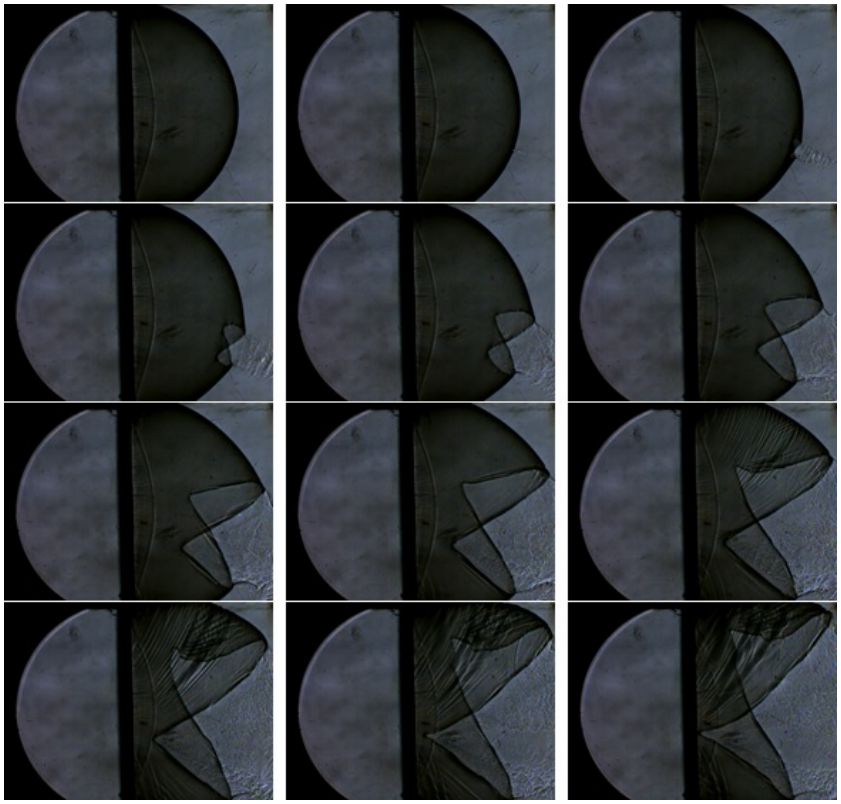


Figure 4.9: Plastic diaphragm burst



Figure 4.10: Plastic diaphragm after test

deflect a large amount before failing. This results in an initial expansion wave which is closer to plane. If the diaphragm is not scored, the burst starts at one of the edges and the diaphragm then folds to one side. This is an asymmetrical burst and is not as consistent as would be liked. To address this the diaphragm was scored to try and get a better burst. Figure 4.11 shows scored aluminium diaphragms after burst. In this case the burst is symmetrical and multiple tests showed that the result was consistent and repeatable. The burst continues to be consistent if multiple diaphragms are used.



Figure 4.11: Aluminuim diaphragms after burst, left: 1 diaphragm used, middle: 2 diaphragms used, right: 3 diaphragms used

The series of images in Figure 4.12 shows how a scored aluminium diaphragm bursts. The burst starts at the centre and propagates outwards along the score lines. The diaphragm then petals out symmetrically. Scored aluminium diaphragms burst at approximately 1bar gauge pressure with the burst pressure varying linearly with number of diaphragms used.

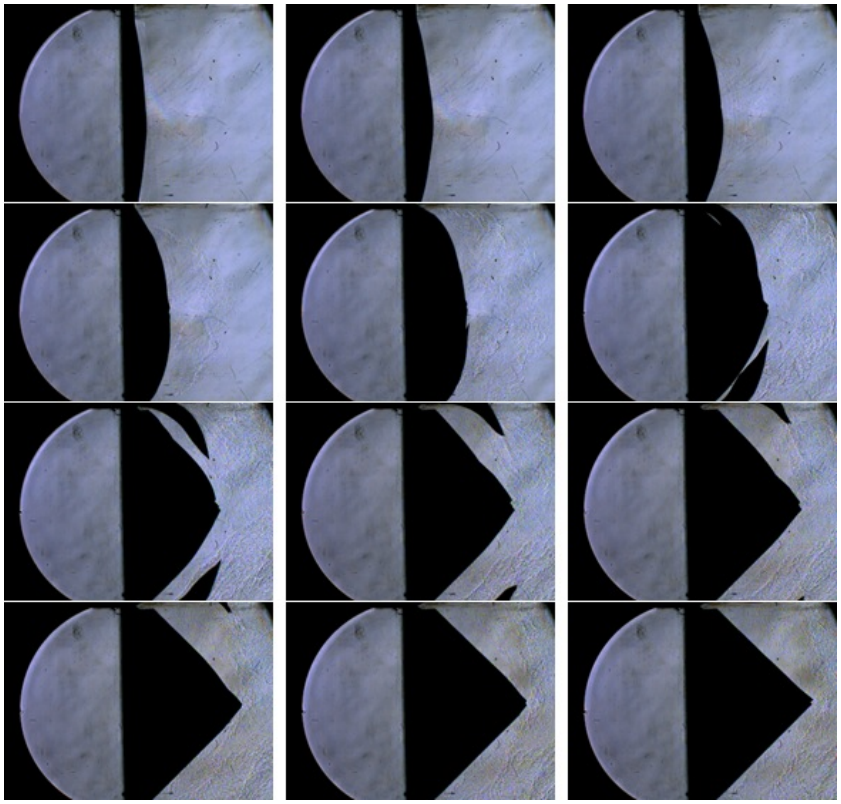


Figure 4.12: Aluminium diaphragm burst

4.1.3.3 Brass foil

0.05mm brass foil was tried and the burst was similar to unscored aluminium. However scoring the brass did not result in a controlled and consistent burst. Figure 4.13 shows several bursts with brass diaphragms. The peeling from one side is clear, however the actual burst is very inconsistent.



Figure 4.13: Brass diaphragm after test

Figure 4.14 shows the burst of a brass diaphragm and the peeling from one side is clear. This burst occurred at 4 bar gauge for a single diaphragm and scoring had little to no effect on the burst.

4.1.3.4 Copper foil

0.1mm copper foil was also tried. The deflection of the copper before burst was higher than both the brass and aluminium, and the actual burst was similar to the brass or unscored aluminium. Scoring the copper had some success however the consistency and repeatability of the burst even with scoring was low. Figure 4.15 shows a burst copper diaphragm, again the diaphragm peeled from one side of the tube. For copper the burst was consistently from the bottom of the tube, with the diaphragm peeling upwards to hit the top of the tube. The cone that is formed on the diaphragm is as a result of a pressure transducer hole downstream of the diaphragm position.

4.1.3.5 Stainless steel foil

Stainless steel was found to have too high a burst pressure to use as a diaphragm even when very thin material was used, as can be seen in Figure 4.16.

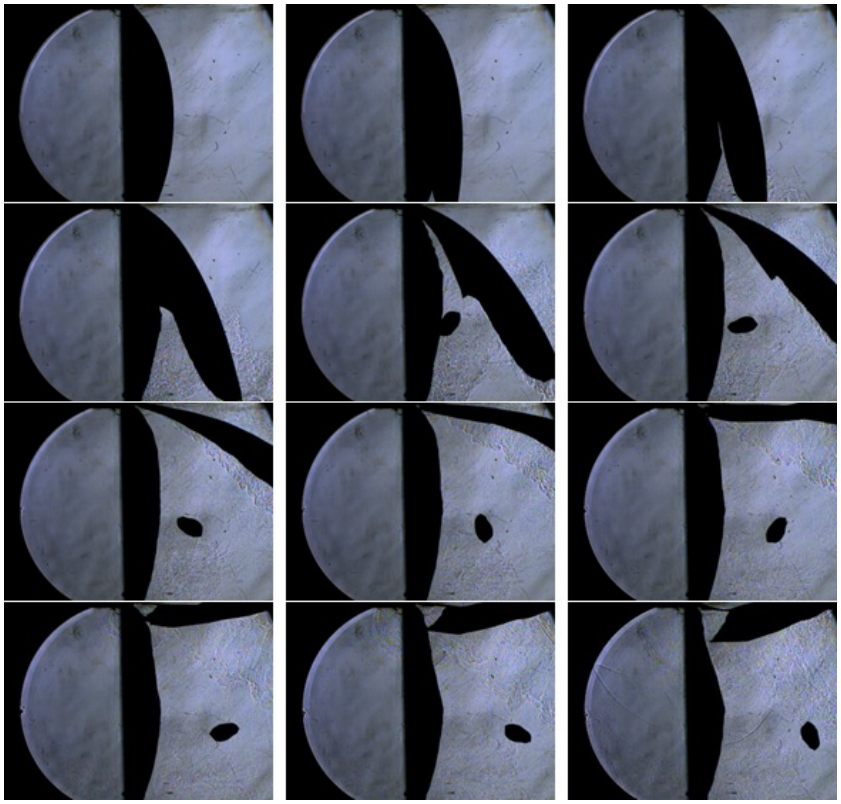


Figure 4.14: Brass diaphragm burst



Figure 4.15: Copper diaphragm after test

Based on this investigation it was decided that Aluminium foil was the most suitable material for use as a diaphragm as it responded well to scoring and burst naturally in a consistent and uniform manner.



Figure 4.16: Stainless steel diaphragmafter test

4.1.4 Optical system

A schlieren setup was used as shown in Figure 4.17. The specification for the optical equipment used are given in Table 4.3.

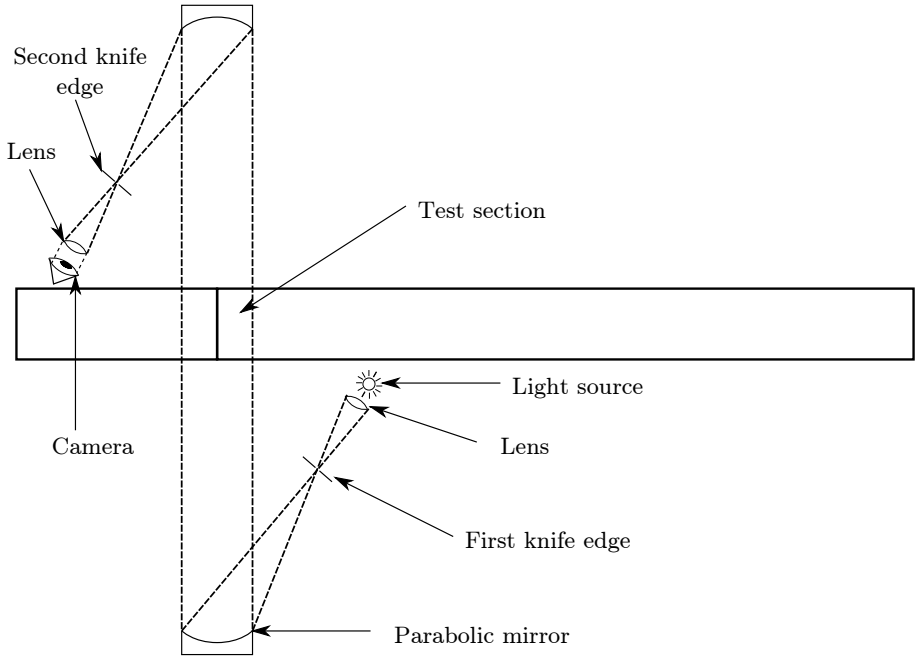


Figure 4.17: Schlieren setup

Table 4.3: Optics specifications

Component	**Specification**
Light source	MegaRay MR2175
Camera	Photron SA5 high speed camera

In order to try and improve the sensitivity of the optics and to try and visualise the expansion wave, the second knife edge was replaced with several different colour filters, as shown in Figure 4.18. Unfortunately these filters cut off too much light and as a result a normal knife edge was used for the experiments.

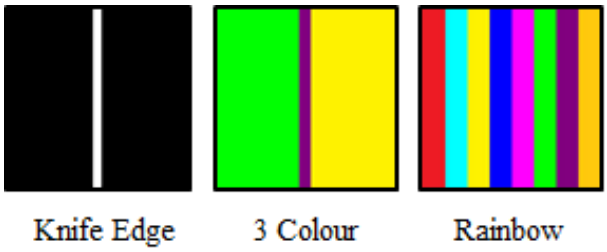


Figure 4.18: Schlieren filters

Another consideration was whether to use a vertical or horizontal filter in the experiments. A major concern when using a vertical filter was the large band next to the diaphragm position due to the diffraction of light around the edge of the window. This band can be seen in the left image of Figure 4.19. As many of the features of interest occur in this area a horizontal filter produced a preferable image. This meant that horizontal gradients were not visualised. However after the reflection off the test piece many of the gradients are vertical and thus the features can still be seen when using a horizontal filter.

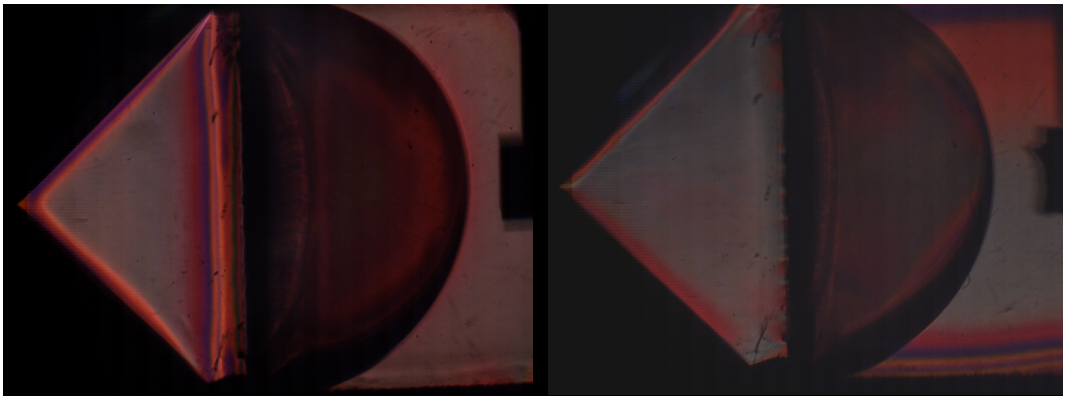


Figure 4.19: Comparison of vertical (left) and horizontal (right) filters

4.1.5 Data capture

A pressure transducer was mounted at the centre of the test-piece as shown in Figure 4.20. The data capture equipment used is listed in Table 4.4.

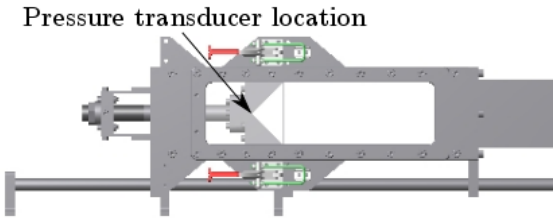


Figure 4.20: Pressure transducer location

Table 4.4: Data capture equipment used

Pressure transducer	PCB 113B21
Oscilloscope	Hantek DSO3064A

4.2 Numerical

The numerical simulations were done using the commercial codes, Ansys Fluent 15.0 and STAR CCM+ 9. The Fluent simulations were run on a computer with the specifications given in Table 4.5. The STAR CCM simulations were run on Crunchyard, a high speed computing facility at the University of the Witwatersrand.

Table 4.5: Computer specifications

Component	**Specification**
Processor	i7-4770 3.4GHz
Memory	8GB DDR2
Operating System	Windows 7 Professional 64-bit

The geometry set-up and meshing was done using the Ansys 15 design modeller and mesher.

5 Methodology

5.1 Experimental

5.1.1 Start of day procedure

1. Switch on room lights.
2. Check "'pressure in"' pipe is correctly attached.
3. Check that there is air pressure.
4. Close safety vent valve.
5. Close both control valves.
6. Ensure all panels are in place and bolts have been properly tightened.
7. Check for leaks.
8. Check shock tube for any obstructions.
9. Check driver can be slid into position.
10. Check Optics/DAQ are correctly set-up.

5.1.2 Diaphragm preparation

1. Cut diaphragm to size according to diaphragm template (Figure 5.1).
2. Punch holes according to template using an 8mm hole punch.
3. Measure and mark the positions of the four corners of the tube on the diaphragm (this should give a 100 x 100mm square in the centre of the diaphragm).
4. Score the diaphragm along the diagonals of the square.

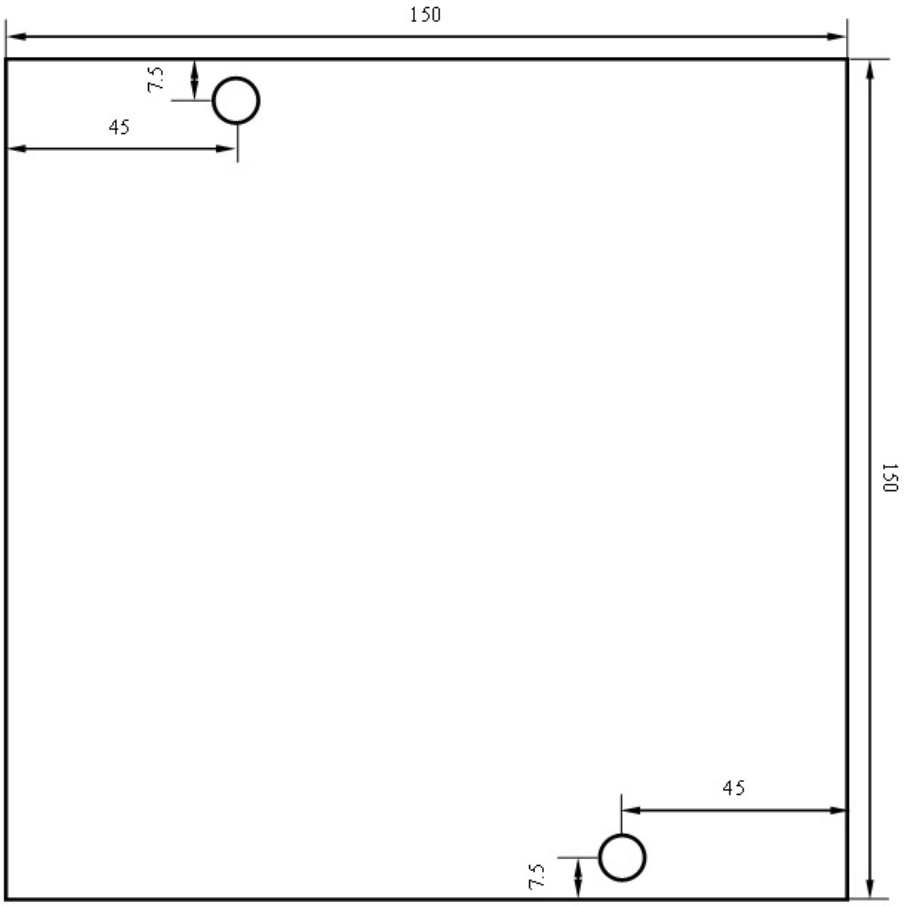


Figure 5.1: Diaphragm template

5.1.3 Diaphragm replacement

1. Diaphragms should be cut according to the template.
2. Open clamps and slide driven section away from driver.
3. Remove used diaphragm.
4. Place new diaphragm over dowels.
5. Slide driven section back into place and clamp.

5.1.4 Test piece positioning and replacement

1. The position of the test piece is controlled by the nut at the back of the driver.
   (a) The test piece can be moved to touch the diaphragm or can be moved 100mm away from the diaphragm.
2. To change the test piece, the rear panel of the driver must be removed.

(a) This is done by removing the 8 M8 cap screws at the back of the driver and pulling the test piece out.

(b) The actual test pieces are held on with 4 M6 cap screws

5.1.5 Test procedure

1. Replace the diaphragm (See diaphragm replacement).
2. Switch on oscilloscope, signal conditioner and trigger box.
   (a) Ensure the signal conditioner reading is green.
   (b) Set the oscilloscope to single trigger mode.
   (c) Check the trigger level being used.
3. Switch on the high speed camera and open the software on the laptop.
   (a) Ensure the settings for the camera are correct.
4. Switch on the light source and check the image.
   (a) Eye protection should be worn and looking straight at the light should be avoided.
   (b) Ensure the image is acceptable.
5. Ensure the oscilloscope is waiting for a trigger.
6. Ensure all the valves are closed.
7. Put on hearing protection.
8. Sound a warning that a test is about to begin.
9. Open the main pressure valve.
10. Slowly open the first control valve until the pressure gauge slowly increases to maximum supply pressure.
11. Slowly open the second control valve to maximum.
12. Monitor the pressure gauge as the driver is pressurized.
13. A warning should be sounded at every bar of pressure. However if the burst pressure is known and consistent, a single warning can be given when the burst pressure is approached.
14. Slowly keep increasing the driver pressure until the diaphragm bursts, the valves should then be immediately closed.

15. For a failed burst or an aborted test
    (a) Close all the valves.
    (b) Vent the driver by opening the second control valve and slowly opening the vent valve (hearing protection should be worn).
    (c) Vent the line in the same way by opening the 1st control valve.
16. Switch off the light source.
17. Check the results on the computer.
    (a) Save results and note comments about the test on the test matrix.
18. If additional tests are being done steps 1-8 are now repeated.
19. Once testing is complete all equipment should be switched off.
20. The tube should be left open, with the control valves and vent valve open.

5.1.6 End of day procedure

1. Ensure air pressure supply is closed.
2. Vent the pressure in pipe.
3. Open the tube and remove the diaphragm and any diaphragm fragments left in the tube.
4. Check there are no other objects left in the tube.
5. Ensure control and the vent valves are left open.
6. Switch off all DAQ equipment.
7. Ensure tools have been placed in tool box.
8. Switch off room lights.

5.2 Numerical

5.2.1 Geometry

The geometry for the numerical simulations was set up to imitate the experimental shock tube. The Ansys 15.0 design modeller was used to create the geometry for the simulations. Figure 5.2 shows examples of the geometry used.

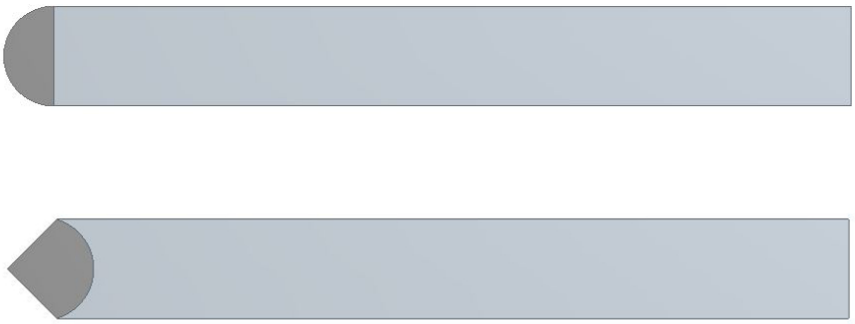


Figure 5.2: Examples of geometry for numerical simulations, Cylindrical test piece with plane diaphragm (top), Triangular test piece with curved diaphragm (bottom).

The geometry was set-up as two regions to allow the initial pressure to be set at different values in the two regions of the shock tube. All the geometries used were 2-D. The two regions were joined by an interface and all the boundaries were made as walls. An annotated diagram of this is given in Figure 5.3. All the outer boundaries were made walls, including the end of the tube. This was done as it resulted in a more stable solution and as the reflection did not reach the area of interest in the time being studied it has no effect on the solution.

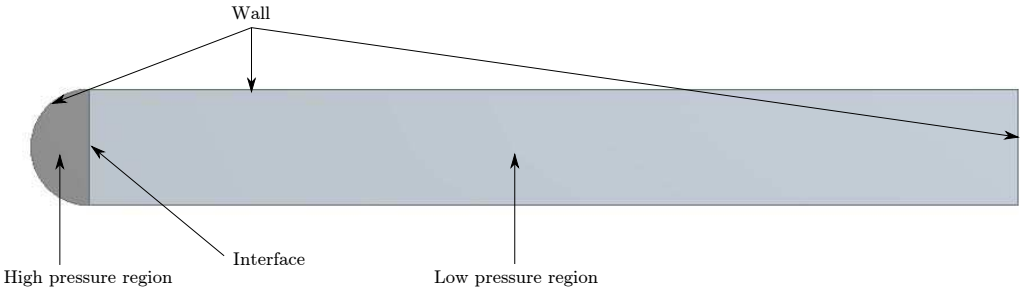


Figure 5.3: Annotated geometry for numerical simulations

A slight modification to the geometry was done for some of the tests, in which an additional region was added at the end of the shock tube as shown in Figure 5.4. This was done to model the flow at the exit of the shock tube in order to determine how a shock wave seen in the experimental results formed. The outside region was sized to ensure that the shock reflecting off the walls didn't interfere with the flow features of interest.

Table 5.1 gives the different geometry configurations which were used. For all geometries the driven section was 800mm long and the tube was 100mm high to replicate the experimental shock tube.

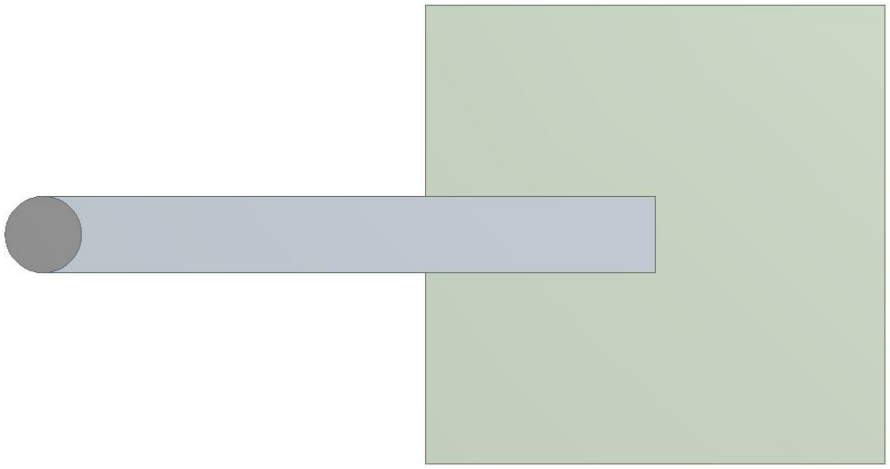


Figure 5.4: Geometry with added outside region

Table 5.1: Geometries for numerical simulations

Test piece	**Interface type**	**Test piece diaphragm distance [mm]**
50mm Cylinder	plane	0
50mm Cylinder	curved	0
50mm Cylinder	curved	60
50mm Cylinder	plane	500
50mm Triangle	plane	0
50mm Triangle	curved	0
50mm Converging	plane	0
50mm Converging	curved	0
0.5AD Parabola	plane	0
1 AD Parabola	plane	0

5.2.2 Meshing

The Ansys 15.0 meshing program was used to generate the basic meshes for the numerical simulations. Automatic mesh refinement within the solver was used to further refine the mesh in the areas of interest during the simulations. An example of a base mesh is given in Figure 5.5.

One important factor when setting up the mesh is that the cells on either side of the interface must be aligned in order to ensure the interface behaves correctly during the simulation.



Figure 5.5: 2mm base mesh for numerical simulations

Figure 5.6 shows a zoomed in view of the interface where it can be seen the mesh on either side of the interface is correctly aligned.

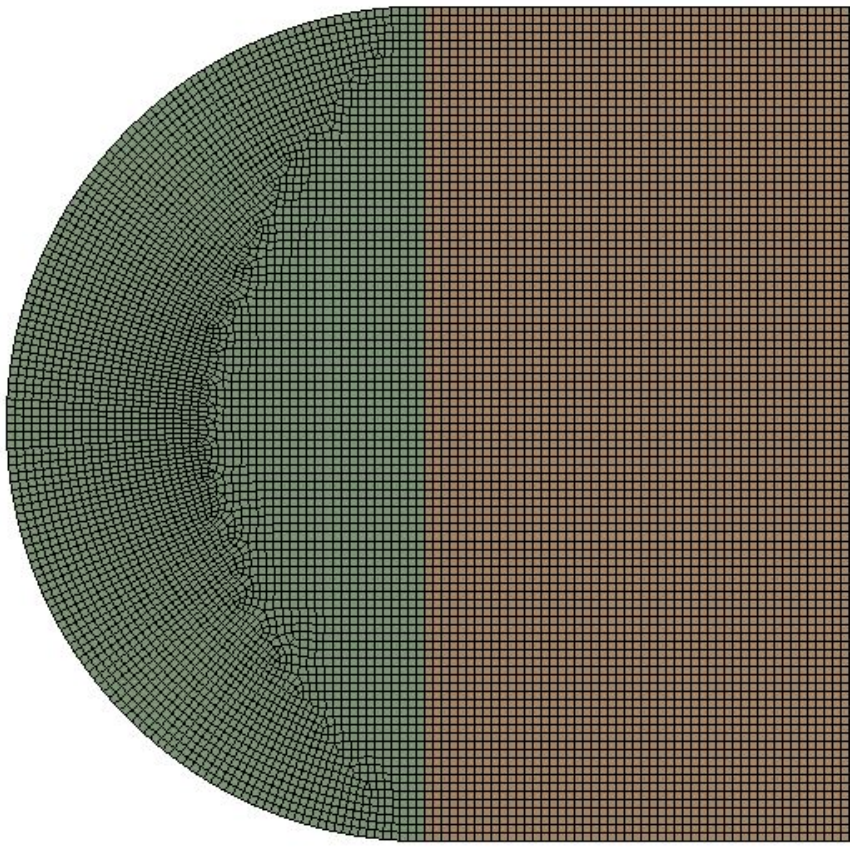


Figure 5.6: Zoomed in view of interface for 1mm base mesh

5.2.2.1 Mesh independence

In order to establish mesh independence, simulations were run using base meshes with 2, 1 and 0.5 mm cell sizes. Simulations were also run with and without automatic mesh adaption. Figure 5.7 shows a summarised comparison of the results. The flow features are consistent for all cases and thus the solution exhibits mesh independence. The 0.5mm base mesh was

used for the remaining simulations as the meshed region was not very large and thus a finer mesh could be used. This also showed the features more sharply.

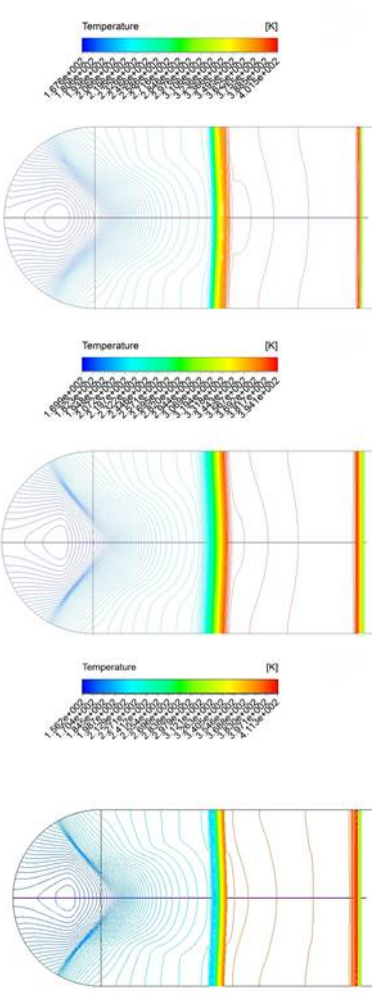


Figure 5.7: Summary of mesh independence results: 2mm mesh no automatic refinement (top), 0.5mm mesh no automatic refinement (middle), 0.5mm mesh automatic mesh refinement (bottom)

5.2.3 Solver set-up

Table 5.2 gives the settings used when setting up the numerical solution.

The entire flow region was initialised to 0Pa pressure and 300K temperature with 0 initial velocity. The two flow regions were then given the correct relative pressures for the simulation. Automatic mesh refinement and coarsening was done at every time step based on gradients of density and velocity.

Table 5.2: Solver settings

Setting	Value
Type	density based
Time	transient
Velocity formulation	Absolute
Models	Energy on
	Inviscid
Fluid	Air - ideal gas
Solution Methods	
Formulation	explicit
Flux type	Roe-FDS
Gradient	Least squares cell based
Flow	3rd order MUSCL
Transient formulation	Second order implicit
Courant number	2

5.2.3.1 Solver independence

In order to establish solver independence the simulation was run using Ansys 15.0 Fluent as well as STAR CCM+ 9. The simulation was also run for both inviscid and k-ϵ viscous solvers. A summary of the results is given in Figure 5.8. Again the flow features are consistent for the different solvers indicating solver independence.

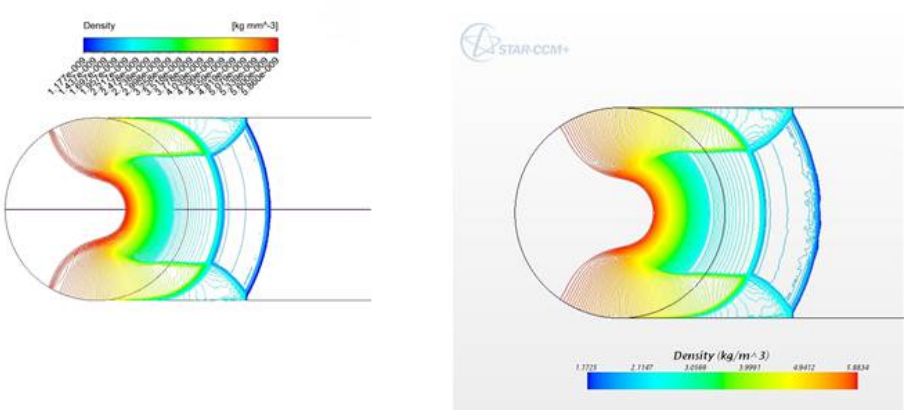


Figure 5.8: Comparison of Fluent (left) and STAR CCM+ (right) results showing solver independence

6 Data Processing

6.1 Image processing

The images of the flow field obtained during the experiments showed flow features, however due to the weak gradients, the features were not as clearly defined as was desired. In order to improve the images, post processing was done to hi-light the features. Figure 6.1 is an unprocessed experimental image. Features can be seen in the driver section; however, they are not clear. The diaphragm burst can be seen clearly in the driven section. The edges of the test pieces are blurred due to the small amount of air between the test piece and the window being drawn out and expanding around the corner.



Figure 6.1: Base experimental image

Some of the features which can be seen are not due to the focusing phenomenon, but rather due to the burst being a natural burst, in which there is some flow in the tube before burst. This flow is significantly slower than the features being looked at and thus by subtracting an image from before the burst these features can be removed from the image. Figure 6.2 shows the image after subtraction. This removes a lot of the 'noise', flow features not relating to the focusing effect, and makes it easier to pick up the important features. This method does reduce the resolution of the image however and is only really effective for later parts of the flow where the features of interest are significantly different from the initial flow. It also makes the image very dark so additional processing is required to make the image useful.



Figure 6.2: Image with 'blank' image subtracted from it

This image can then be processed to more clearly show the flow features. This was done using several image processing methods in Matlab. The program used can be found in the digital appendix. The final processed image can be seen in Figure 6.3. The major flow features of interest, in this case waves moving towards the symmetry plane, can be seen. After post-processing the experimental images can be compared with the numerical results in order to validate them.

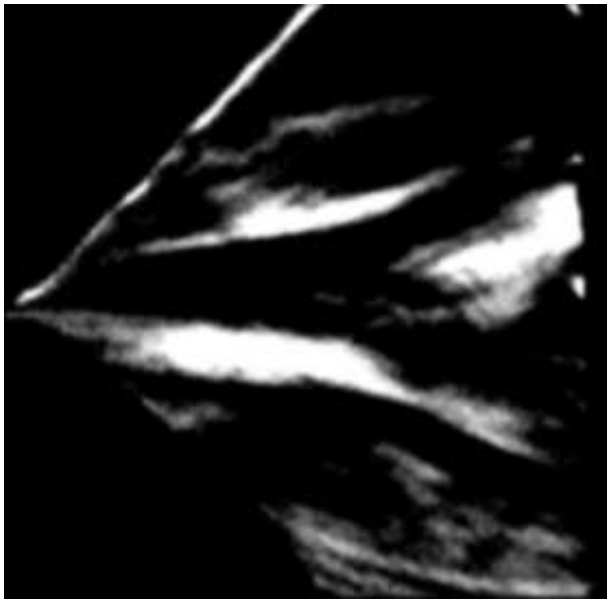


Figure 6.3: Final processed image

6.2 Numerical Results Processing Method

The numerical results needed to be processed so that they could be used to draw conclusions about the flow. The easiest way to get a graphical representation of the flow was to plot contours on the flow field. Contours of density, pressure and temperature were selected. These contours allow a good understanding of what the different features are to be established. Figure 6.4 shows examples of these contours. The combination of the three contour plots allows expansion and compression waves to be identified as well as determine which features are contact surfaces. In order to get more quantifiable data a pressure trace was taken at the centre of the cavity. The position is shown in the bottom image of Figure 6.4 (blue cross). The pressure and temperature along the symmetry line were also recorded at every 0.5mm for each time step. The line along which these readings were taken is also shown in the bottom image of Figure 6.4 (purple line).

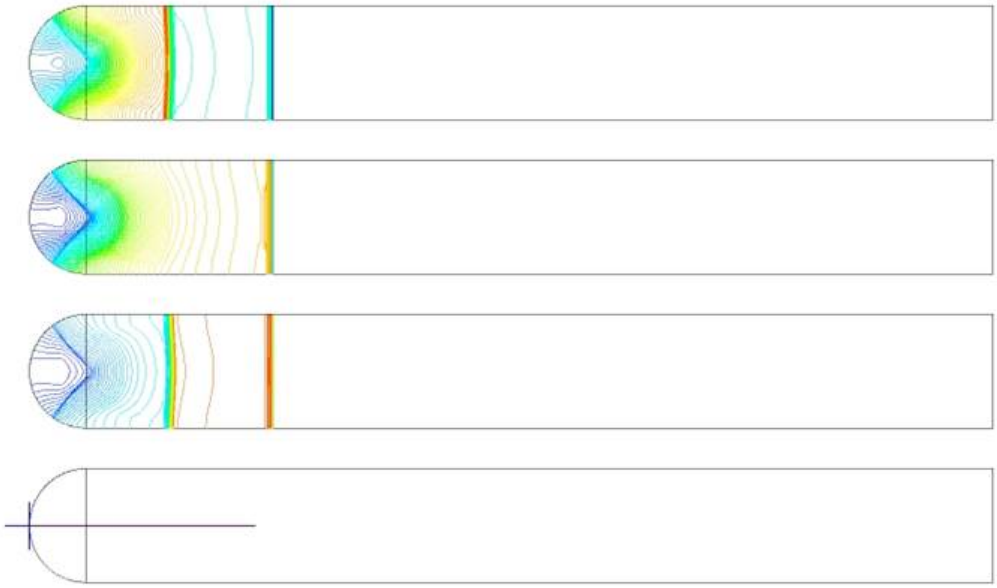


Figure 6.4: Example of contours of Density (top), Pressure (second), Temperature (third) and the locations for pressure and temperature data (bottom)

In addition to the contour plots, numerical shadowgraph and schlieren images were created for comparison with the experimental results. The schlieren images were created for both vertical and horizontal gradients; this had the advantage of showing which configuration would show the features more clearly for the experimental testing. It also highlights the weak gradients present and thus helps explain the difficulties encountered when trying to visualise the features experimentally.

A useful method for understanding the flow features was to generate a surface plot of the temperature or pressure along the symmetry line with time. The resulting surface gives a

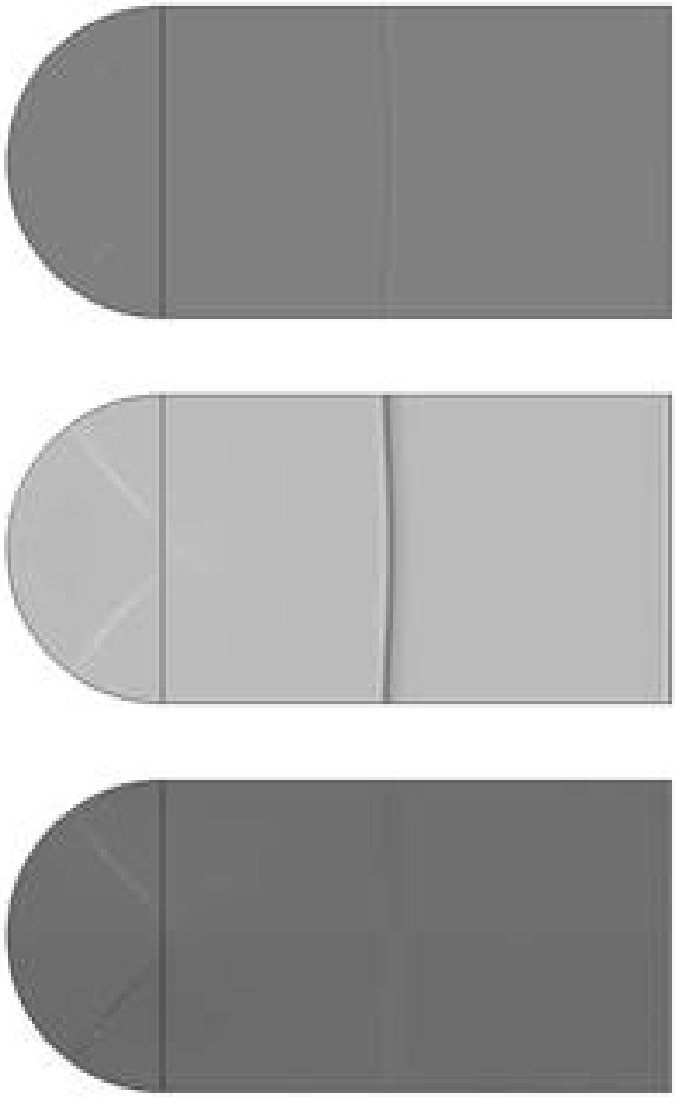


Figure 6.5: Example of numerical shadowgraph (top), schlieren, horizontal gradients (middle), schlieren, vertical gradients (bottom)

good idea of the strength of the gradients involved, both with regards to time and position as well as providing another tool for identifying what each feature seen in the contours is. An example of one of these surface plots is given in Figure 6.6.

A top view of this surface is a useful description of the flow if it is kept in mind that it represents a three dimensional surface. Figure 6.7 is the top view of the surface shown in Figure 6.6. From this image the initial shock and expansion can be identified, as can the effects of two dimensional waves on the symmetry line of the tube. Plots such as this will be used to describe the flow features in the following section.

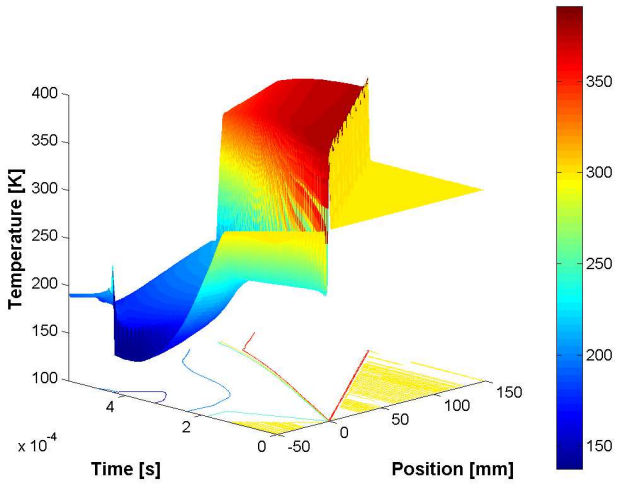


Figure 6.6: Example of 3 dimensional surface plot

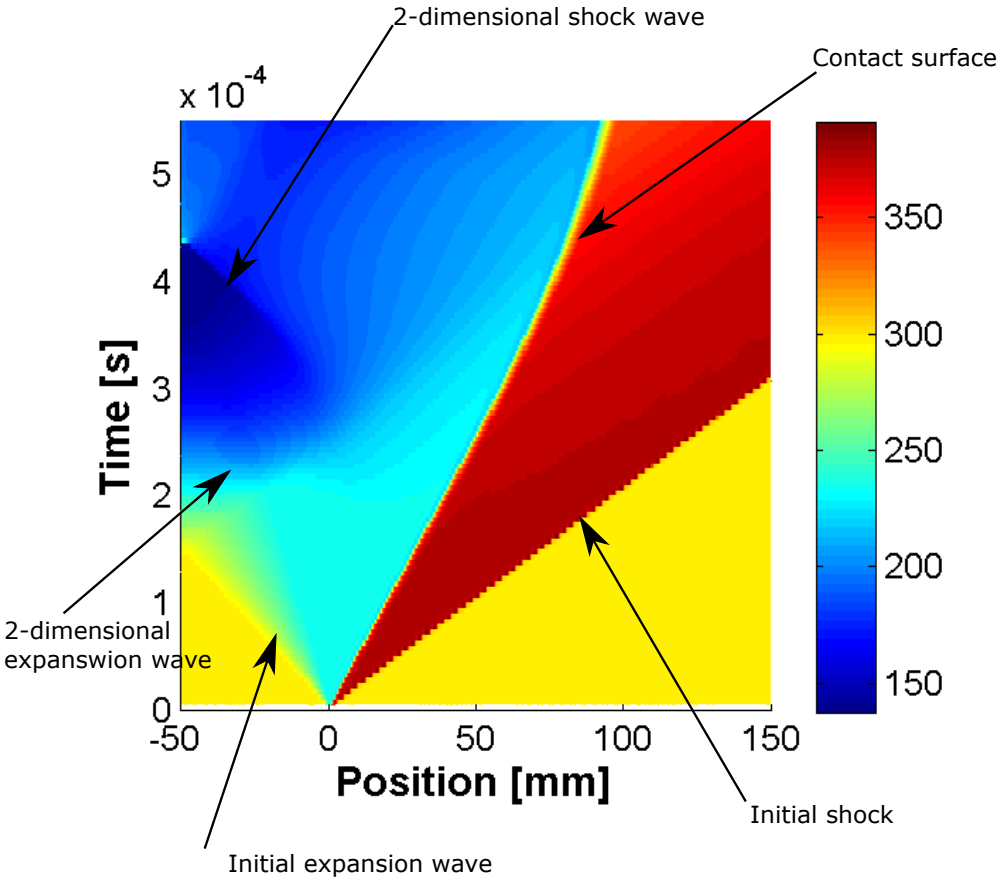


Figure 6.7: Top view of surface plot

7 Results and Discussion

7.1 Description of Flow Field

In this section the basic flow fields which result when an expansion wave enters into cavities of different shapes will be described. These descriptions are for the ideal case where the initial expansion wave is plane, the diaphragm disappears instantaneously and the test-piece is placed immediately adjacent to the diaphragm position. When the situation is not ideal, the real case for experimental work, the flow is different and the differences will be discussed in later sections as will the effect of other parameters on the flow features.

7.1.1 Cavity geometry

A time series is given in Figure 7.1 of density contours for a shock tube without a test-piece placed in the driver section. This time series serves as a base line for comparison with the flow when a test piece is placed in the driver. As there are no inclined surfaces the flow remains one dimensional with the expansion wave simply reflecting off the back wall of the driver. The reflected expansion passes through the initial expansion and once the trailing edge of the initial expansion has reflected off the back wall only a single one dimensional expansion wave remains travelling down the tube.

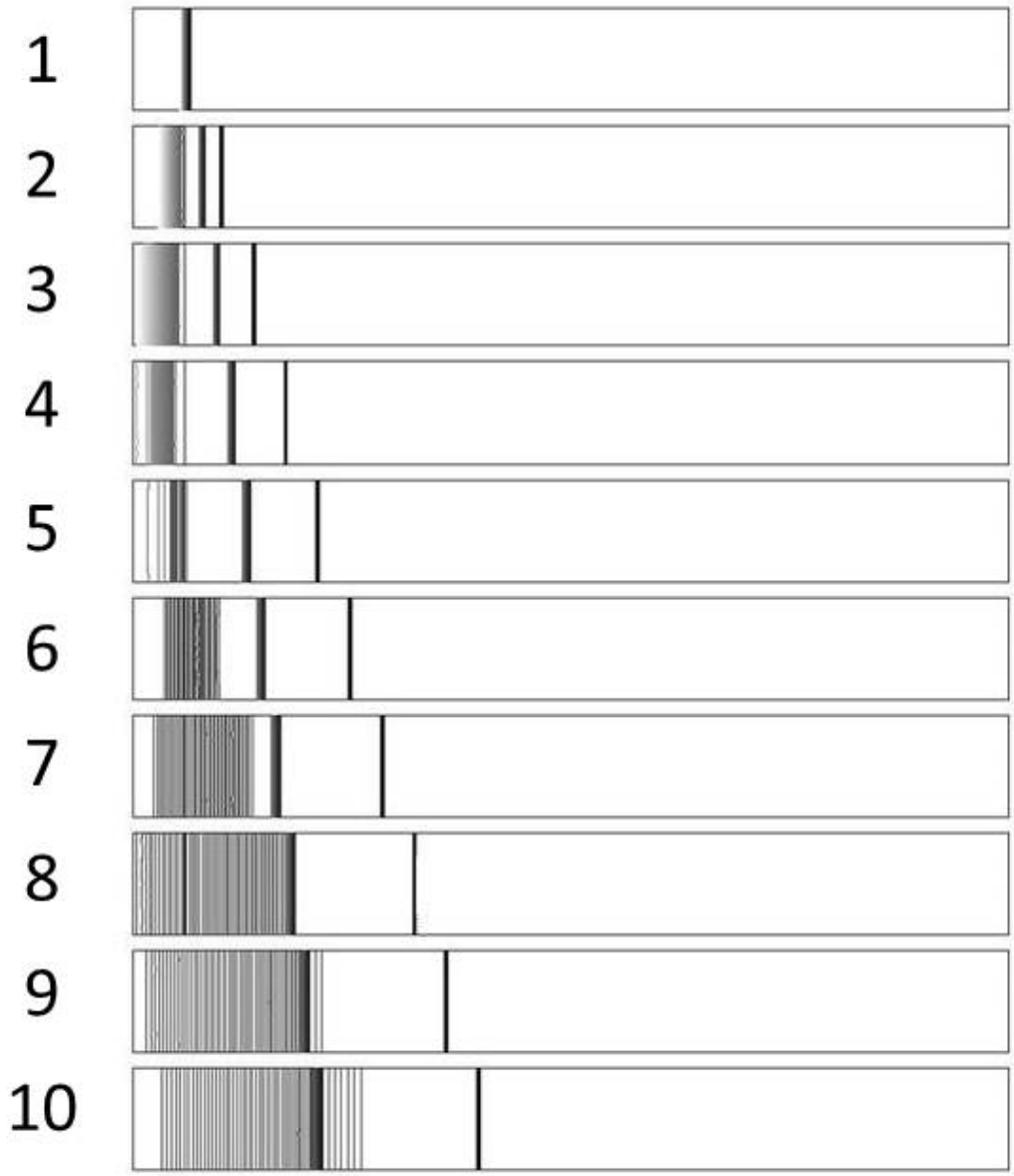


Figure 7.1: Time series for no test piece, P41 = 7, Contours of density

The first geometry used was a cylindrical test-piece, for which the initial deflection angle is small but increases to 90^o. After diaphragm burst a shock wave travels into the low pressure section of the tube, followed by the contact surface. An expansion wave travels into the high pressure section. As the test-piece is placed immediately adjacent to the diaphragm the expansion wave immediately hits the start of the test piece at the top and bottom of the tube, and starts to reflect towards the symmetry plane of the tube. The reflected expansion causes the fluid at the top and bottom of the tube at the start of the test-piece to be expanded more than the rest. This causes the fluid at these regions to be at a lower pressure and temperature then the surrounding fluid and thus compression waves start to form to ensure that the fluid pressure increases to be at the same pressure as the fluid downstream of it. Another way

of thinking about this is to take a reference frame which is moving with the fluid. For the fluid being accelerated in the driver section, the walls of the test piece appear to bend into the flow, which causes compression waves to form. This can be seen in the first three images of Figure 7.2. The contours of density show the shock from the diaphragm burst, furthest right, the contact surface, and the expansion with the reflected expansion wave at the top and bottom of the tube. In the third image the compression waves can be seen starting to form. As the reflected expansion waves travel further into the tube towards the symmetry plane, the compression waves which started at the wall also grow towards the symmetry plane as the region of decreased pressure increases in size with the movement of the reflected expansion waves. The compression waves continue to grow and meet at the symmetry plane. The compression waves strengthen to become shock waves and enclose a region of flow in the driver section (the fifth image). The shock waves reflect on the symmetry plane with regular reflection. The enclosed region will be called the focus region for expansion wave focusing. Within this region the two dimensional expansion waves continue to reflect, causing the the fluid properties to continue to decrease. This in turn causes the shock waves to move into the driver. When the shock waves have completely moved into the driver (image 8) the focusing is complete and the focus region disappears. The lowest values for the fluid properties occur just before this. The shock waves then reflect out of the cavity. After this, similar flow patterns repeat, however the features are weaker each time, until equilibrium within the fluid is established. A cylindrical cavity has very little effect on the contact surface or the initial shock wave which was formed at diaphragm burst.

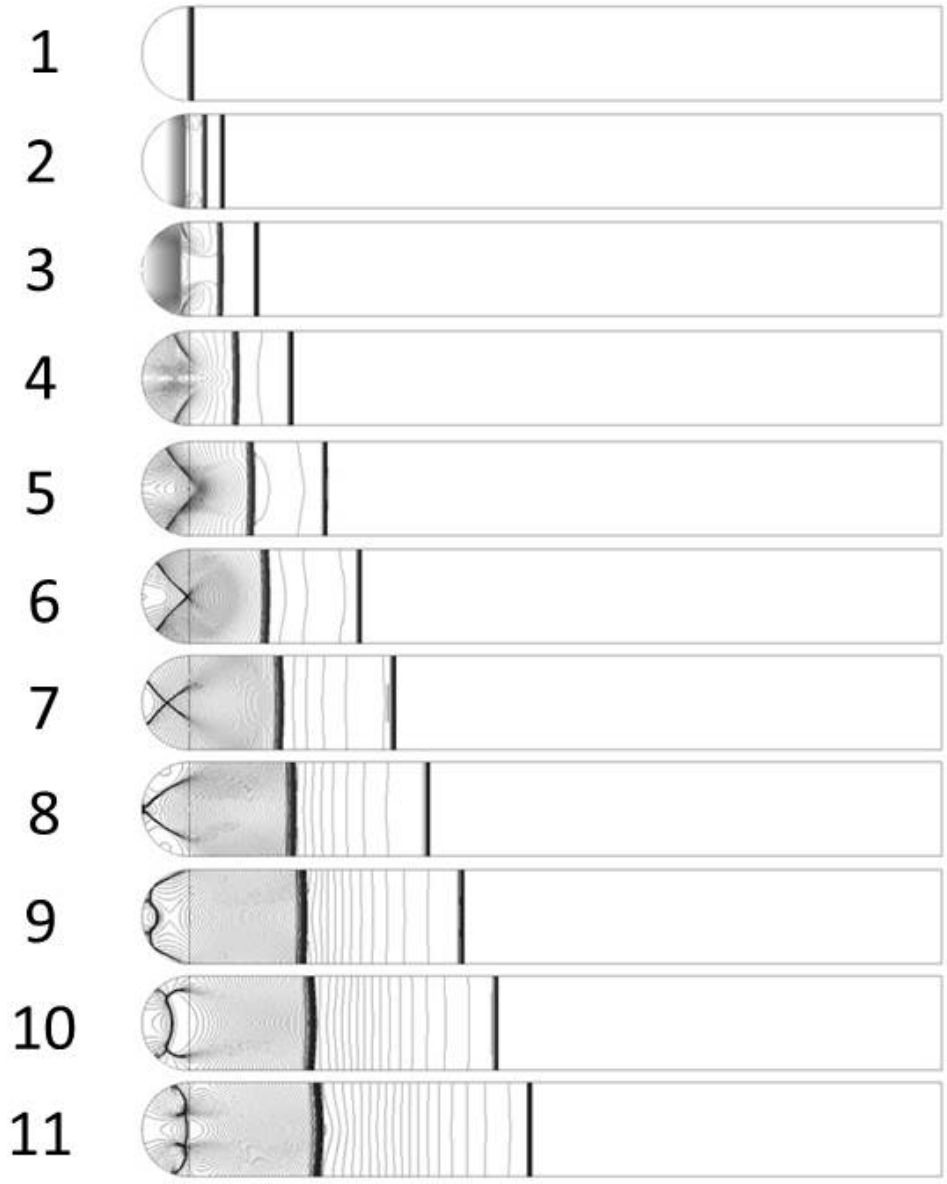


Figure 7.2: Time series for cylindrical test piece, P41 = 7, Contours of density

Figure 7.3 and Figure 7.4 give a more detailed look at the movement of the expansion waves and explanation for the flow features which are seen. The leading and trailing edge of the initial expansion wave are shown by the dashed black lines in Figure 7.3. The expansion wave remains plane as it enters the cavity, and it spreads out as is expected for an expansion wave. The red dotted lines represent the reflected expansion wave from the point at which the initial expansion wave hits the walls of the cavity. The characteristics start perpendicular to the wall, and as the wall at the trailing characteristic position is at a lower gradient than the leading characteristic the characteristics behind the leading characteristic are forced to curve, as the waves travel further into the cavity this becomes more pronounced. From the second image in Figure 7.3 a region is highlighted with cross-hatching. This region represents

an area of the flow which is being expanded by 2 expansion waves, the initial expansion and the reflected expansion. Only the region above the symmetry plane is hi-lighted. The fluid in this region is expanded more than the fluid closer to the symmetry plane as well as the fluid downstream in the tube. This over expansion causes compression waves to form immediately downstream of the trailing characteristic of the reflected expansion wave. In the remaining images the cross-hatched region can clearly be seen to grow towards the symmetry plane and as a result the compression waves also need to extend towards the symmetry plane. In the 5th image the leading edge of the reflected expansion wave has reached the symmetry plane and reflected away from it, the purple dash-dot line. This causes a region at the end of the cavity which has been expanded by 3 expansion waves. It should be noted that the region ahead of the leading characteristic, which looks like a focus region in images 5 and 6, is in fact a region of relatively higher pressure and temperature as it has only been expanded by the initial expansion wave. As this region collapses new reflected expansion waves start to move outwards from the symmetry plane causing a region of highly expanded fluid on the symmetry plane, this also causes the compression waves which have formed to grow towards the symmetry plane, the start of this is seen in image 6.

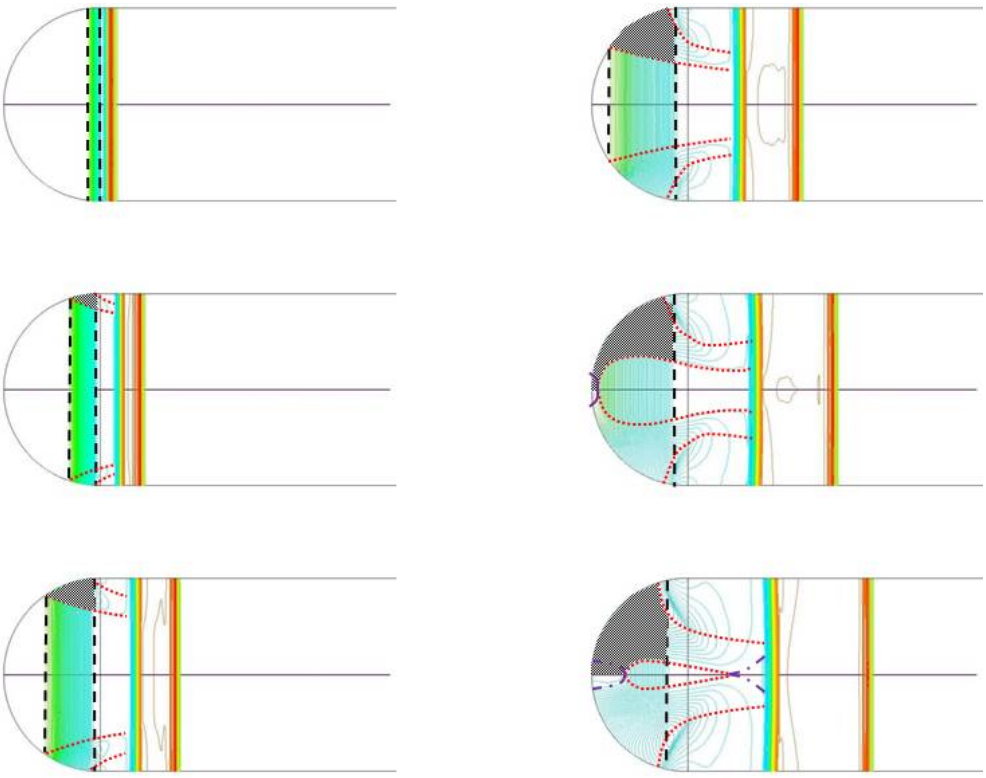


Figure 7.3: Movement of a plane expansion wave into a cylindrical cavity, Contours of Temperature

Figure 7.4 shows the compression waves formed strengthen to shock waves and move into the cavity. The first two images show that the compression waves are following the trailing

edge of the reflected expansion wave, red dotted line. The flow in the region enclosed by the shock waves continues to be over expanded by expansion waves reflecting off the wall and the shock waves, shown in the first two images by the purple and orange leading characteristics. As the trailing edge of the expansion wave, red dotted line, moves deeper into the cavity it collapses into itself, which in turn makes the shock waves following it appear to accelerate in to the cavity.

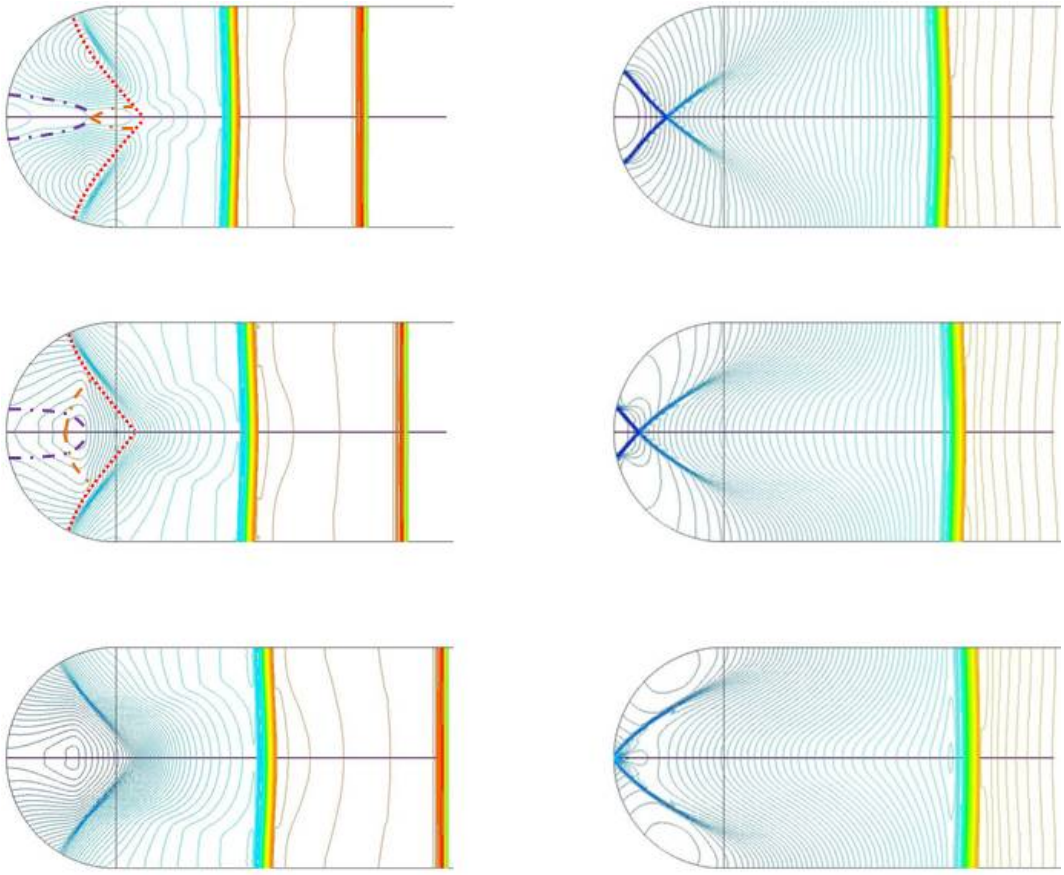


Figure 7.4: Movement of compression waves into cylindrical cavity, Contours of Temperature

The second geometry was a triangular cavity, for this geometry the deflection angle is constant along the entire test-piece. The basic flow is similar to the cylindrical case, however there are some differences. The most notable is that the driver geometry has an effect on the contact surface moving down the tube. In Figure 7.5 this effect can be seen. As the wall is at a large angle to the initial expansion wave, the reflected expansion accelerates the flow both away from the symmetry plane and towards the driver. The resulting velocity profile can be seen by the shape of the contact surface which moves down the tube at fluid velocity. The curving of the contact surface shows that a velocity gradient exists across the height of the tube due to the driver geometry. Other then this effect the flow features are much the same as the cylindrical case. The reflected expansion results in a low pressure and density region which in

turn needs a compression wave to form to ensure the pressure is corrected. The compressions strengthen to shock and create an enclosed "focus" region. The shocks move into the driver and the focus region collapses. The reflection patterns when the shock waves leave the cavity become quite complicated. It should be noted that in the final image of Figure 7.5 the shock waves at the corner of the test piece and the tube wall detach from reflected shock moving out of the tube and move into the cavity, repeating the flow pattern described previously, however with weaker gradients throughout.

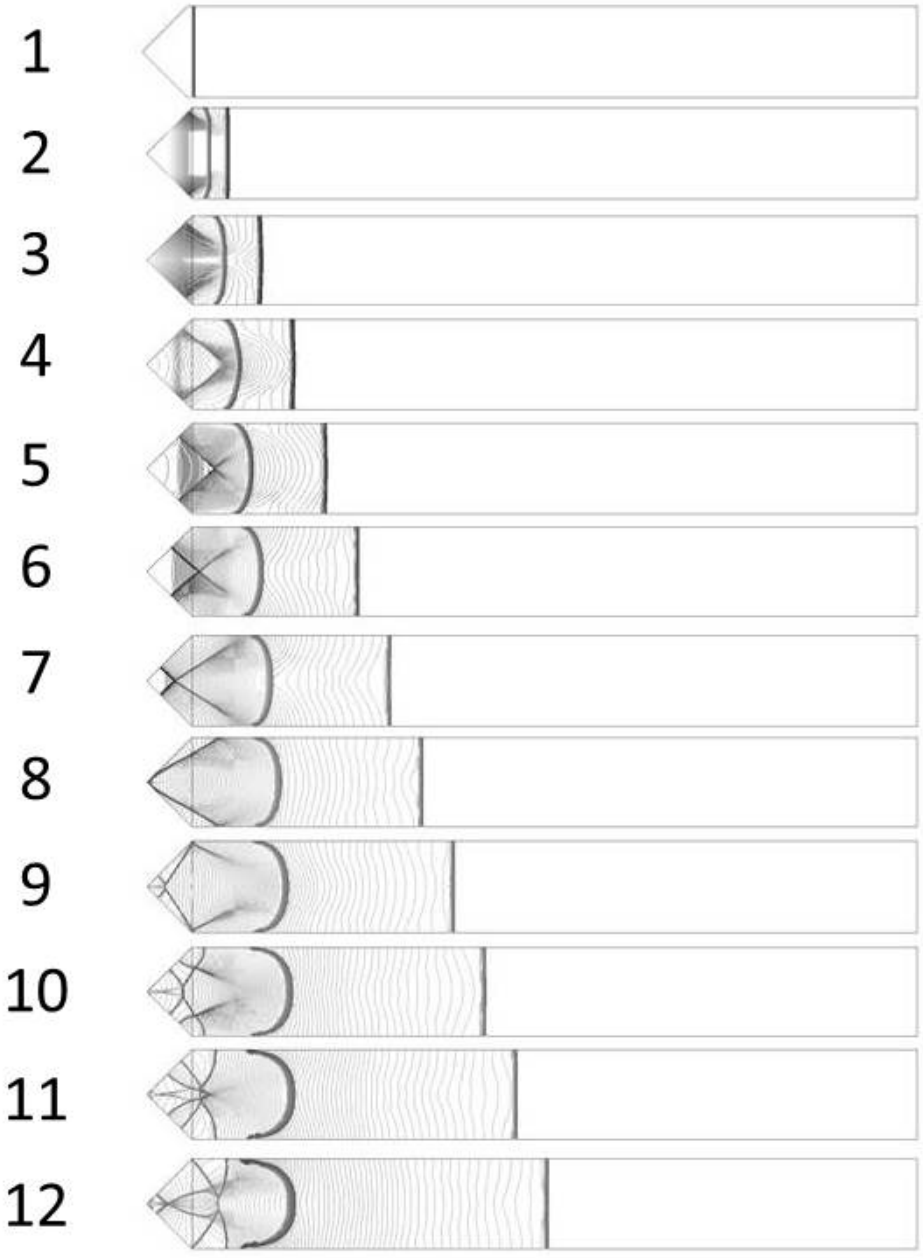


Figure 7.5: Time series for triangular test piece, P41 = 7, Contours of density

Figure 7.6 gives a more detailed look at the wave patterns which cause the flow seen in Figure 7.5. The initial expansion wave leading and trailing edge is shown by the dashed black lines. This wave moves into the driver and remains plane as with the cylindrical test piece. The reflected expansion wave from the test piece is shown by the dotted red lines. The leading edge of this expansion wave can be seen to move almost completely perpendicular to the tube direction. Again the region where two expansion waves are moving through the flow is hi-lighted by the grey cross-hatched region. It should be remembered that unlike shock wave flows where there is a discontinuous change in flow properties and thus separate regions of different flow properties appear, for expansion wave flows regions of changing flow properties are set up. In the case shown in image 2, 3 and 4 of Figure 7.6 the grey region represents a region where the flow properties change in two dimensions due to the two expansion waves. Thus the values are highest before the expansion wave has passed through the flow, and lowest when both expansion waves have fully passed through the flow (bottom left of the grey region to top right). In image 5, a region in which 3 expansion waves are moving through the flow is hi-lighted by the diagonally hatched region. In this region, both the initial expansion wave (black dashed line), the reflected expansion wave (red dotted line), and the expansion wave reflected from the symmetry plane (purple dot-dash line) are present. The additional expansion wave means that the direction in which the flow properties are changing is different to the region where there are two or 1 expansion waves. The movement of the reflected expansion wave means that when the full reflected (purple) expansion wave has moved through the region the lowest fluid properties will be found at the symmetry plane. Additional reflected expansions will cause the lowest properties to be found at the walls, then back at the symmetry plane, and so on until the trailing edge of the initial reflection (red dotted line) reaches the end of the cavity. At this point the symmetry plane and the wall meet causing the lowest fluid properties to be present before the compression waves behind the trailing edge reach the end of the cavity causing the focus region to disappear.

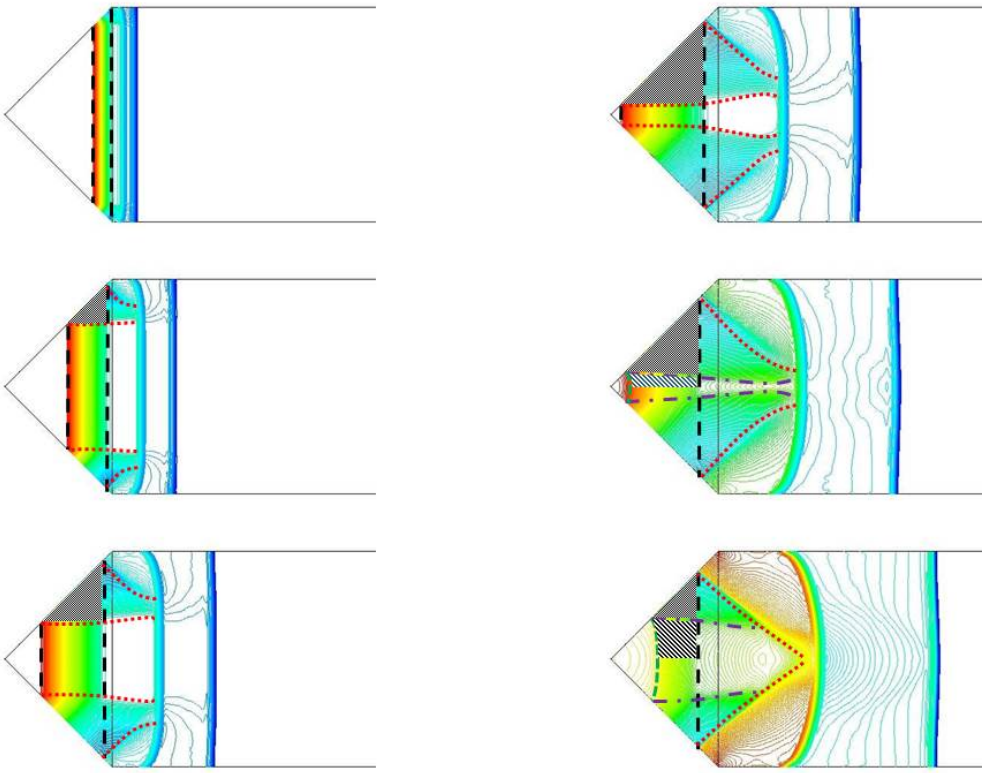


Figure 7.6: Detailed focusing phenomena for triangular test piece, Contours of Temperature

The third geometry used will be called a converging cavity. It consists of two quarter cylinders placed so that the cavity ends in a sharp point. The density contours for this geometry are given in Figure 7.7. The flow for this particular geometry varies from the previous two cases as the reflected expansion affects both the contact surface and the initial shock from the diaphragm burst. The flow in the driver itself is also different. The contact surface never leaves the driver section near the walls indicating that there is a stagnated area of flow in this region.

The shock is also curved due to the reflected expansion wave. Within the driver section the flow starts in a similar way to the previous geometries, the reflected expansion waves cause compression waves to form which strengthen into shock waves. These shock waves meet at the symmetry plane and then start to move into the driver. Due to the shape of the driver, the incident angle of the shocks with the symmetry plane increases as the shocks move into the driver. Thus, at a point, the reflection on the symmetry plane changes from regular to Mach reflection (image 6 in Figure 7.7). The Mach stem grows and before the shock reaches the end of the cavity a single normal shock wave has been formed (image 7). The fluid ahead of this shock reaches extremely low pressure, temperature and density. While the shock waves move into the driver, vortices form at the contact surface and the contact surface starts to roll up. This is most likely due to the flow on the test piece meeting the tube at 90^o and thus

a separation bubble forms at either side of the test piece. The contact surface starts to roll up in image 5 of Figure 7.7. When the shock waves leave the cavity a complicated reflection pattern is set up as can be seen in image 8-10.

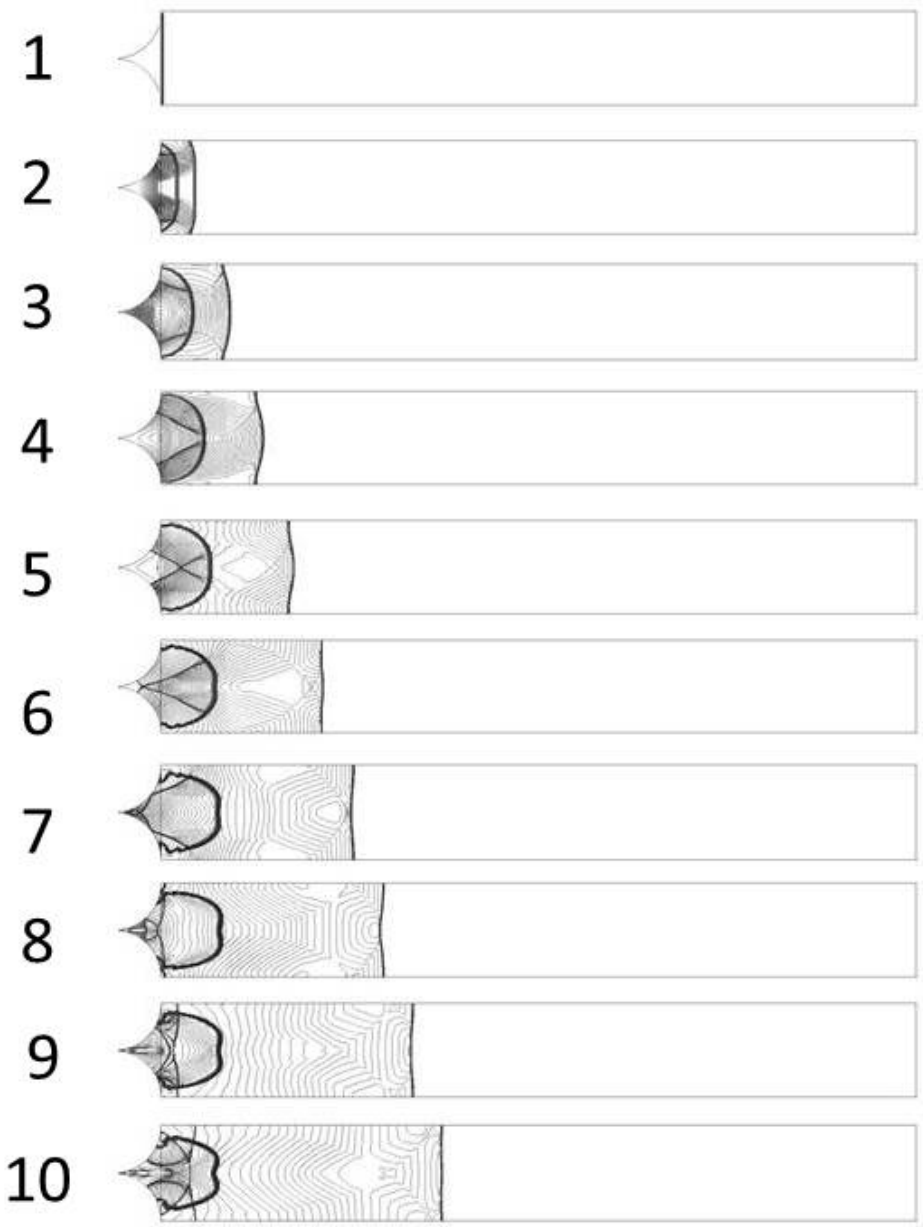


Figure 7.7: Time series for Converging test piece, P41 = 7, Contours of density

A more detailed look at the wave patterns for the converging test piece is given in Figure 7.8. As with the previous two geometries the reflected expansion waves create regions in which the flow properties change by a large amount. When the trailing edge of the initial reflection meets at the symmetry plane the focus region is formed and the compression waves also meet. The reflection of the expansion waves in this region creates areas of low pressure in the same

way as described for the triangular test piece. Unlike the triangular and cylindrical test piece the reflected expansion waves can clearly be seen to move through the contact surface and affect the shape of the shock wave.

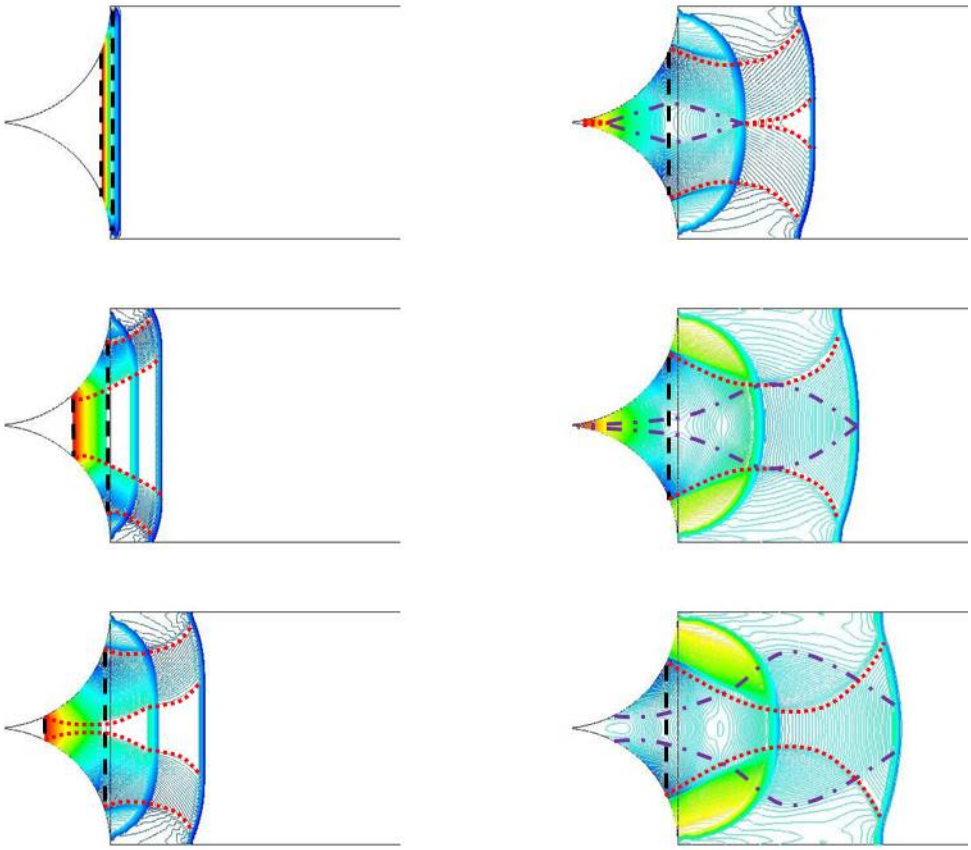


Figure 7.8: Detailed focusing phenomena for converging test piece, Contours of Temperature

The final two geometries were both parabolas. For the parabola with an aperture to depth ratio of 0.5, Figure 7.9, the flow features are very similar to the cylindrical case, except for the contact surface which is slightly affected by the driver geometry.

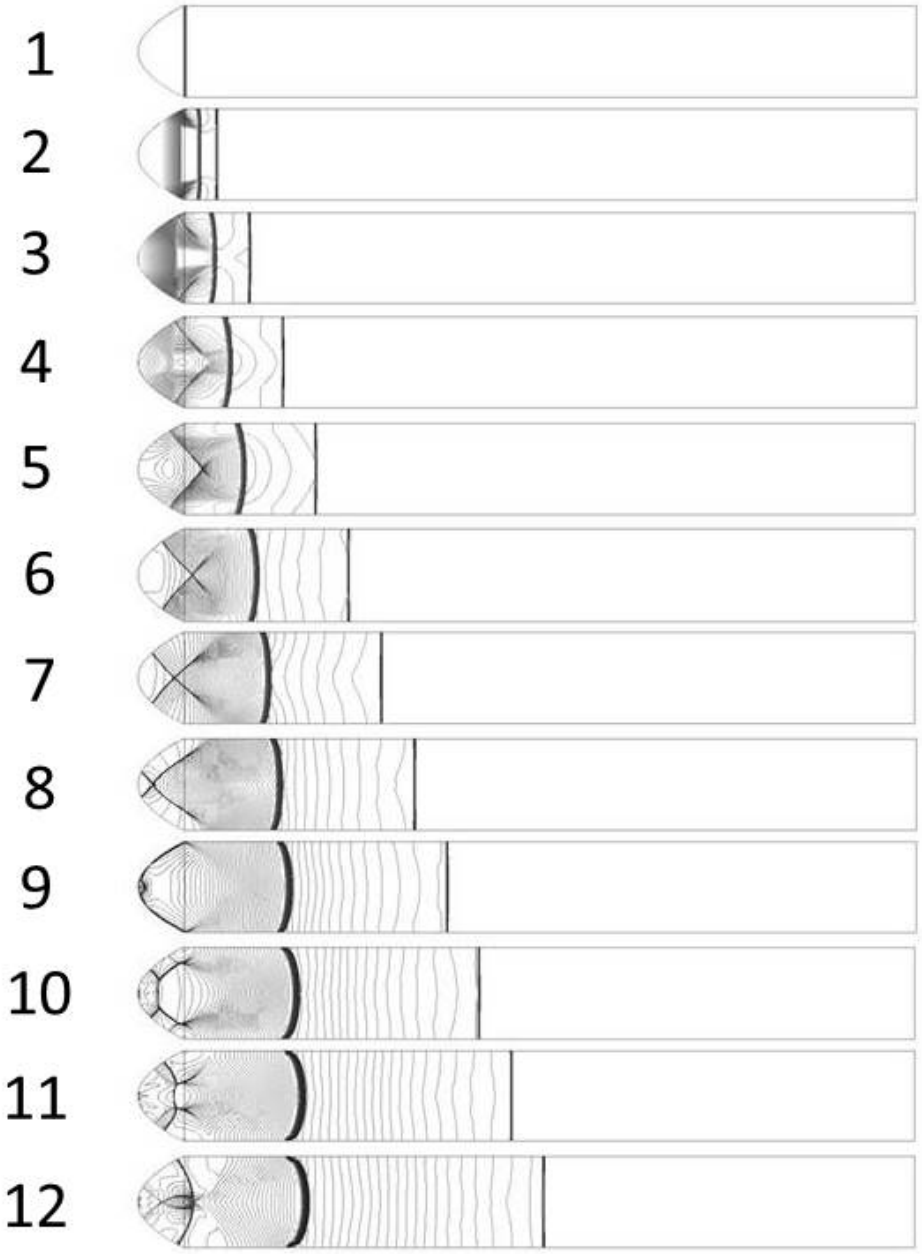


Figure 7.9: Time series for Parabolic test piece AD 0.5, P41 = 7, Contours of density

The wave patterns for the AD = 0.5 parabola are shown in more detail in Figure 7.10. The wave pattern is very similar to the cylinder, except that the wave shapes are more parabolic than cylindrical.

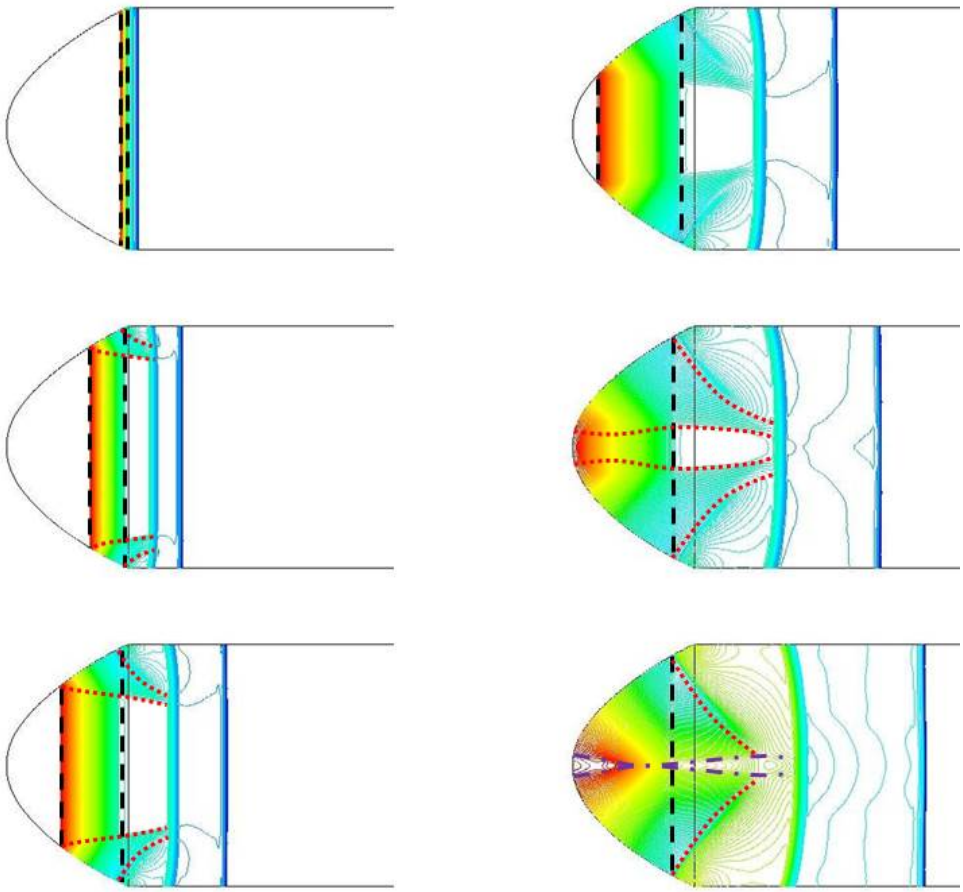


Figure 7.10: Detailed focusing phenomena for Parabolic test piece AD = 0.5, Contours of Temperature

For the parabola with an aperture to depth ratio of 1 the features are slightly different. The extra length of the driver allows the shock waves which form after the expansion wave reflects to more fully develop and more complex expansion wave reflection patterns occur before the shock waves reach the end of the driver. The shock waves reflect regularly when they first meet on the symmetry plane. However, as they move in the driver, the reflection changes to Mach reflection and the Mach stem grows from the symmetry plane outwards. At a point the Mach stem grows to be the full height of the cavity and thus the wave becomes a single normal shock wave. The shock remains attached at the walls thus remains regular reflection at the walls. As a result this shock doesn't exhibit the same shock focusing pattern as is normally seen for shock wave cavity flows. Apart from this the flow features are similar to the 0.5 AD ratio parabola.

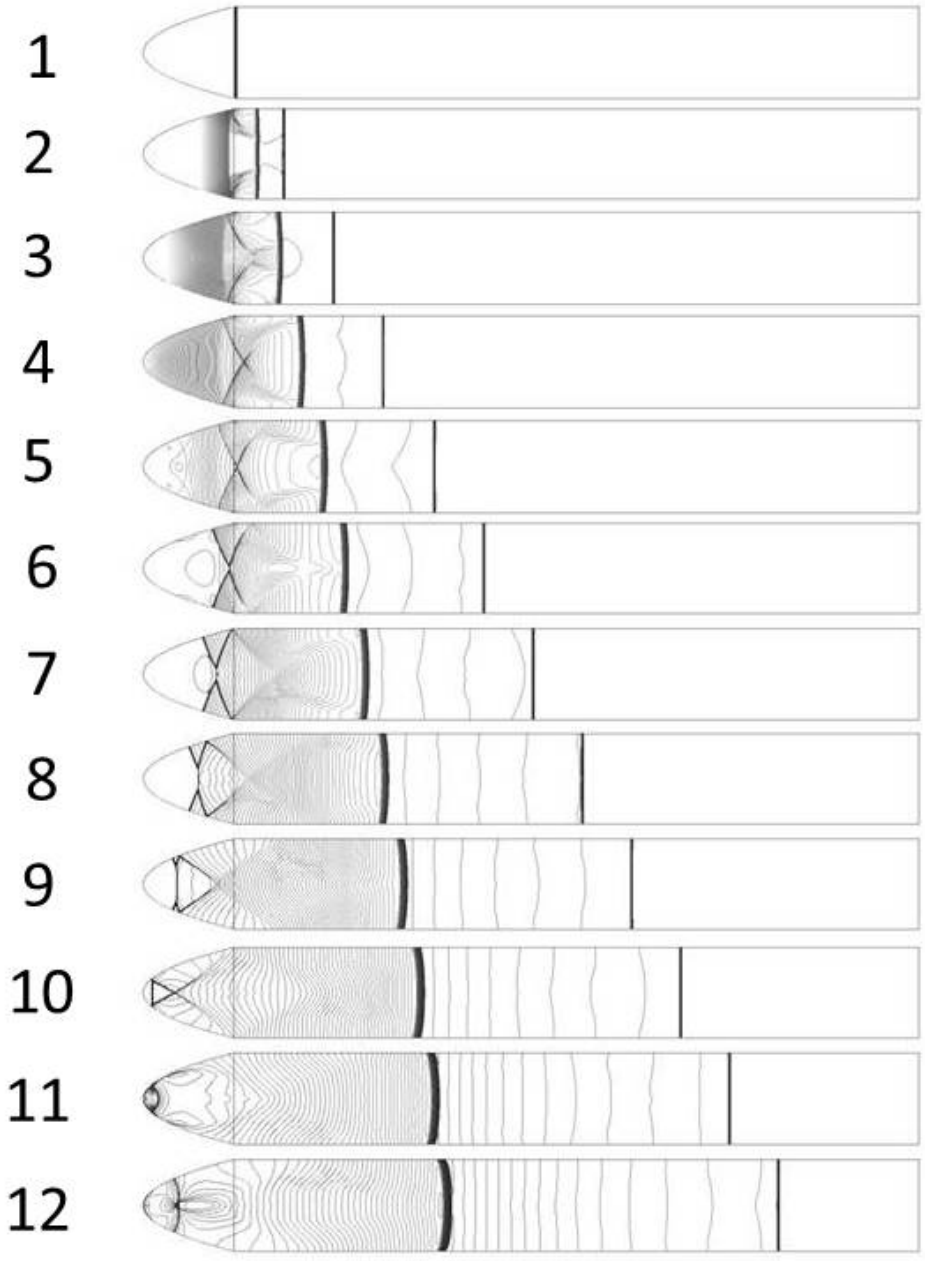


Figure 7.11: Time series for Parabolic test piece AD 1, P41 = 7, Contours of density

The wave patterns for the AD =1 parabola are shown in Figure 7.12 and Figure 7.13. As the cavity is deeper more reflected expansion waves can form before the trailing edge of the first reflected expansion, dotted red line, reaches the end of the cavity. Figure 7.12 shows the formation of the focus region and is similar to the patterns seen for the previous geometries.

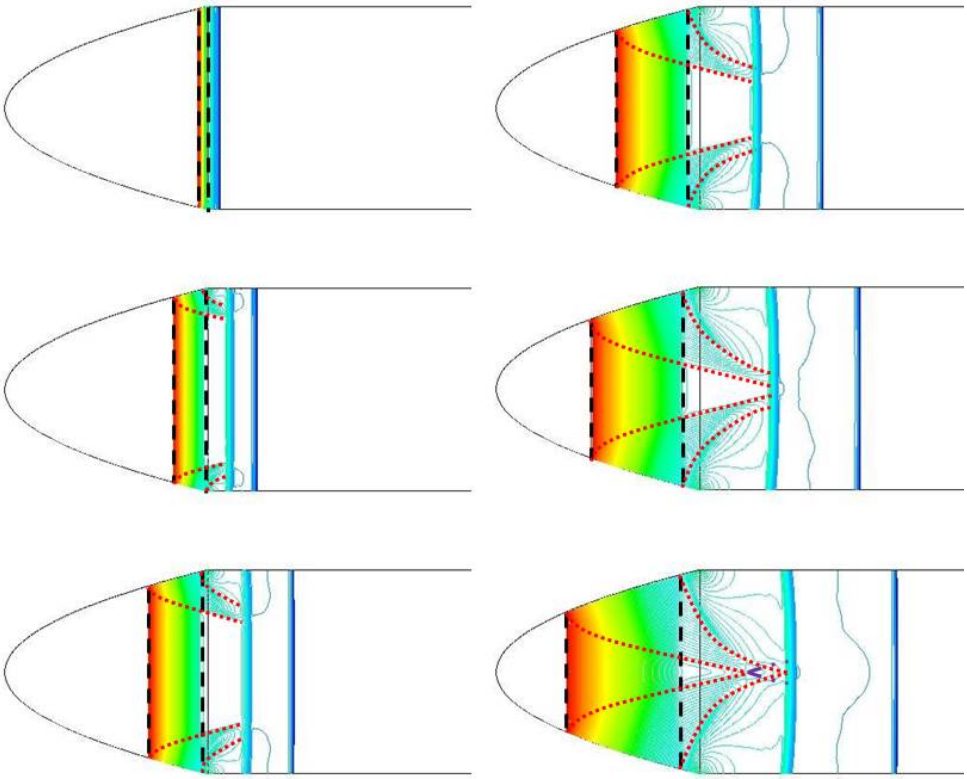


Figure 7.12: Detailed focusing phenomena for Parabolic test piece AD = 1, early, Contours of Temperature

The deeper cavity allows some of the later reflected expansion waves to be hi-lighted. In Figure 7.13 these additional reflected waves can be seen from image 4. Only the leading edge of the expansion wave is shown as the trailing edge will only become apparent once the entire expansion wave has been reflected. The dashed green line is the reflected leading edge of the original expansion wave, note that this reflected wave is curved, unlike the plane wave which entered the cavity. The blue dotted line is the reflection of the initial reflected expansion wave leading edge, red dotted line, off the end of the cavity. The dark blue dash-dot line in the 6th image is the reflection of the purple expansion wave leading edge off the wall of the cavity. The motion of these expansion waves helps to explain the very low fluid property values which are found at the end of the cavity as multiple expansion waves have been reflected out of the cavity, causing an exaggerated drop in pressure and temperature.

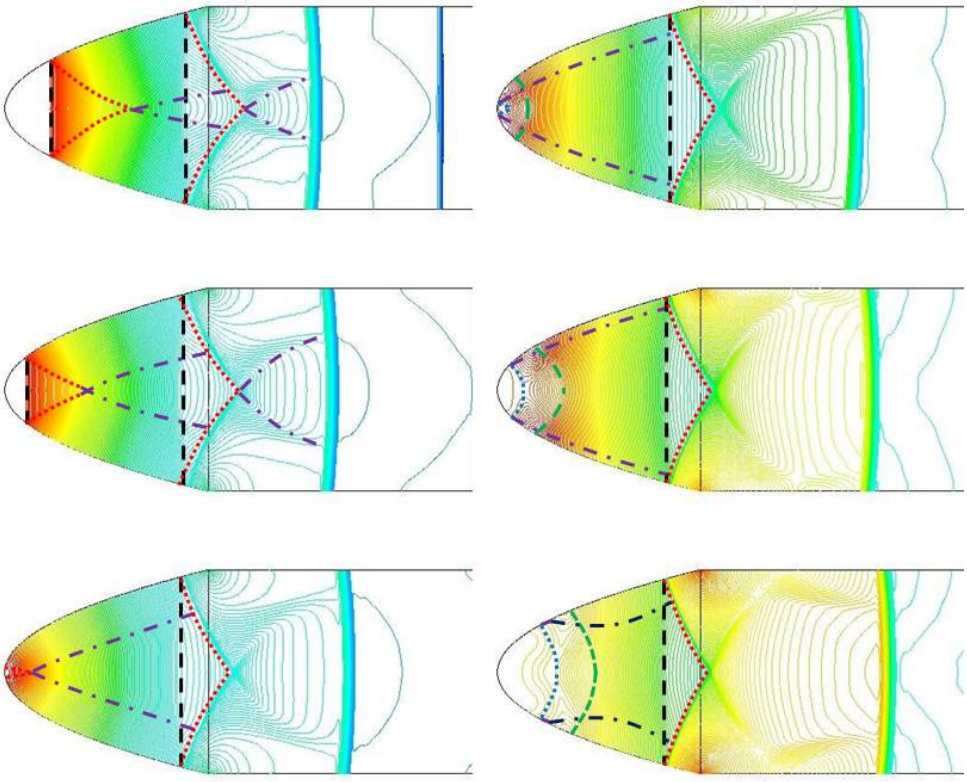


Figure 7.13: Detailed focusing phenomena for Parabolic test piece AD = 1, late, Contours of Temperature

The lowest pressure and temperature which occurs in the tube for the different geometries is given in Table 7.14. These values do not occur at the same time for the different geometries due to the difference in the flow, but they show for which geometry the focusing is the strongest, indicated by the lowest pressure and temperature as this implies the fluid has been expanded the most.

Figure 7.14: Minimum pressure and temperature for different geometries

Geometry	**Minimum pressure [kPa]**	**Minimum temperature [K]**
No test piece	72.7	157
Cylinder	33.2	125
Triangular	6.8	80
Converging	1.4	50
Parabola AD 0.5	14.7	99
Parabola AD 1	16.9	103

Figure 7.15 gives the Wave position along centre line against time plots for the various geometries used. These plots show the time and position for the values given in Table 7.14.

These diagrams also provide additional understanding about the formation and strength of the focusing region for the different geometries. The converging test piece has the most different wave diagram, in particular the very high temperature which occurs when the shock wave collapses into the cavity. The cylindrical, triangular and parabolic cavities all have similar wave diagrams.

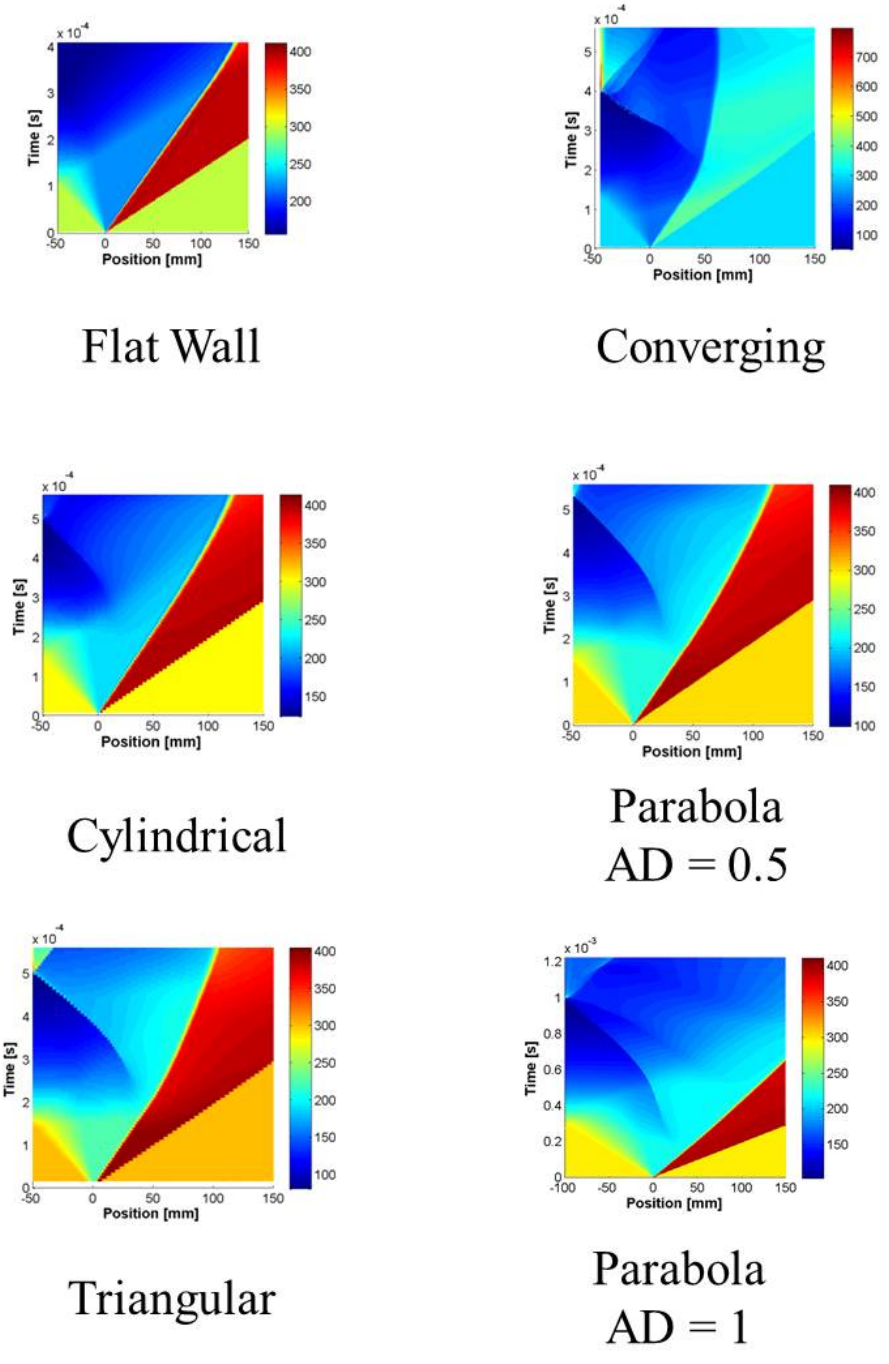


Figure 7.15: Wave position along centre line vs time plots for different geometries, coloured by temperature

Figure 7.16 gives the contour plot with a graph of the temperature along the symmetry line. Normally this image would be part of an animation which shows the full period of flow with the temperature plot. This helps to see how the focus region is formed and helps to identify the features seen. The animation for this simulation as well as the other simulations can be found in the digital appendix.

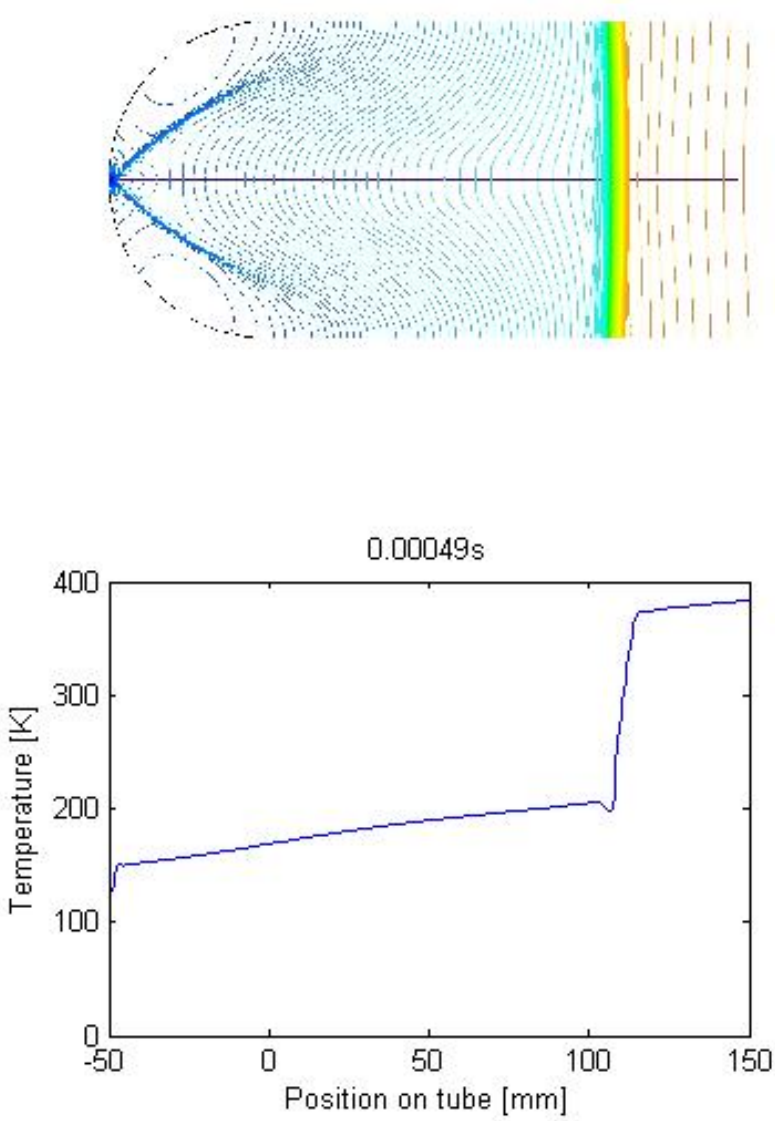


Figure 7.16: Contour plot with temperature along symmetry line for cylindrical test piece and diaphragm pressure ratio of 7

The basic flow pattern for all geometries can be summarised as:

1. The expansion wave enters the cavity and the deflection of the walls causes a reflected expansion wave.

2. The reflected expansion wave creates a region through which the fluid is expanded more than the rest of the fluid.

3. Compression waves form behind the trailing edge of the reflected expansion wave to correct the fluid properties.

4. When the trailing edges of the reflected expansion waves meet on the symmetry plane, with the corresponding compression waves behind them an enclosed flow region is formed which has been called the focus region.

5. The reflected expansion waves within this region continue to reflect, creating regions of flow in which the fluid is being expanded by 3 or even more expansion waves. This causes the fluid properties to drop to very low values.

6. As the trailing edge of the main reflected expansion wave, and the compression waves immediately behind it, move into the cavity the fluid in the focus region is expanded through the multiple expansion waves in a progressively smaller region.

7. When the compression waves reach the end of the cavity the focus region disappears and the lowest fluid properties are found just before this occurs.

7.2 Curved Diaphragm simulations

As experimentally a perfectly plane diaphragm at burst could not be achieved, simulations were run with an initially curved diaphragm in order to see the effect this would have on the flow. The major concern with a curved diaphragm is the initial expansion wave will also be curved and thus there will be two dimensional waves in the flow which are unrelated to the driver geometry used. The initial shock wave which moves down the tube is also curved. Thus it impacts the upper and lower walls of the tube, which means there are two dimensional shock waves immediately at the diaphragm position which are also unrelated to the driver geometry. Figure 7.17 gives density contours for a cylindrical test piece where the diaphragm is highly curved as was seen for plastic diaphragms experimentally. The diaphragm curvature is such that it makes a hemisphere in the tube. The initial curvature causes the shock wave to immediately reflect off the top and bottom of the tube, image 2, while the expansion immediately collapses towards the centre of the tube. This creates a region similar to the focus region seen in the ideal case, where a low pressure and temperature area is trapped between shock waves, which gets smaller as the shock waves converge. Unlike the flow for the plane diaphragm case, this occurs independently of the geometry. The expansion is also

not fully enclosed as the expansion is still free to move into the driver section. The expansion which does move into the driver is weaker and doesn't reflect off the driver geometry at as large an angle as the plane diaphragm case. As a result no shocks are formed in the driver however the initial shock waves from the diaphragm burst are drawn into the driver at a later time.

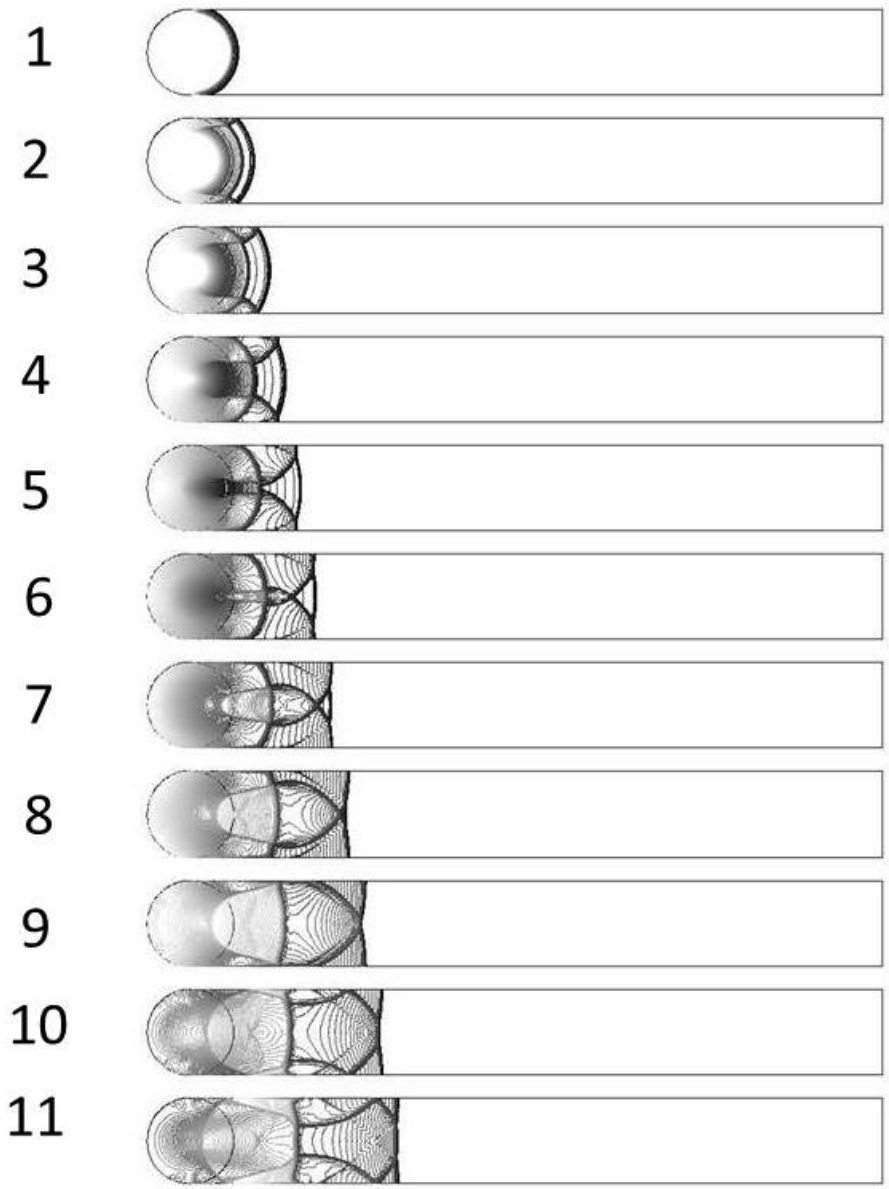


Figure 7.17: Time series for cylindrical test piece with an initially curved diaphragm, P41 = 5, Contours of density

The flow for the other driver geometries, such as the triangular cavity shown in Figure 7.18 is similar, showing that the flow is primarily as a result of the diaphragm curvature rather than the driver geometry. In this simulation, the diaphragm is slightly less curved, with the maximum deflection being 0.4 times the tube height rather than 0.5 times as was shown in

the case for the cylindrical simulation. For the triangular test-piece weak shock waves do start to form in the driver as in the plane diaphragm case, image 7. However the shocks from the curved diaphragm are drawn into the drive before these waves can fully develop to form a flow pattern as in the plane diaphragm case, images 8-10.

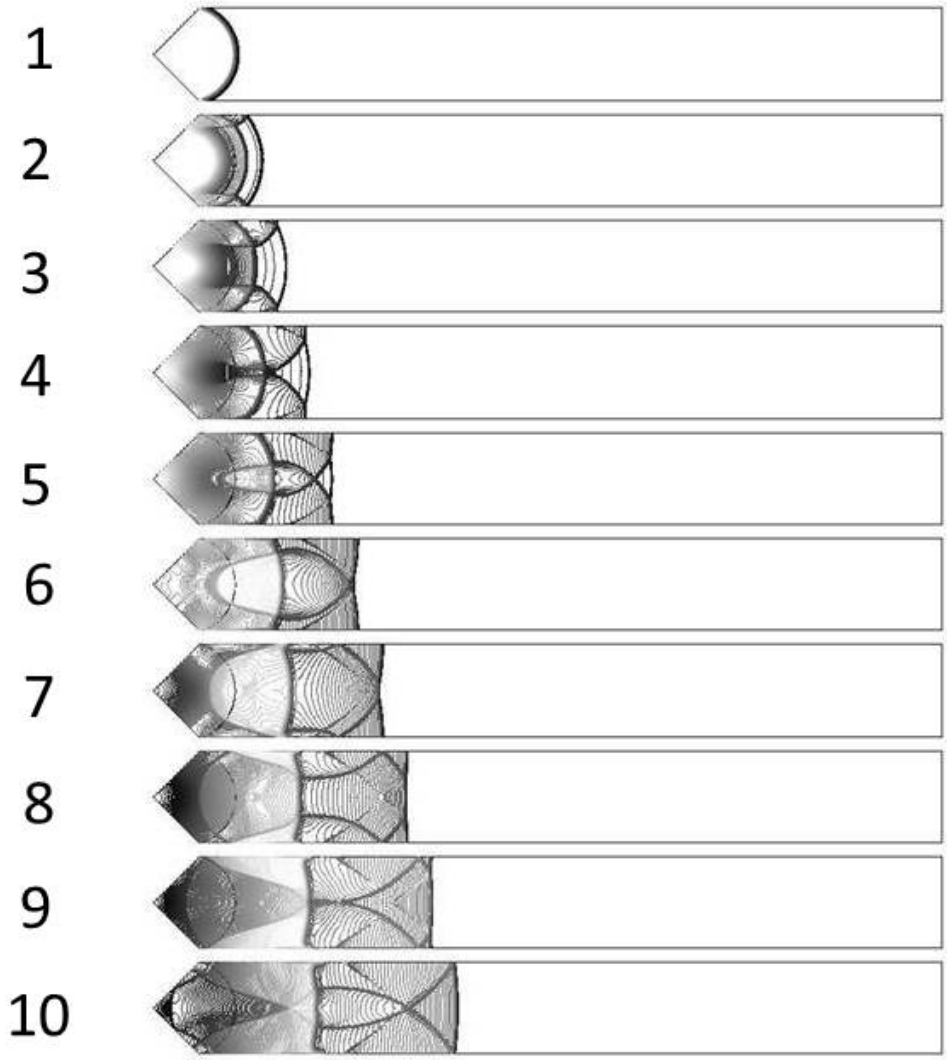


Figure 7.18: Time series for triangular test piece with an initially curved diaphragm, P41 = 7, Contours of density

Wave diagrams for these curved diaphragm simulations are shown in Figure 7.19. The initial flow, before 0.00025s, is almost identical for the two cases as this is due to the diaphragm curvature rather than the test piece geometry. At later times the flow starts to differ and some similarities to the plane diaphragm case can be seen, however the actual flow continues to be different. The initial focus due to the curved diaphragm is very short and also very small, which can be seen be the small region of dark blue which occurs at around 0.00024s.

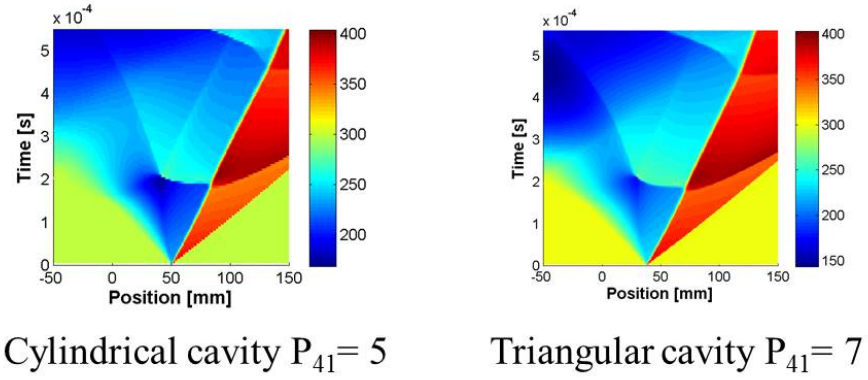


Figure 7.19: Wave position along centre line vs time plots for different geometries with an initially curved diaphragm, coloured by temperature

7.3 Results for Different Diaphragm Pressure Ratios

The time series in Figure 7.20 show the flow for the cylindrical test piece at 4 different diaphragm pressure ratios. All of these pressure ratios are below 10 and thus, as shown by Figure 2.10, the fluid velocity downstream of the expansion wave is subsonic. This means that for all these cases the trailing edge of the expansion wave moves into the driver. For the diaphragm pressure ratios of 3, 5 and 7 the flow features are similar, with the strength of the waves increasing with increasing pressure ratio. At the diaphragm pressure ratio of 9 the flow starts to differ. This is due to the flow velocity downstream of the expansion wave being very close to sonic and thus the trailing edge of the expansion wave barely moves into the driver before the two dimensional expansion waves meet at the symmetry line.

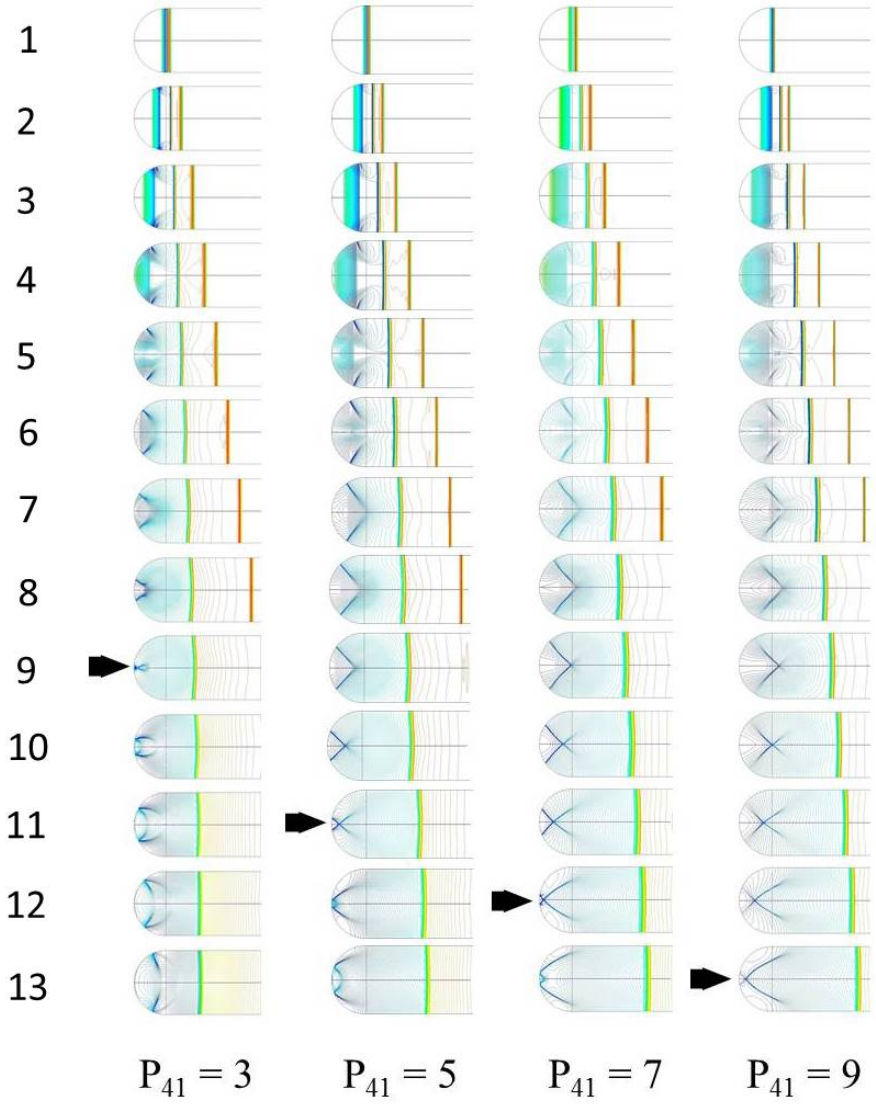


Figure 7.20: Comparison of flow for different diaphragm pressure ratios below 10 (arrow indicates when lowest flow values occur, Contours of temperature, 0.000042s between frames

The minimum pressure and temperature as well as the flow time at which they occur are plotted in Figure 7.21 for the pressure ratios below 10 which were tested. The general trends are for a higher diaphragm pressure ratio the minimum values occur later and are lower. The diaphragm pressure ratio of 9 result is slightly different, as was noted with the time series.

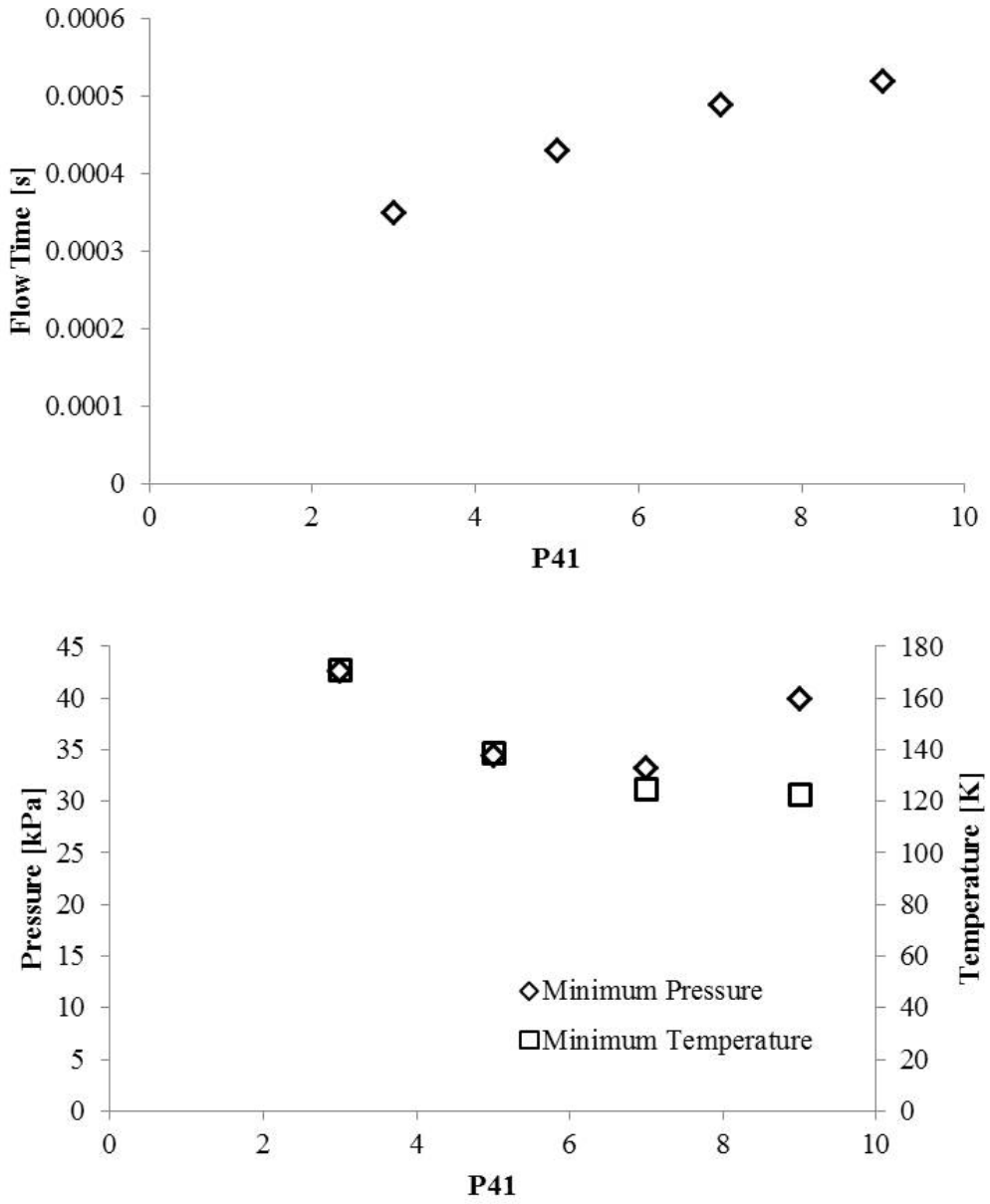


Figure 7.21: Plot of minimum temperature and pressure with diaphragm pressure, P41 ¡10, Cylindrical test piece

For diaphragm pressure ratios above 10 the flow is quite different as can be seen in Figure 7.22 and Figure 7.23. This is due to the flow velocity being supersonic and the trailing edge of the expansion wave thus travelling downstream instead of into the driver. The diaphragm pressure ratio of 9 results are included again as even for this pressure ratio some of the flow features seen with the higher pressure ratios begin to appear. Figure 7.22 shows the early flow features which occur for these pressure ratios. The main feature to note is that for the high pressure ratios shocks don't form at the walls and move into the driver section. Instead shocks form at the driver position and move transverse to the tube rather than along the

tube. Only once the shocks have met at the symmetry plane and reflected do they start to move towards the driver, image 10 for a pressure ratio of 12 and image 9 for a pressure ratio of 15.

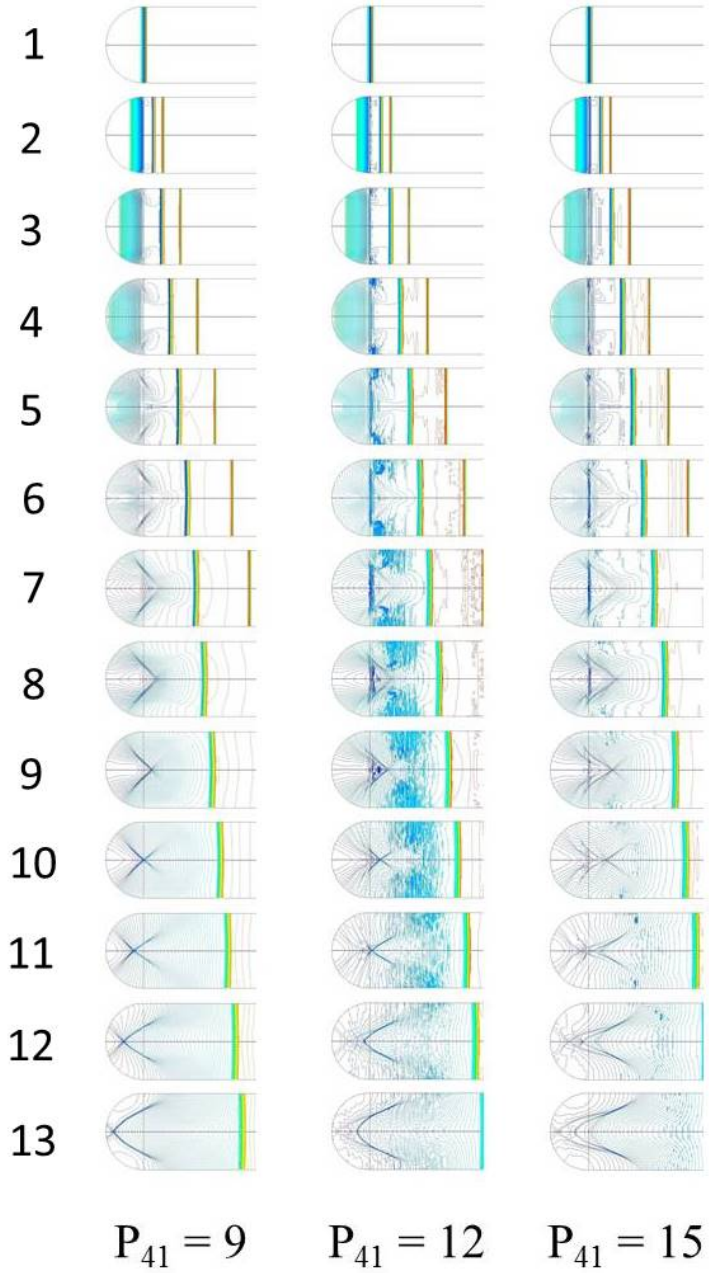


Figure 7.22: Comparison of flow for different diaphragm pressure ratios above 10, Contours of temperature, early flow features

Later a focusing region similar to that seen for a curved diaphragm develops, this also occurs for the diaphragm pressure ratio of 9. This later focusing is shown in Figure 7.23. The end of focusing at which the lowest flow property values occur is indicated with an arrow.

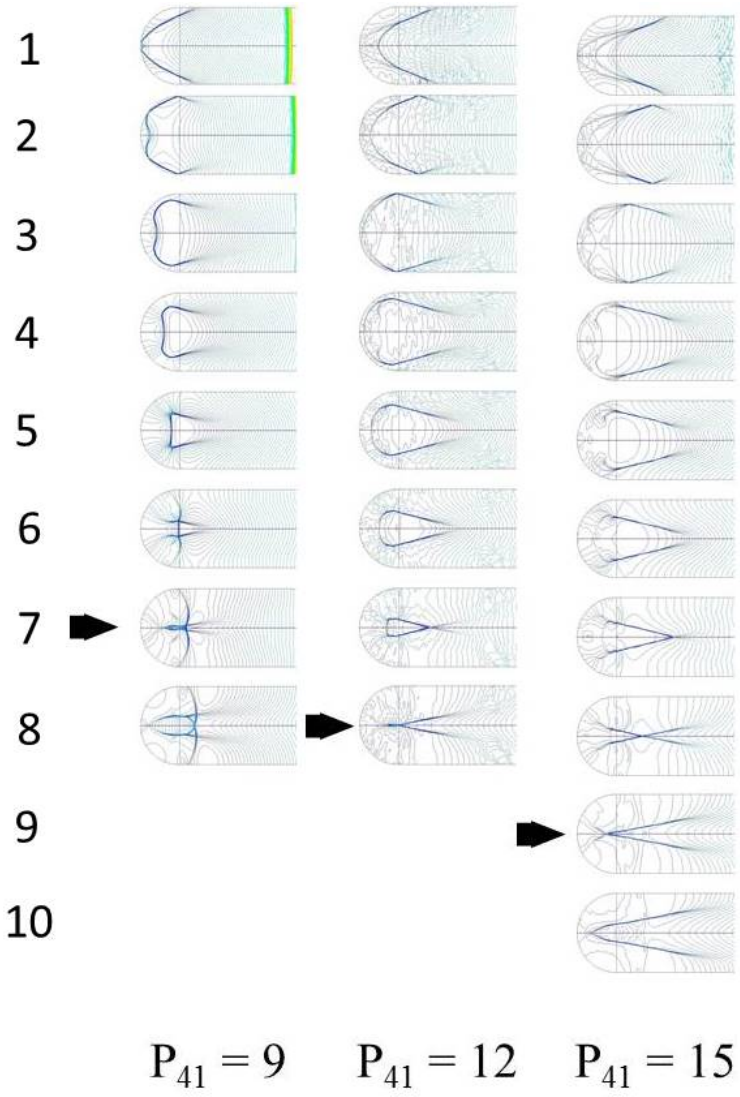


Figure 7.23: Comparison of flow for different diaphragm pressure ratios above 10, Contours of temperature, late flow features

The minimum pressure and temperature for these pressure ratios is plotted in Figure 7.24. These occur at the later time. The values plotted for the P41 = 9 case are for a second focus which happens later than that shown in Figure 7.21 as indicated in Figure 7.23.

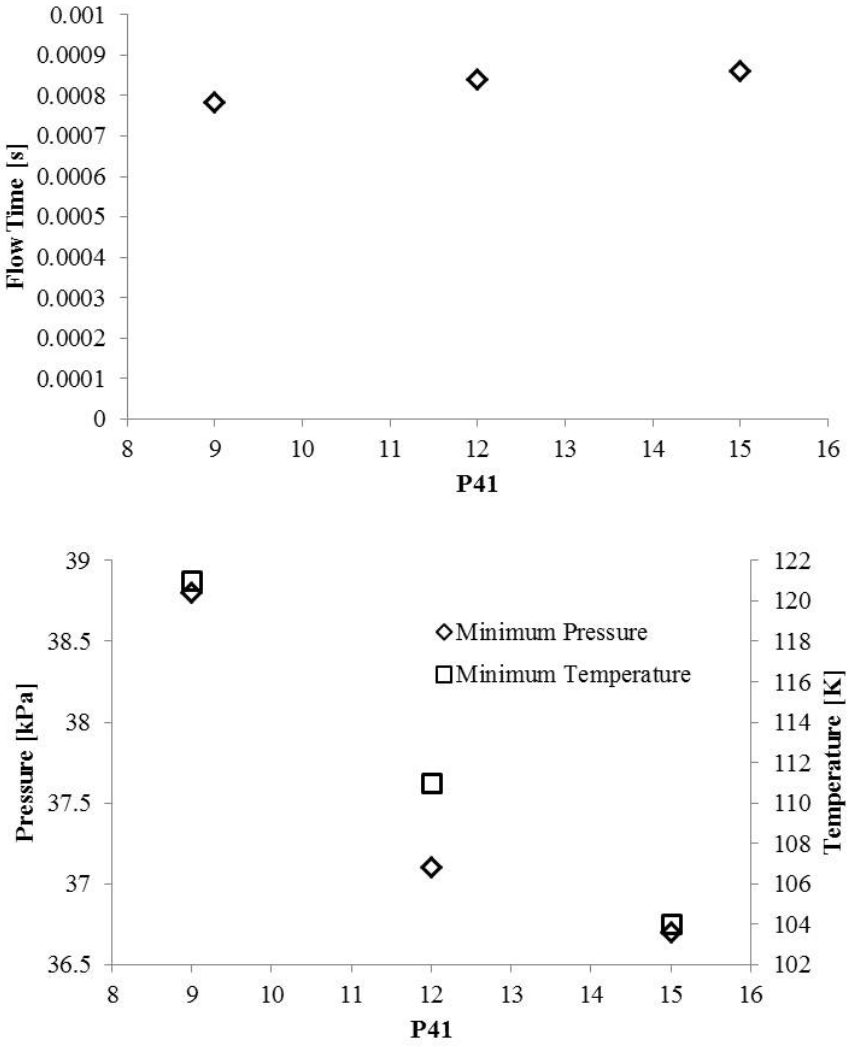


Figure 7.24: Plot of minimum temperature and pressure with diaphragm pressure, P41 ¿ 10, Cylindrical test piece

The flow for different pressure ratios for the triangular test piece is shown in Figure 7.25. As with the cylindrical test piece for diaphragm pressure ratios below 10 the flow pattern is similar. However, the features become stronger as the pressure ratio increases, the focusing region also takes longer to form and the lowest values occur later. Unlike the cylindrical test piece the same flow pattern is present for diaphragm pressure ratios above 10, as shown by the time series on the right for a diaphragm pressure ratio of 12. The focus region formed initially extends well into the driven section as the trailing edge of the expansion wave is moving down into the driven section. The reason for the flow pattern persisting is likely due to the angle at which the expansion wave reflects off in the driver being large immediately at the diaphragm unlike the cylindrical test piece where the angle increases gradually. This stronger reflection can be seen in the first 3 images for the P41=12 time series. The fourth column in Figure 7.25 shows a second focus region that forms for the P41 = 12 case, similar

to the flows which are seen for P41= 12 and 15 with the cylindrical test piece. The pressure and temperature in this second region don't drop as low as they do in the first focus region however.

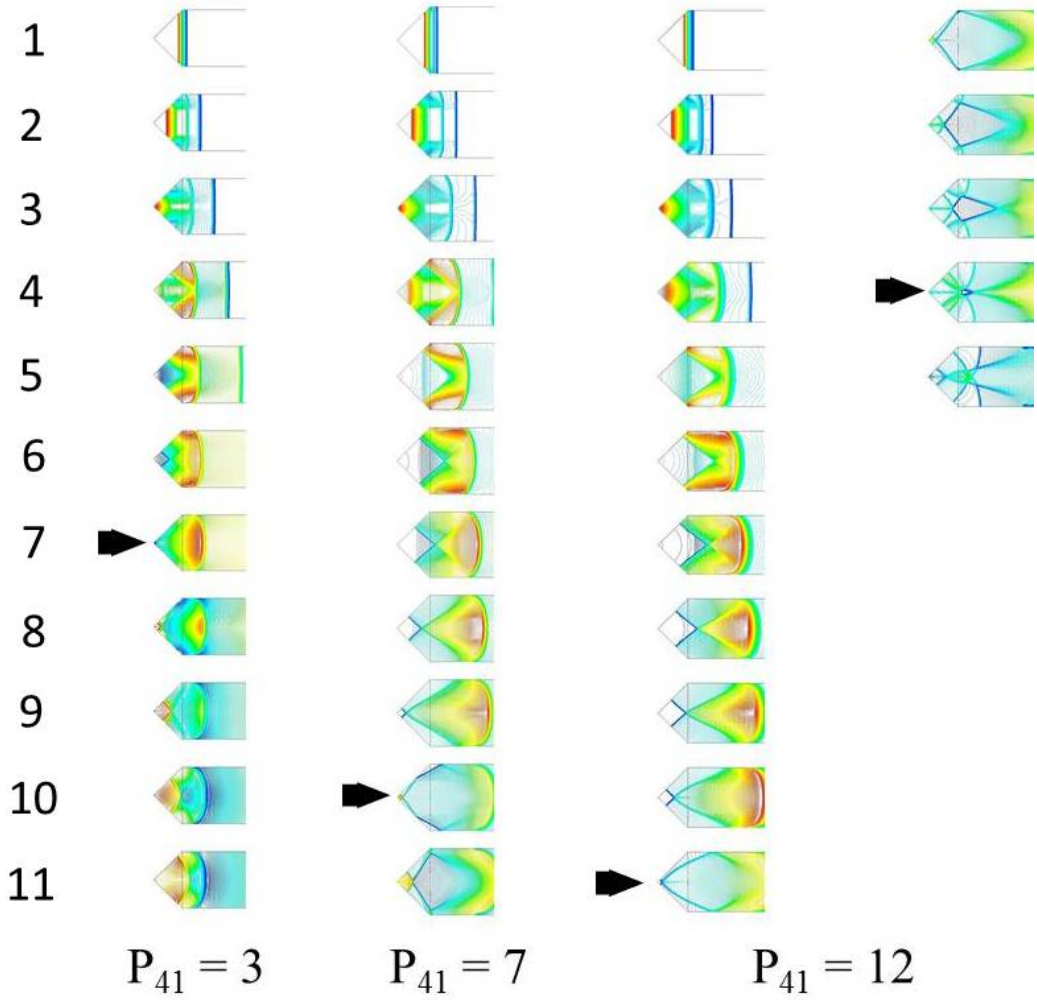


Figure 7.25: Comparison of flow for different diaphragm pressure ratios, triangular test piece, Contours of density, time between images = 0.000056s

A plot of the minimum pressure and temperature reached for the different diaphragm pressure ratios is given in Figure 7.26. As with the cylindrical case the minimum temperature drops as the pressure ratio increases, note that the minimum temperature is significantly lower than that for the cylindrical test piece showing that the focusing is stronger for this geometry. The minimum pressure exhibits the same behaviour as cylindrical geometry with the minimum pressure reached at P41 = 12 being slightly higher than for P41 =7. It does however need to be remembered that the magnitude of the pressure drop for is still significantly higher for the P41 = 12 case, $\approx$ 1200 kPa compared with $\approx$ 700 kPa for the P41 = 7 case.

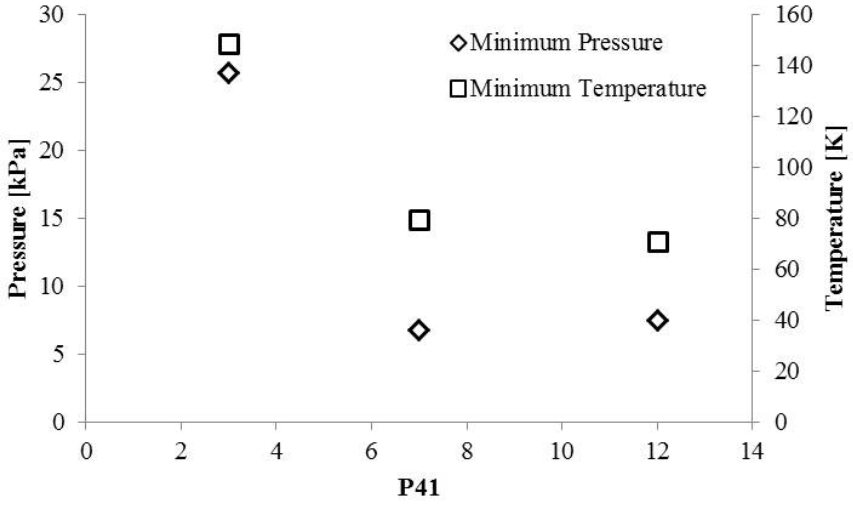


Figure 7.26: Plot of minimum temperature and pressure with diaphragm pressure for triangular test piece

Different diaphragm pressure ratios have a similar affect when the converging test piece is considered. The flow is shown in Figure 7.27. As with the triangular test piece the basic flow pattern remains even when the diaphragm pressure ratio exceeds 10. This is due to the expansion meeting the wall at a large angle immediately at the diaphragm. One feature which is clear for different pressure ratios is that the contact surface moves further down the tube before the flow velocity is decreased to zero. However, the edge of the contact surface at the walls never moves down the tube even with higher pressure ratios. As with the previous time series the point at which the lowest temperature and pressure is reached is indicated. As with the other geometries, this occurs later as the pressure ratio increases. For the diaphragm pressure of 12 case, a second low pressure region is seen later, as with the triangular test piece this is indicated in the fourth column of Figure 7.27.

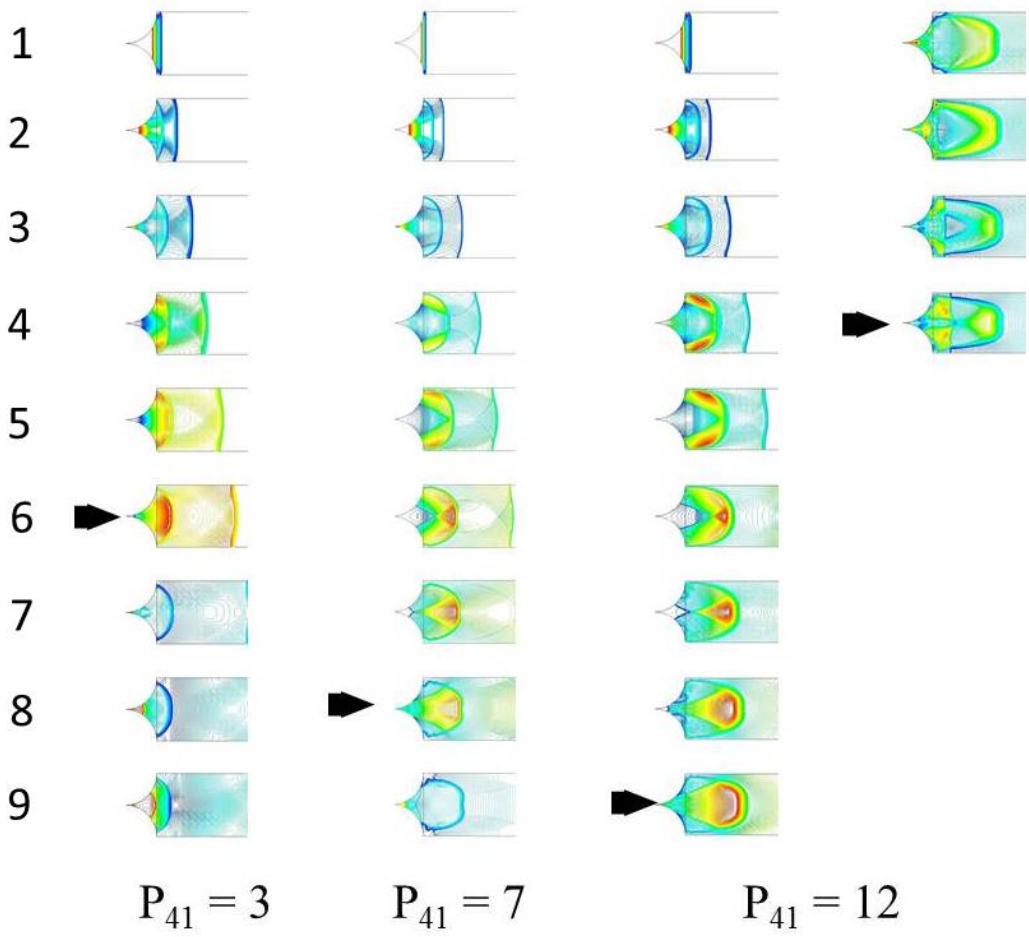


Figure 7.27: Comparison of flow for different diaphragm pressure ratios, converging test piece, contours of density, time between images = 0.000056s

A plot of the minimum pressure and temperature reached for the different diaphragm pressure ratios is given in Figure 7.28. The same trends are seen for the triangular and cylindrical cavities however the pressure is significantly lower. The values given are all for the end of the first focus region.

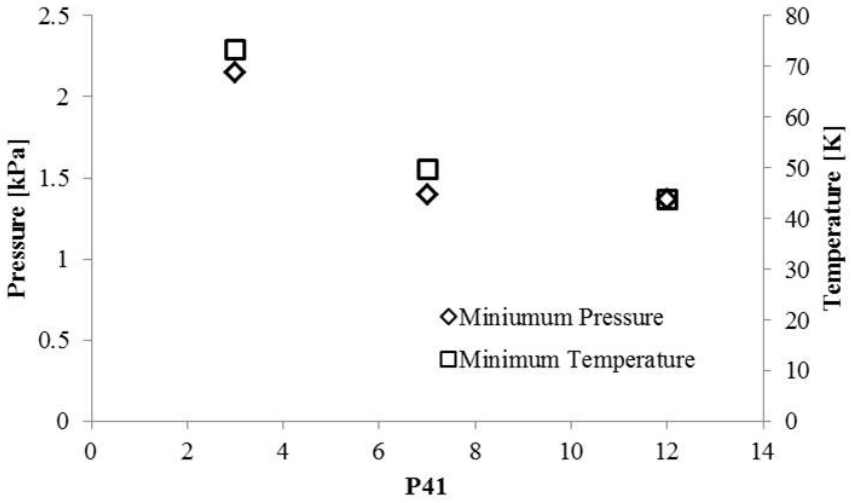


Figure 7.28: Plot of minimum temperature and pressure with diaphragm pressure for converging test piece

7.4 Results for Different Test-piece Distances from the Diaphragm

The distance of the test piece from the diaphragm is important as the expansion wave flattens out as it travels away from the diaphragm. Figure 7.29 and Figure 7.30 give contour plots for the test piece placed 60mm and 500mm away from the diaphragm.

It is quite obvious that moving the test piece away from the diaphragm has a large effect on the focusing phenomenon. At 60mm away from the diaphragm, the focusing already doesn't drop the flow properties sufficiently to cause strong compression waves to form and the transverse waves are weak in relation to the main expansion wave.

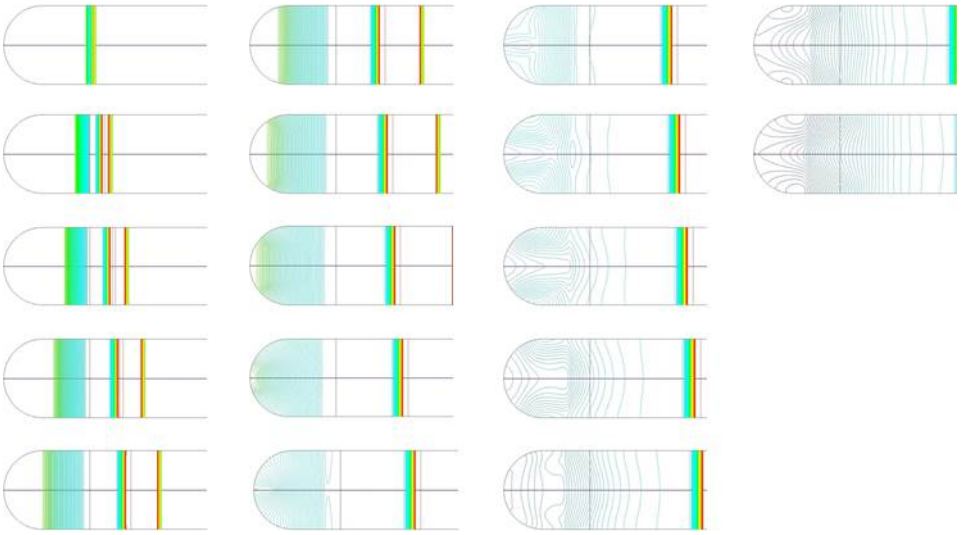


Figure 7.29: Time series for cylindrical test piece placed 60mm from the diaphragm, P41 = 7, Contours of temperature

When the test piece is moved further away from diaphragm the focusing becomes even weaker and the leading edge of the reflected expansion has become plane before it crosses the trailing edge of the initial expansion wave. This results in flow very similar to having a plane walled driver for most of the length of the tube.

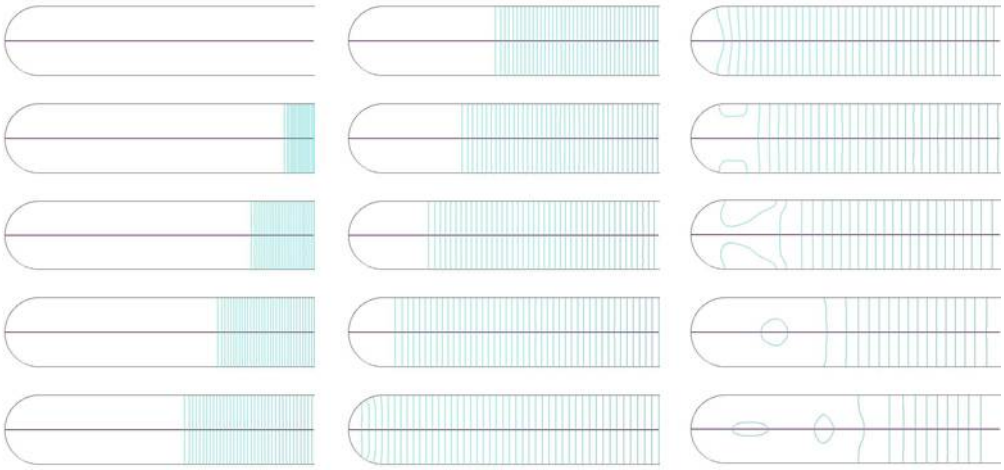


Figure 7.30: Time series for cylindrical test piece placed 500mm from the diaphragm, P41 = 7, Contours of temperature

Figure 7.31 gives the time distance plots for different test piece diaphragm distances. The focusing is clearly weaker as the distance is increased. This can be seen from the lack of a clear focus region for either the 60mm or 500mm case, as well has the higher minimum temperatures for these cases. For neither of the cases where the test piece was moved away from the diaphragm were strong compression waves or shock waves formed in the driver.

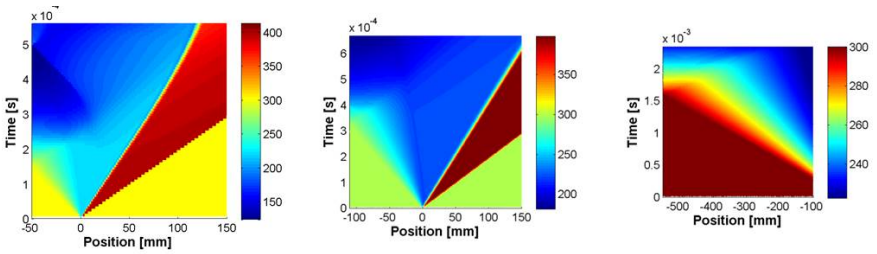


Figure 7.31: Wave position along centre line vs time plots for cylindrical test piece at different distances from the diaphragm, coloured by temperature

7.5 Experimental/Numerical Validation

This section will compare the results from the experimental tests with those obtained from the numerical simulations in order to determine the validity of the numerical simulations. This will be done qualitatively as the images obtained experimentally are unable to give quantitative data. Figure 7.32, Figure 7.34 and Figure 7.36 give images for the experimental tests for the cylindrical, triangular and converging cavities. The images were recorded at 50000 frames per second and have been post processed in order to allow the flow features to be more clearly seen. The features seen differ in shape from the numerical results and this is likely due to the diaphragm burst not being instantaneous and thus the initial expansion wave is not the same as the ideal case modelled by the numerical simulations. The diaphragm bursts from the centre and thus the initial expansion will be curved, even if the diaphragm doesn't have much curvature at burst.

The cylindrical test piece has the weakest reflected expansion waves and as a result the expansion wave itself isn't seen in the experimental images, however the compression waves which form in the driver can be seen. Figure 7.32 gives a series of images from an experimental test with the cylindrical test piece in place and a diaphragm pressure ratio of 3. The features seen were compared with numerical results in order to try and determine what they were and to check the validity of the numerical results.

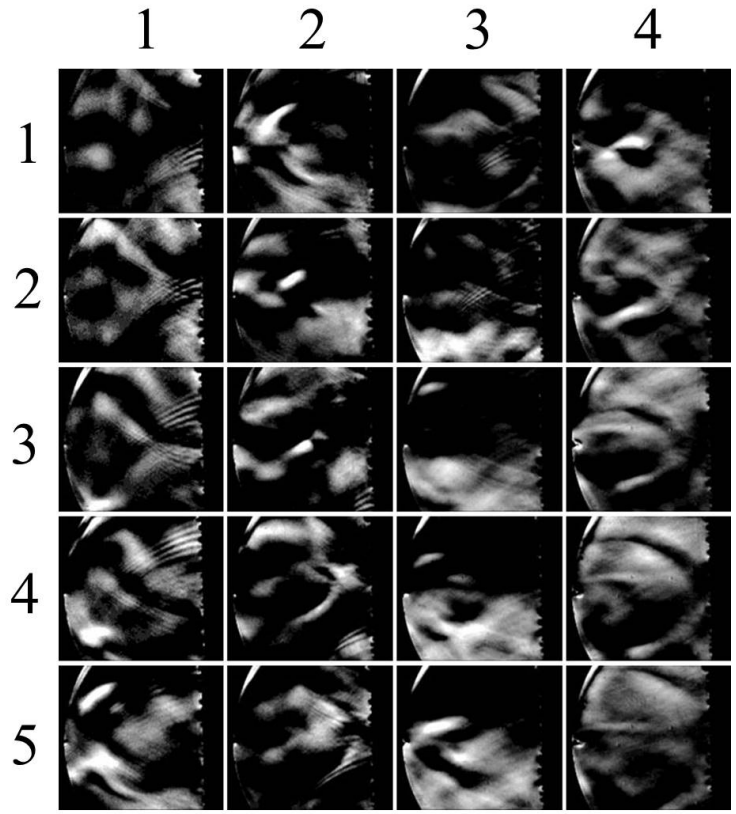


Figure 7.32: Time series of experimental images for the cylindrical test piece and an initial diaphragm pressure ratio of 3. From top left to bottom right. 0.00002s between images first image is approximately 0.00024s after diaphragm burst

Figure 7.33 compares the results from the numerical and experimental tests and highlights the major features which are seen in both cases. The black rectangles on the numerical results show the region of flow which is shown in the experimental images. The basic shape and timing of the features in the experiential results indicates that the numerical model is valid, however differences are also apparent in the actual shape of the compression waves, especially in the central image where the reflected waves are quite different between the experimental and numerical tests. The series of Mach lines which can be seen on several of the experimental images come from the diaphragm, both because it doesn't burst instantaneously and because it doesn't disappear completely and thus sends perturbations into the flow around it.

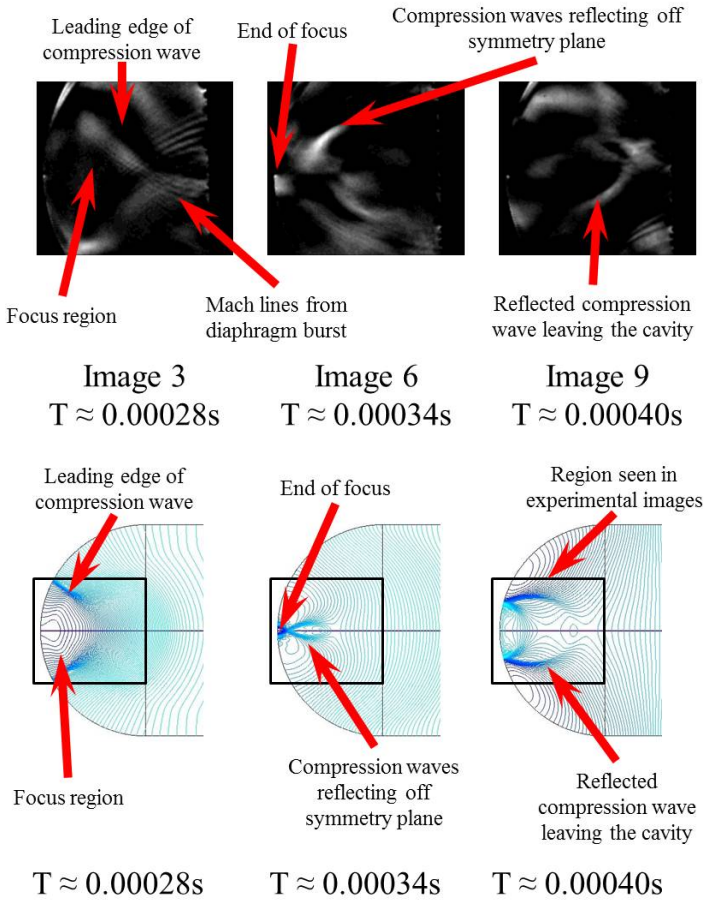


Figure 7.33: Flow features seen in experimental images and numerical contour plots for cylindrical test piece, P41 = 3

In the first column of Figure 7.35 the initial expansion wave can be seen moving into the driver in the first column. It is very faint, however the basic shape can be seen to be curved. The curvature is in the opposite direction to the curve of the diaphragm at burst and thus this curvature can mostly be contributed to the time it takes the diaphragm to burst rather than the shape at burst. The aluminium diaphragm bursts from the centre outward and thus the expansion wave starts moving from the centre first and only from the edge of the tube later once the diaphragm has opened, resulting in an expansion wave which is curved towards the driver. The triangular test piece gives stronger reflected expansion waves and these can be seen moving into driver section in the second column of Figure 7.34. The shocks which are clearly seen in the numerical work are not clear in the experimental images. This could be due to three dimensional effects from the diaphragm burst or the curvature of the initial expansion wave. Compression waves do seem to form in the third column of images, but these are difficult to make out and imply weak gradients which was not expected.

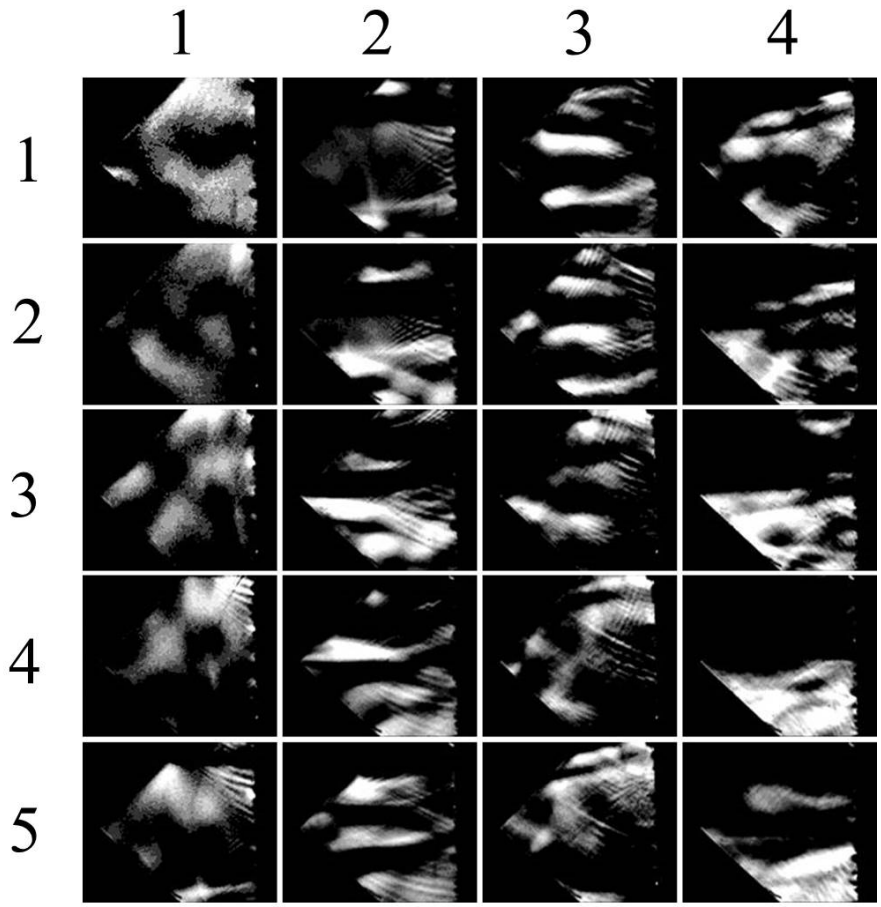


Figure 7.34: Time series of experimental images for the triangular test piece and an initial diaphragm pressure ratio of 3. From top left to bottom right. 0.00002s between images

Figure 7.35 gives a comparison of the results for the triangular test piece. The movement of the expansion waves is very similar between the numerical and experimental images, however the shock waves predicted by the numerical results are not present.

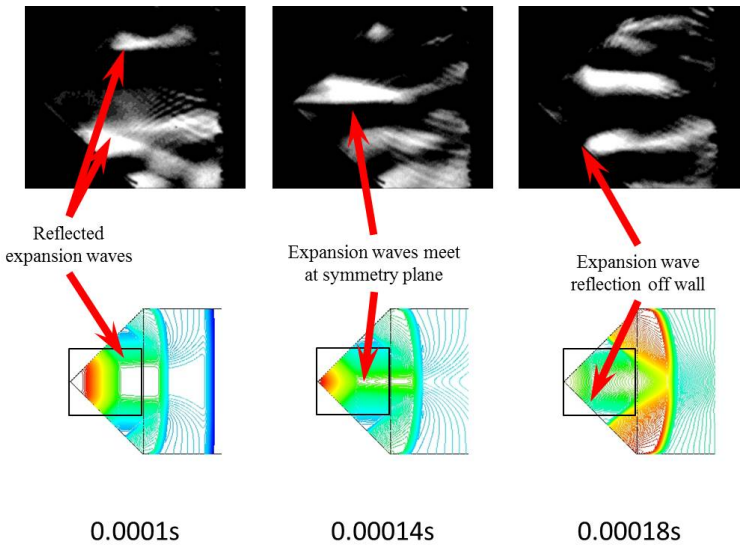


Figure 7.35: Flow features seen in experimental images and numerical contour plots for triangular test piece, P41 = 3

The reflected expansion waves from the converging test piece have the strongest gradients and they can be seen in the experimental images. Figure 7.36 gives experimental images for the converging test piece with a diaphragm pressure ratio of 3. The first column in Figure 7.36 shows the initial expansion wave and the reflected expansion waves moving into the driver. The compression waves enter the driver in the second and third column. In the final image in column 3 the wave moving into the driver is plane before it reflects off the walls as is predicted by the numerical results. Unfortunately the stronger gradients associated with this test piece means that large areas of the experimental image are very dark and as a result it is difficult to make out specific features and the later features predicted by the numerical simulations are not visible.

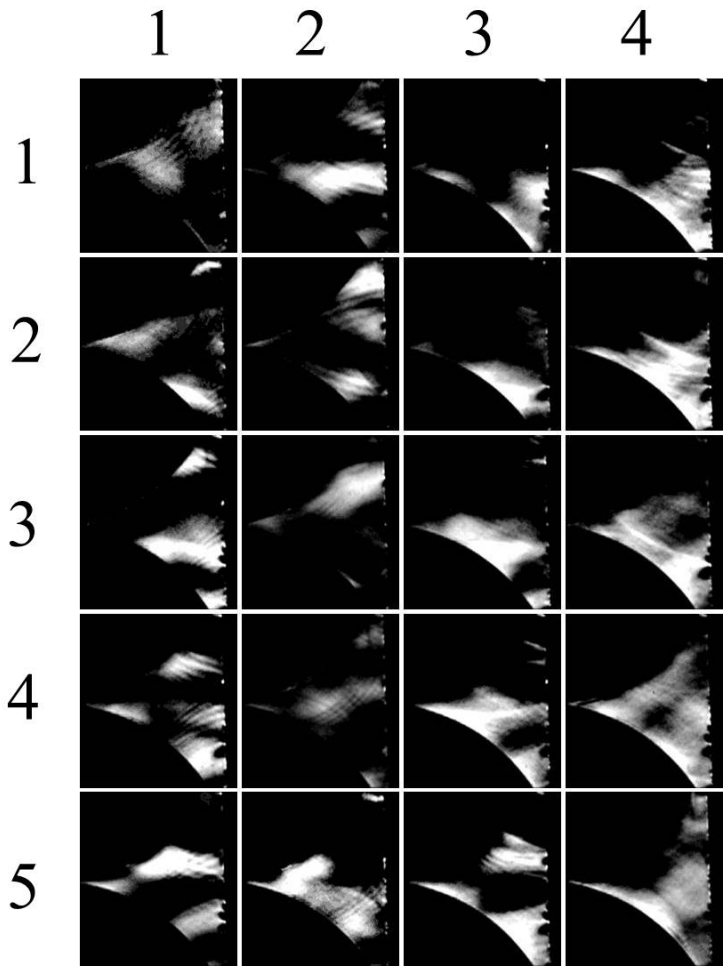


Figure 7.36: Time series of experimental images for the converging test piece and an initial diaphragm pressure ratio of 3. From top left to bottom right. 0.00002s between images

A comparison of the flow features seen in the experimental and numerical results is given in Figure 7.37. As with the results for a cylindrical test piece the black rectangles show the flow region which can be seen in the experimental images. Again the timing and basic shape of the flow features agree very well between the experimental and numerical results. The reflected expansion waves are slightly obscured in the experimental images by Mach lines coming off the diaphragm, however the position of the expansion waves matches very closely with what is predicted by the numerical results. Unlike the triangular test piece, the shape of the waves in this case are also very similar to those predicted. The compression waves which follow the expansion waves can be seen just coming into view at the edges of the central and right image in both the experimental and numerical results.

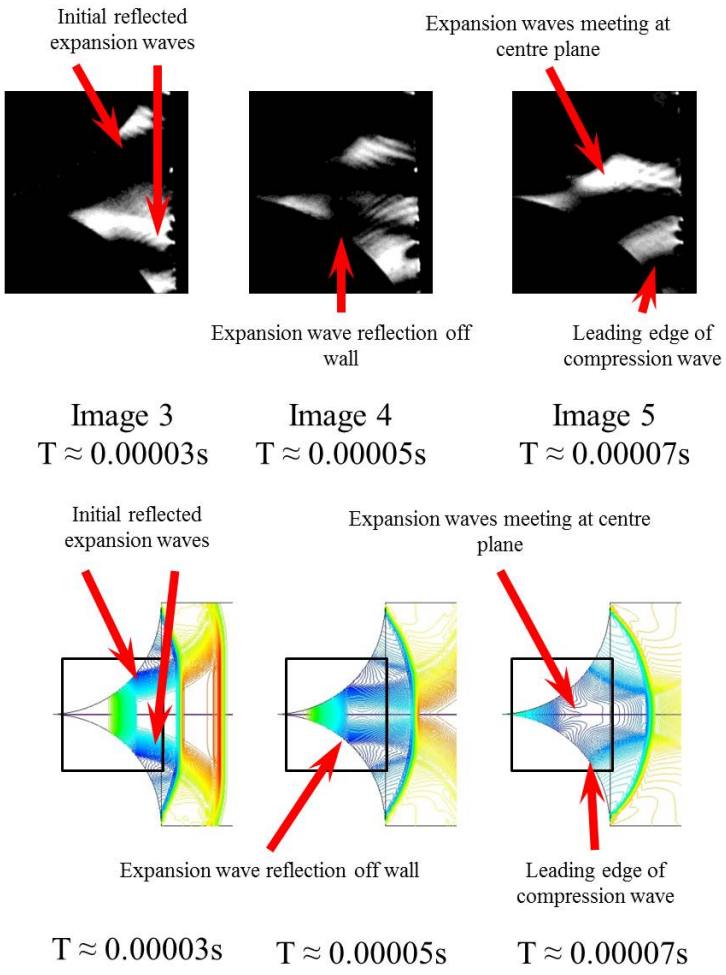


Figure 7.37: Flow features seen in experimental images for the converging test piece

Based on this qualitative study of the numerical and experimental results the numerical study can be considered valid as the major flow features it predicts are seen experimentally. The differences between the two results are likely due to the diaphragm burst not being modelled exactly by the numerical simulations and the initial expansion wave not being perfectly plane for the experimental work which has been shown to have a large affect on the the flow features, section 7.2.

7.5.1 Shock-wave formed at exit of shock tube

A feature which was seen for all the experimental testing, both with different diaphragm materials and different driver geometries was a shock wave which entered the driver at around 0.006s after diaphragm burst. Figure 7.38 shows this shock wave for three different types of diaphragm. This was initially thought to be the main shock from the diaphragm burst reflecting off the wall of the room in which the experiments were done and re-entering the

tube. In order to confirm this a numerical study which modelled an area outside the tube was done.

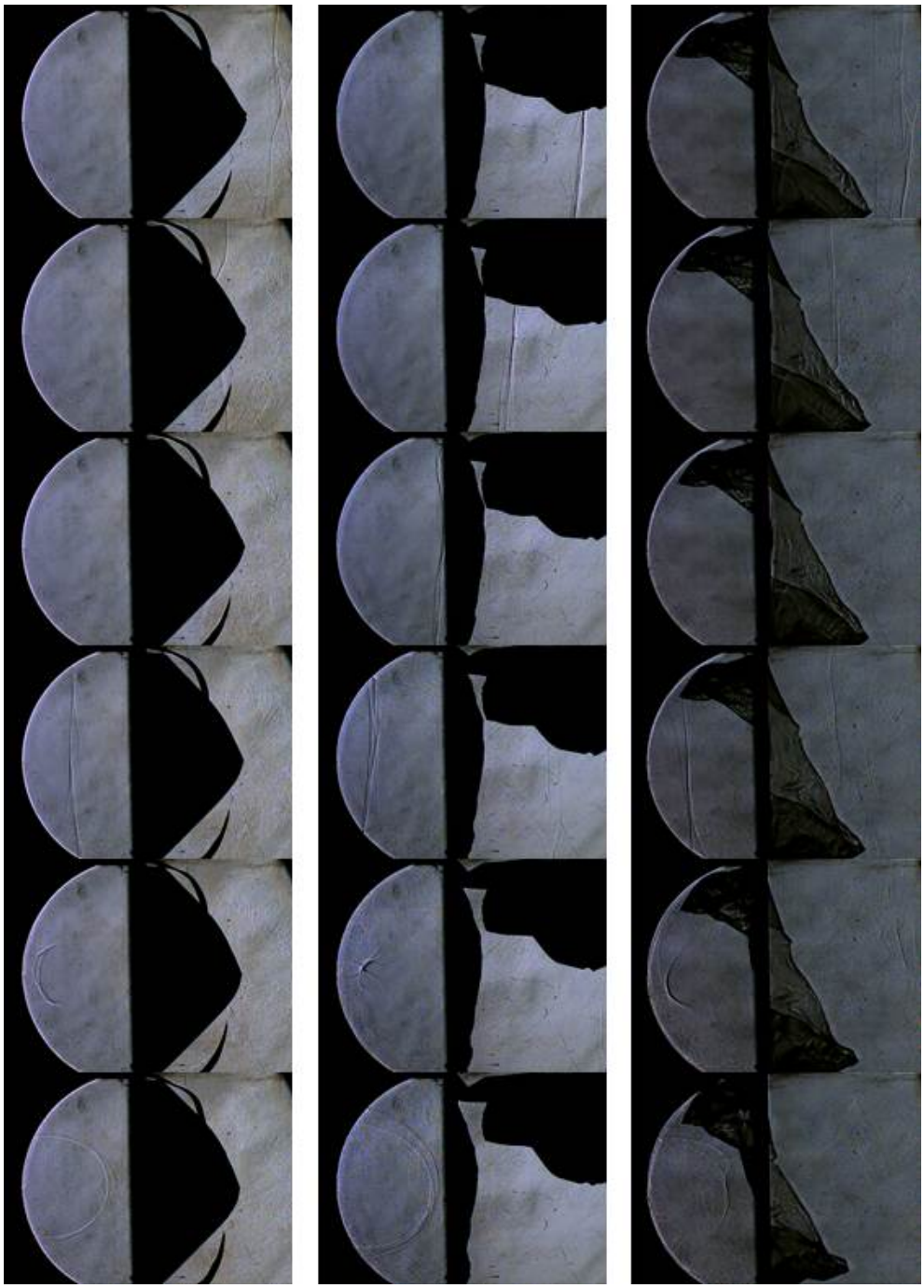


Figure 7.38: Shock wave at late time step in experimental results, left aluminium, middle brass, right plastic. First frame approximately 0.00565s, 0.0059s and 0.00595s after diaphragm burst respectively

Figure 7.39 shows how the shock wave is formed from the numerical simulation. The top image simply shows the shock wave expanding into the open area at the end of the tube.

The central images show a compression wave forming in the end of the tube as the expansion wave which reflected off the end of the driver reaches the end of the tube. The compression wave is strengthening and will form a shock wave as it moves back down the tube, resulting in the shock wave which is seen in the experimental results. The zoomed in image shows that the compression wave does form due to the expansion waves as it has already formed before the reflected shock wave from the area outside the tube enters the tube again.

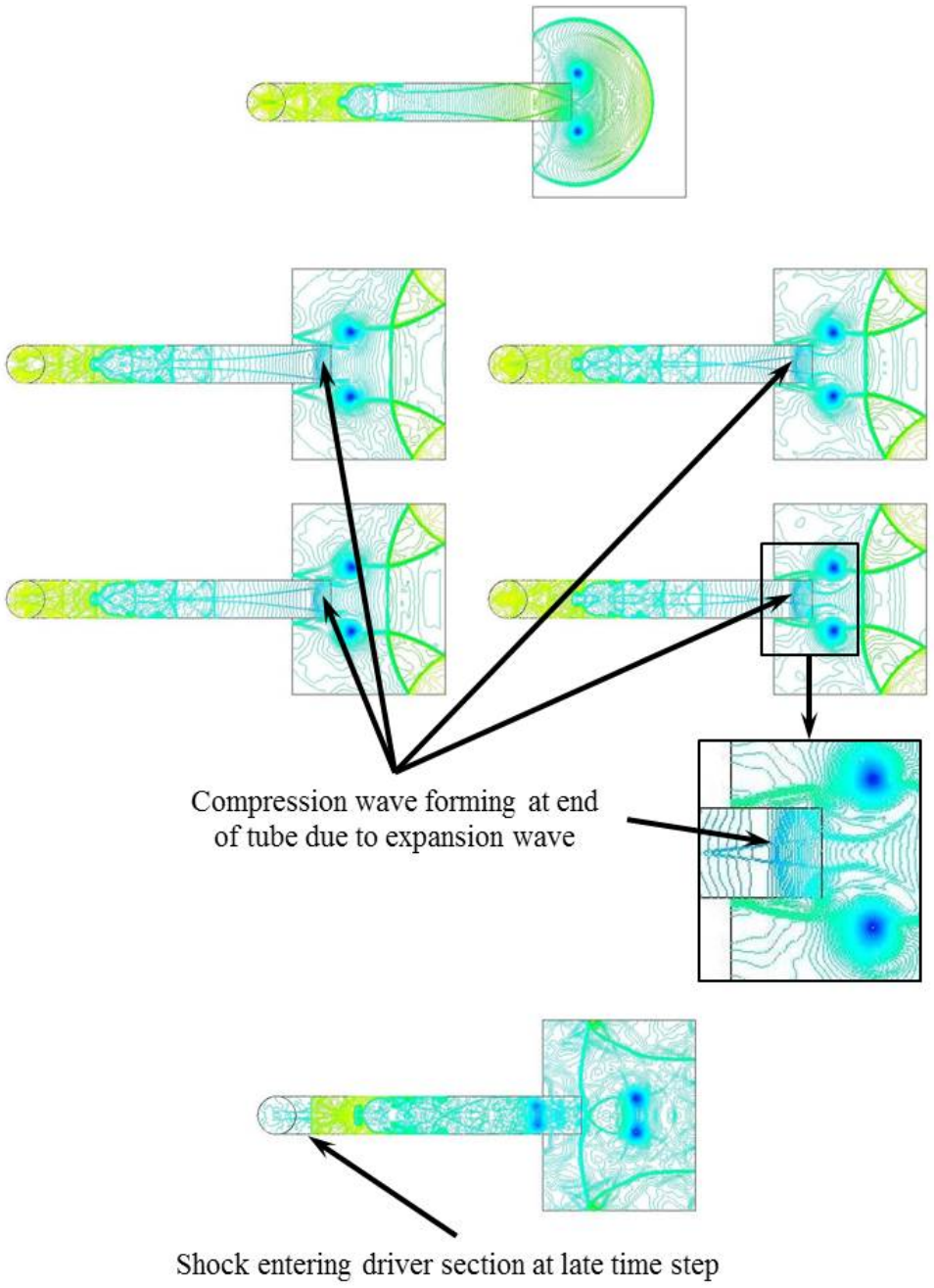


Figure 7.39: Numerical result showing formation of reflected shock at tube exit

7.5.2 Pressure trace comparisons

The pressure traces expected for the different geometries based on the numerical results are given in Figure 7.40 to Figure 7.42. The shock waves which form and move into the driver are clear on the traces. The shocks are significantly stronger for the triangular and converging test piece, with the peak pressure after the shocks being higher than the initial pressure in the driver for the converging test piece. This would be expected as the converging test piece comes to a point.

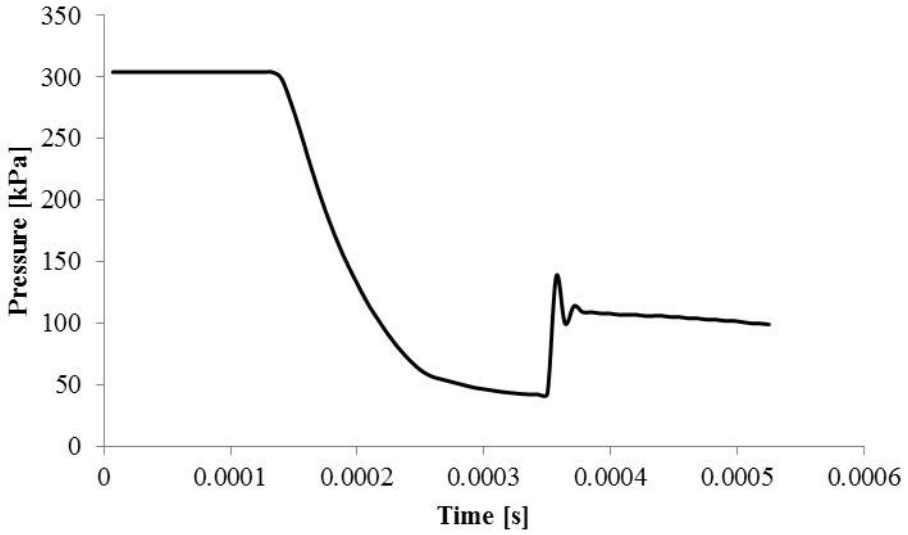


Figure 7.40: Pressure trace for numerical tests for the cylindrical test piece

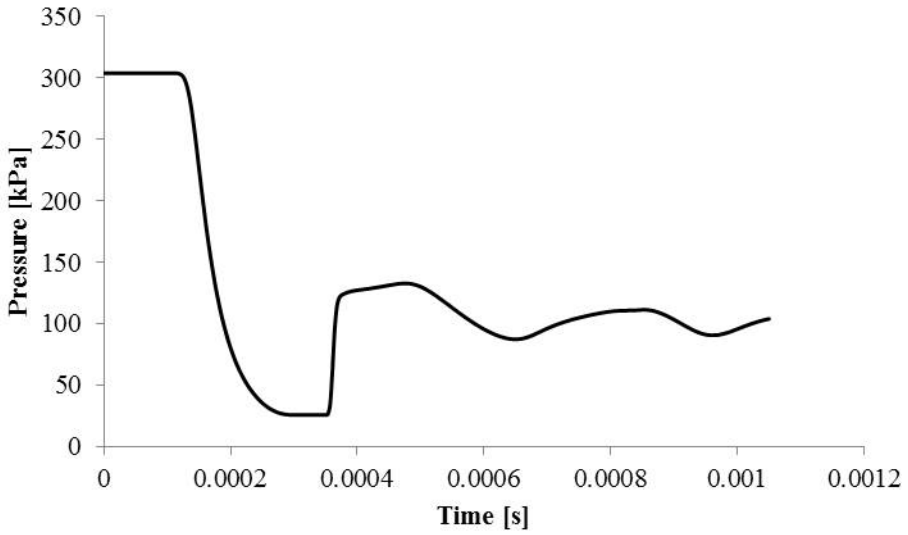


Figure 7.41: Pressure trace for numerical tests for the triangular test piece

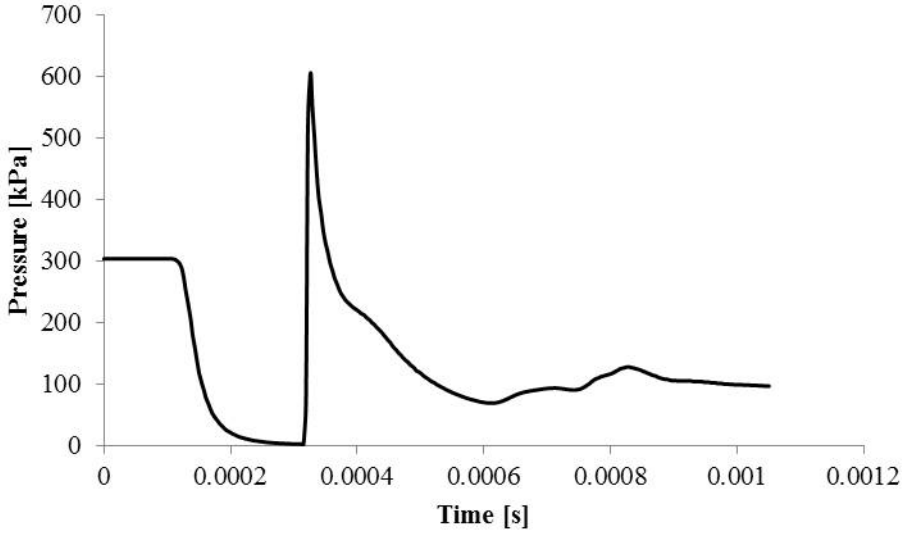


Figure 7.42: Pressure trace for numerical tests for the converging test piece

The pressure traces from the experimental results were not consistent, especially for the triangular and converging test piece. This is likely due to the transducer used not being accurate for vacuum pressures. The pressure traces obtained for the cylindrical test piece are presented in Figure 7.43 as they showed some consistency and the very rapid drop in pressure is clearly visible, however the accuracy of the measurement is still questionable and thus the pressure traces will not be used as validation for this research. Future work should be done to improve the accuracy of the pressure traces obtained experimentally.

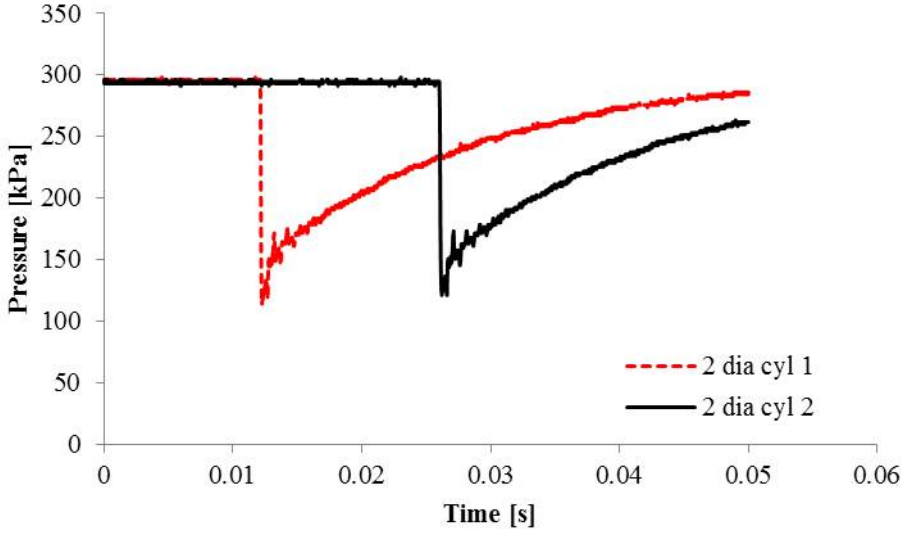


Figure 7.43: Comparison of pressure traces from the experimental tests for the cylindrical test piece

8 Conclusions

1. When an expansion wave enters a cavity it will create a reflection pattern which results in a region of low pressure, temperature and density being formed.
   (a) The shape of the focus region is affected by the initial shape of the expansion wave, with a curved expansion wave showing a weaker focus region than a plane wave entering a cavity.
   (b) The greater the pressure drop over the initial expansion wave the stronger the focusing which occurs.
   (c) The lower the gradient of the expansion wave, i.e. the further the expansion wave is from the initial diaphragm burst in a shock tube the weaker the focusing will be.
   (d) Numerical results predict that shock waves will form in the driver region of a shock tube if a cavity is present in the driver.
2. Experimental results show that the compression waves which form are unlikely to form into shock waves. This may be due to three dimensional effects in a shock tube or the nature of the diaphragm burst.

9 Recommendations

1. Additional experimental work with better optics should be done.
   (a) Replace the windows of the shock tube with glass rather than perspex in order to improve the quality of the images.
   (b) A higher resolution camera should be used to allow features to be seen more clearly.
   (c) A better quality colour schlieren system should be used in order to visualise the expansion waves.
2. Experiments with higher pressure ratios over the diaphragm should be done.
3. More investigation should be done into the diaphragm material used, a material which has a brittle failure mechanic may produce better results.
4. Experiments should be performed using a pressure transducer designed for vacuum pressures in order to obtain pressure traces to compare with the numerical work.

References

[1] Anderson, JD (2003) Modern Compressible Flow With Historical Perspective. New York: McGraw-Hill.

[2] Glass, I and Gordan Hall, J () "Shock Tubes." In "Handbook of Supersonic Aerodynamics," .

[3] Maclucas, DA (2012) Shock wave-induced flow features in concave profiles. Ph.D. thesis.

[4] Mahomed, I (2013) Two-dimensional expansion wave diffraction around a 90 convex corner. Ph.D. thesis, University of the Witwatersrand.

[5] Nishida, M (2001) Shock Tubes and Tunnels: Facilities, Instrumentation, and Techniques, vol. 1. doi: 10.1016/B978-012086430-0/50015-4.

[6] Skews, BW, Kleine, H, Barber, T, and Iannuccelli, M (2007) "New Flow Features in a Cavity During Shock Wave Impact." vol. 4, no. December, pp. 414–420.

[7] Wright, J (1961) Shock tubes. London: Methuen.

Appendix A Digital Appendix

1. Expansion Wave Generator Inventor parts and assemblies and spreadsheets with calculations
2. CFD Simulation data
   (a) Mesh Files
   (b) Mesh independence simulations
   (c) Journal files
   (d) Old CFD
   (e) Curved diaphragm
   (f) Plane diaphragm
   (g) STAR CCM+
3. Experimental pictures and pressure trace data
4. CFD images and plot data
5. Matlab programs
   (a) Image Processing
   (b) Data Processing
6. Animations

Appendix B Numerical Simulations

Table B.1: All numerical simulations run

Geometry	**Diaphragm Distance**	**Pressure Ratio**	**Diaphragm**	**Solver**
Cylindrical	0	3	Plane	Inviscid
Cylindrical	0	5	Plane	Inviscid
Cylindrical	0	7	Plane	Inviscid
Cylindrical	0	9	Plane	Inviscid
Cylindrical	0	12	Plane	Inviscid
Cylindrical	0	15	Plane	Inviscid
Cylindrical	0	7	Plane	k-ϵ
Cylindrical	0	5	Curved	Inviscid
Cylindrical	0	7	Curved	Inviscid
Cylindrical	0	7	Curved	k-ϵ
Cylindrical	60	7	Plane	Inviscid
Cylindrical	500	7	Plane	Inviscid
Triangular	0	3	Plane	Inviscid
Triangular	0	7	Plane	Inviscid
Triangular	0	12	Plane	Inviscid
Triangular	0	7	Curved	Inviscid
Triangular	0	7	Plane	k-ϵ
Triangular	0	7	Curved	k-ϵ
Converging	0	3	Plane	Inviscid
Converging	0	7	Plane	Inviscid
Converging	0	12	Plane	Inviscid
Converging	0	7	Curved	Inviscid
Converging	0	7	Plane	k-ϵ
Parabola AD 1	0	7	Plane	Inviscid
Parabola AD0.5	0	7	Plane	Inviscid
Control	N/A	7	Plane	Inviscid

Appendix C Experimental Tests